

| REPORT DOCUMENTATION PAGE  |             |  | Form Approved<br>OMB No. 0704-0188 |  |
|--|-------------|--|------------------------------------|--|
| Public reporting burden for this collection of information is estimated to average 1 hour per response, including the time for reviewing instructions, searching existing data sources, gathering and maintaining the data needed, and completing and reviewing this collection of information. Send comments regarding this burden estimate or any other aspect of this collection of information, including suggestions for reducing this burden to Department of Defense, Washington Headquarters Services, Directorate for Information Operations and Reports (0704-0188), 1215 Jefferson Davis Highway, Suite 1204, Arlington, VA 22202-4302. Respondents should be aware that notwithstanding any other provision of law, no person shall be subject to any penalty for failing to comply with a collection of information if it does not display a currently valid OMB control number. PLEASE DO NOT RETURN YOUR FORM TO THE ABOVE ADDRESS.   |             |  |                                    |  |
| 1. REPORT DATE (DD-MM-YYYY)<br>19-03-2007  |             | 2. REPORT TYPE<br>Final                              |                                    | 3. DATES COVERED (From - To)<br>06-01-2003 to 11-30-2006 |
| ELECTROMAGNETIC CONTROL OF HIGH HEAT-FLUX SPRAY<br><br>IMPINGEMENT BOILING UNDER MICROGRAVITY CONDITIONS   |             | 5a. CONTRACT NUMBER                                  |                                    |  |
|  |             | 5b. GRANT NUMBER<br>F49620-03-1-0276                 |                                    |  |
|  |             | 5c. PROGRAM ELEMENT NUMBER                           |                                    |  |
| 6. AUTHOR(S) Donald D. Gray, John M. Kuhlman,<br><br>Shannon L. Glaspell, C. Andy Hunnell, Paul J.<br><br>Kreitzer, Deepak Mehra, and Rageey M. Youssef  |             | 5d. PROJECT NUMBER                                   |                                    |  |
|  |             | 5e. TASK NUMBER                                      |                                    |  |
|  |             | 5f. WORK UNIT NUMBER                                 |                                    |  |
| 7. PERFORMING ORGANIZATION NAME(S) AND ADDRESS(ES)<br><br>WVU Research Corporation<br>886 Chestnut Ridge Road<br>P.O. Box 6216<br>Morgantown, WV 26506-6216  |             | 8. PERFORMING ORGANIZATION<br>REPORT                 |                                    |  |
| 9. SPONSORING / MONITORING AGENCY NAME(S) AND ADDRESS(ES)<br><br>AFOSR<br>875 N Randolph St<br>Arlington VA 22203<br>Rhett Jeffries/NA   |             | 10. SPONSOR/MONITOR'S<br><br>- AFRL-SR-AR-TR-07-0205 |                                    |  |
| 12. DISTRIBUTION / AVAILABILITY STATEMENT<br>Approved for public release,<br>distribution unlimited  |             |  |                                    |  |
| 13. SUPPLEMENTARY NOTES AFRL/AFOSR/NA Project Manager is LtCol Rhett Jefferies, USAF.  |             |  |                                    |  |
| 14. ABSTRACT The primary goal of this project was to discover how to most effectively use electromagnetic forces to enhance spray impingement boiling heat transfer in microgravity ( $\mu g$ ). This project was closely coordinated with the non-electromagnetic spray impingement boiling experiments conducted by Dr. Kirk L. Yerkes of the Air Force Research Laboratory (AFRL). The West Virginia University (WVU) investigation of electrical body forces to enhance and control spray impingement boiling extended the AFRL research. The computational phase of the WVU project was based on the commercial multiphysics code CFD-ACE+, which was successfully modified to incorporate the Coulomb and electric Kelvin forces. WVU's ground-based experiments demonstrated for the first time that modest increases in heat transfer coefficient and Nusselt number can be achieved in spray impingement boiling by using electrical forces, thus confirming the fundamental hypothesis of this research. Further increases in heat transfer performance are likely to result from a better understanding of the relevant microphysics and better electrode designs. Experimental results have been used to estimate the time scales for various phenomena that occur in spray impingement boiling, which could lead to improved electrode designs. |             |  |                                    |  |
| 15. SUBJECT TERMS<br>spray cooling, boiling heat transfer, electrical forces, microgravity   |             |  |                                    |  |
| 16. SECURITY CLASSIFICATION OF:  |             |  | 17. LIMITATION<br>OF ABSTRACT      | 18.<br>NUMBER<br>OF PAGES                                |
| a. REPORT  | b. ABSTRACT | c. THIS PAGE   |                                    |  |
|  |             |  |                                    | 19a. NAME OF RESPONSIBLE<br>PERSON                       |
|  |             |  |                                    | 19b. TELEPHONE NUMBER (include<br>area code)             |

Final Report

**ELECTROMAGNETIC CONTROL OF HIGH HEAT-FLUX SPRAY IMPINGEMENT  
BOILING UNDER MICROGRAVITY CONDITIONS**

Donald D. Gray<sup>1</sup>, John M. Kuhlman<sup>2</sup>,  
Shannon L. Glaspell<sup>2</sup>, C. Andy Hunnell<sup>2</sup>, Paul J. Kreitzer<sup>2</sup>,  
Deepak Mehra<sup>1</sup>, and Rageey M. Youssef<sup>1</sup>

<sup>1</sup>Department of Civil and Environmental Engineering

<sup>2</sup>Department of Mechanical and Aerospace Engineering,  
West Virginia University  
Morgantown, WV 26506

March 2007

## ACKNOWLEDGMENTS

This work was sponsored by the Air Force Office of Scientific Research, USAF, under grant number F49620-03-1-0276. The views and conclusions contained herein are those of the authors and should not be interpreted as necessarily representing the official policies or endorsements, either expressed or implied, of the Air Force Office of Scientific Research or the U.S. Government.

Support from CFD Research Corporation for the high speed video camera, and from the University of Dayton Research Institute is gratefully acknowledged. Technical discussions with our lead AFRL technical contact, Dr. Kirk L. Yerkes, and his colleagues Mr. Richard Harris and Mr. Travis Michalak are greatly appreciated.

## ABSTRACT

The primary goal of this project was to discover how to most effectively use electromagnetic forces to enhance spray impingement boiling in microgravity ( $\mu g$ ). This project was closely coordinated with the non-electromagnetic spray impingement boiling heat transfer experiments conducted by Dr. Kirk L. Yerkes of the Air Force Research Laboratory (AFRL). The West Virginia University (WVU) investigation of electrical body forces to enhance and control spray impingement boiling extended the AFRL research. The computational phase of the WVU project was based on the commercial multiphysics code CFD-ACE+, which was successfully modified to incorporate the Coulomb and electric Kelvin forces. WVU's ground-based experiments demonstrated for the first time that modest increases in heat transfer coefficient and Nusselt number can be achieved in spray impingement boiling by using electrical forces, thus confirming the fundamental hypothesis of this research. Further increases in heat transfer performance are likely to result from a better understanding of the relevant microphysics and better electrode designs. Experimental results have been used to estimate the time scales for various phenomena that occur in spray impingement boiling, which could lead to improved electrode designs.

## EXECUTIVE SUMMARY

In order to reach the higher levels of performance required in future aircraft and spacecraft, improved methods of thermal management must be developed. Spray impingement boiling under conditions of variable gravity has been under investigation at the Air Force Research Laboratory, Propulsion Directorate, Power Division (AFRL/PRPS) under the direction of Dr. Kirk L. Yerkes. The West Virginia University (WVU) project extended the AFRL work by studying the effect of electrical forces on spray cooling. The primary goal of the WVU project was to discover if electrical or magnetic forces could enhance spray impingement boiling; and, if this was possible, how it could be done most effectively. Both computational and experimental approaches were used.

The computational phase of the WVU project was based on the commercial multiphysics code CFD-ACE+ which was successfully modified to incorporate the Coulomb and electric Kelvin forces. Several flows that embody phenomena that occur in spray impingement boiling were simulated. All of the simulations were performed using single processor personal computers, and all assumed two dimensional axisymmetric flow.

Simulations of the experiments of Labus (1977), in which an isothermal jet impinged on a sharp edge disk in microgravity ( $\mu g$ ), reproduced the qualitative behavior of the surface tension and inertial flow regimes seen in moving and still photos of the experiments. The experiment of Liu and Lienhard (1989), in which a round jet impinged on a constant heat flux surface without phase change, was also simulated. The computed values of local Nusselt number as a function of distance from the impingement point showed good agreement with the experimental data.

Simulations of a droplet impacting a dry wall reproduced the spread and rebound of the droplet, although the simulations were stopped before the rebounding droplet would have left the surface. The ratio of the maximum radius of spread to the drop diameter showed a sensitive dependence on contact angle which agreed with the experimental data.

Simulations of a droplet hitting a liquid layer using a relatively coarse grid revealed the formation of the crown and the Worthington jet, including the pinch-off of a droplet. The ejection of the droplet was in agreement with the experimental splashing criterion of Cossali et al. (1977). With a much finer grid, additional details of the flow became visible, notably the ring jet observed experimentally by Thoroddsen (2002).

CFD-ACE+ was modified to allow the inclusion of the Coulomb and electric Kelvin forces. The interaction of spray drops and liquid layers is not fully understood, so it could not be properly modeled by the code. In particular, the fate of free charge carried by droplets when they impinge on a wall or a liquid film requires further study. Two new boundary conditions were added to the code to account for the limiting cases of an insulated wall and a grounded perfectly conducting wall.

The flow of a round free jet in the WVU experimental geometry was simulated with no body force, with terrestrial gravity in the initial direction of the jet, and with terrestrial gravity opposed by the electric Kelvin force due to the second generation electrode system. The Kelvin force

distorted the jet and appeared to create free surface waves near the impact zone, confirming that significant electric Kelvin forces can be created in the vicinity of a heated surface.

The goal of simulating a spray with boiling on the impingement surface was not reached, primarily because the computational requirements exceeded the capabilities of the Pentium 4 class single processor personal computers that were used. In addition, significant gaps in physical understanding concerning the interaction of both uncharged and charged sprays with liquid films and solid surfaces were encountered. The microphysics of bubble growth in flow boiling is another key area requiring more research. Progress in simulating spray impingement boiling will require better understanding of these phenomena.

An apparatus was constructed with assistance from AFRL researchers that was closely patterned after their spray impingement boiling experiment. In the WVU apparatus, a single full-cone spray nozzle sprays a dielectric coolant onto a circular resistive heater. This WVU apparatus is identical to the AFRL apparatus with the exception of high-voltage feedthroughs and electrodes.

Without electrical body force effects, heat transfer performance in Earth gravity for both vertical downward and horizontal spray impingement has been documented for spray flow rates between  $4.8 \times 10^{-6} \text{ m}^3/\text{s}$  and  $9.8 \times 10^{-6} \text{ m}^3/\text{s}$  (4.6 GPH to 9.3 GPH), and heater power levels from 10 W to 70 W. The heat transfer coefficient increases with increased spray flow rate, but is only weakly dependent on the heater power level. Different brass and PVC spray nozzles show significant variations in spray cooling performance (order of  $\pm 5\text{-}15\%$ ) whenever the nozzle is realigned or the nozzle-to-heater spacing is changed. Flow visualization using a high speed digital video camera and laser light sheet illumination indicates a highly contorted free surface for the liquid film that forms on the heater surface. Outward radial motion of the wave-like craters and ridges that form on the interface is observed.

Results have also been obtained for the effects of electrical body forces on heat transfer performance of the identical instrumented spray nozzle and heater for ranges of electrode voltage, and for similar ranges of spray volume flow rate and heater power level using a TFR heater. An initial series of Kelvin force electrode designs showed no improvement in heat transfer using FC-72, while a second-generation Kelvin force electrode that was designed using the CFD-ACE+ code showed modest but consistent improvements (order of 10% in heat flux; order of 5% for Nusselt number) using HFE-7000. These heat transfer enhancements are seen only during two phase cooling. Two Coulomb force electrode geometries also showed modest but consistent improvements in heat transfer (order of 5-15%), but only at heat fluxes where boiling of the liquid film occurs.

The flow visualization results have been used to aid in the estimation of characteristic time scales governing the effects of surface tension, gravity, heating of the liquid film, and vaporization of the film. For the present dense liquid sprays, it is concluded that none of these time scales are as short as the average time between droplet impacts into a heater surface area equal to the estimated size of the thin, crater-like liquid films formed by a previous droplet impact.

The most significant result of this research is that the fundamental hypothesis that spray impingement boiling heat transfer can be enhanced by electrical fields has been demonstrated for

the first time. Neither the Coulomb nor the Kelvin force electrodes used in these tests have been optimized so a significantly greater enhancement of heat transfer by means of electrical forces can still be achieved.

The following persons participated in this research project:

|                     |  |
|---------------------|--|
| Donald D. Gray      | Principal Investigator, Professor, West Virginia University    |
| John M. Kuhlman     | Co-Principal Investigator, Professor, West Virginia University |
| Shannon L. Glaspell | Graduate Research Assistant, West Virginia University          |
| C. Andy Hunnell     | Graduate Research Assistant, West Virginia University          |
| Paul J. Kreitzer    | Graduate Research Assistant, West Virginia University          |
| Deepak Mehra        | Graduate Research Assistant, West Virginia University          |
| Rageey M. Youssef   | Graduate Research Assistant, West Virginia University          |
| Vincent DeCapio     | Undergraduate Research Assistant, West Virginia University     |
| Stephen Epifano     | Undergraduate Research Assistant, West Virginia University     |
| Benjamin Truschel   | Undergraduate Research Assistant, West Virginia University     |

The following publications have resulted from this project:

Cole, V., Mehra, D., Lowry, S., Gray, D., 2005. "A Numerical Spray Impingement Model Coupled with a Free Surface Film Model," *Proceedings of the 16<sup>th</sup> Annual Thermal and Fluids Analysis Workshop (TFAWS-2005)*, 14 pages.

[http://www.ustdc.com/tfaws/files/InterdisciplinaryPaperSession/TFAWS05\\_VCole\\_ID.pdf](http://www.ustdc.com/tfaws/files/InterdisciplinaryPaperSession/TFAWS05_VCole_ID.pdf)

Glaspell, S. L., 2006. "Effects of the Electric Kelvin Force on Spray Cooling Performance," M. S. Thesis, West Virginia University, Dept. of Mechanical and Aerospace Engineering, Morgantown, WV.

Hunnell, C. A., 2005. "Design, Construction, and Initial Testing of Experimental Test Package for Convective Spray Cooling in Terrestrial Gravity Conditions," M. S. Thesis, West Virginia University, Dept. of Mechanical and Aerospace Engineering, Morgantown, WV.

Hunnell, C. A., Kuhlman, J. M., and Gray, D. D., 2005. "Spray Cooling Heat Transfer under Terrestrial-Gravity Conditions", draft report submitted to Air Force Research Laboratory, July.

Hunnell, C. A., Kuhlman, J. M., and Gray, D. D., 2006. "Spray Cooling in Terrestrial and Simulated Reduced Gravity," *Space Technology & Applications International Forum (STAIF-2006)*, AIP Conference Proceedings Volume 813, M. S. El-Genk, editor, 126-133.

Kreitzer, P. J., 2006. "Experimental Testing of Convective Spray Cooling with the Aid of an Electric Field Using the Coulomb Force," M. S. Thesis, West Virginia University, Dept. of Mechanical and Aerospace Engineering, Morgantown, WV.

Kreitzer, P. J., Glaspell, S. L., Kuhlman, J. M., Mehra, D., and Gray, D. D., 2006. "Electrical Force Effects on Spray Cooling," Paper 06PSC-61, SAE 2006 Power Systems Conference, New Orleans, LA, Sept. 7-9.

Kuhlman, J. M., Kreitzer, P. J., Mehra, D., Gray, D. D., and Yerkes, K. L., 2007. "Influence of the Coulomb Force on Spray Cooling," STAIF 11<sup>th</sup> Conference on Thermophysics Applications in Microgravity, Albuquerque, NM, Feb. 11-15.

Mehra, D., 2007. "Effects of Varying Body Forces on Isothermal and Non Isothermal Liquid Jet Impingement", Ph. D. Dissertation, West Virginia University, Dept. of Civil and Environmental Engineering, Morgantown, WV.

Youssef, R. M., 2007. "Modeling the Effect of a Spray on a Liquid Film on a Heated Surface," Ph. D. Dissertation, West Virginia University, Dept. of Civil and Environmental Engineering, Morgantown, WV.

## TABLE OF CONTENTS

|  | Page |
|--|------|
| CHAPTER 1 INTRODUCTION .....   | 1    |
| CHAPTER 2. PHYSICAL BASIS .....  | 5    |
| 2.1 Electromagnetic Body Forces in Fluids.....   | 5    |
| 2.2 Coolant Properties.....  | 7    |
| CHAPTER 3. COMPUTATIONAL INVESTIGATIONS.....   | 11   |
| 3.1 The Multiphysics Code CFD-ACE+.....  | 11   |
| 3.2 Simulations Without Electric Forces .....  | 15   |
| 3.2.1 Round Jet Hitting a Sharp Edge Disk in Microgravity .....                          | 16   |
| 3.2.1.1 Surface Tension Flow Regime.....   | 17   |
| 3.2.1.2 Inertial Flow Regime .....   | 19   |
| 3.2.2 Round Jet Hitting a Heated Surface.....  | 22   |
| 3.2.3 Drop Hitting a Wall .....  | 24   |
| 3.2.3.1 Drop Hitting a Dry Wall .....  | 25   |
| 3.2.3.2 Drop Hitting a Wet Wall.....   | 28   |
| 3.3 Simulations with Electric Forces .....   | 32   |
| 3.3.1 Coulomb Force.....   | 32   |
| 3.3.2 Electric Kelvin Force .....  | 33   |
| 3.3.2.1 Effect of Kelvin Force on Liquid Jet Hitting a Surface .....                     | 38   |
| 3.3.2.1.1 Case 1: Low Velocity with No Gravitational Force and No Kelvin Force....       | 39   |
| 3.3.2.1.2 Case 2: Low Velocity with Gravitational Force and No Kelvin Force.....         | 42   |
| 3.3.2.1.3 Case 3: Higher Velocity with No Gravitational Force and No Kelvin Force        | 45   |
| 3.3.2.1.4 Case 4: Higher Velocity with Gravitational Force and No Kelvin Force.....      | 49   |
| 3.3.2.1.5 Case 5: Low Velocity with Gravitational Force Opposed by Kelvin Force .        | 52   |
| 3.3.2.1.6 Case 6: Higher Velocity with Gravitational Force Opposed by Kelvin Force ..... | 56   |
| CHAPTER 4 EXPERIMENTAL INVESTIGATIONS.....   | 61   |
| 4.1 Introduction.....  | 61   |
| 4.2 Experimental Apparatus.....  | 61   |
| 4.2.1 Statement of Experimental Accuracy .....   | 66   |

|   |    |
|---|----|
| 4.3 Experiments Without Electrical Forces ..... | 67 |
| 4.4 Experiments with Electrical Forces .....    | 78 |
| 4.4.1 Electric Kelvin Force Experiments.....    | 78 |
| 4.4.2 Coulomb Force Experiments .....           | 84 |
| CHAPTER 5 TIME SCALE ESTIMATES.....             | 89 |
| CHAPTER 6 CONCLUSIONS AND RECOMMENDATIONS ..... | 93 |
| REFERENCES .....                                | 96 |

## LIST OF FIGURES

|  | Page |
|--|------|
| Figure 1.1 Schematic of spray cooling droplet impingement .....  | 2    |
| Figure 3.1 Labus Case 1 simulation at $t = 1.2$ s mirrored on axis of symmetry. ....                                     | 18   |
| Figure 3.2 Surface tension case photographed by Labus (1977). ....   | 18   |
| Figure 3.3 Streamlines for Case 1 at 1.2 s. ....   | 19   |
| Figure 3.4 Labus Case 2 simulation mirrored on y axis at $t = 0.3$ s. ....   | 20   |
| Figure 3.5 Inertial flow photographed by Labus (1977). ....  | 20   |
| Figure 3.6 Streamlines for Labus Case 2 simulation at $t = 0.3$ s. ....  | 21   |
| Figure 3.7 Location of free surface for inertial flow in experiment (Labus, 1977, Figure 25) and Case 3 simulation. .... | 22   |
| Figure 3.8 Streamlines for liquid jet impingement on a uniformly heated surface at steady state conditions. ....         | 23   |
| Figure 3.9 Water droplet at time = 0 s. ....   | 25   |
| Figure 3.10 Water droplet with $100^\circ$ contact angle at time = 2.5 ms. ....  | 26   |
| Figure 3.11 Water droplet with $100^\circ$ contact angle at time = 3.5 ms. ....  | 26   |
| Figure 3.12 Water droplet with $100^\circ$ contact angle after time = 6.5 ms. ....                                       | 26   |
| Figure 3.13 Water droplet with $100^\circ$ contact angle at time = 8 ms. ....  | 27   |
| Figure 3.14 Droplet spreading factor as a function of time for various static contact angles. ....                       | 27   |
| Figure 3.15 Droplet and liquid layer at zero time. ....  | 29   |
| Figure 3.16 Drop splash at 0.15 ms. ....   | 29   |
| Figure 3.17 Drop splash at 1.5 ms. ....  | 30   |
| Figure 3.18 Drop splash at 2.8 ms. ....  | 30   |
| Figure 3.19 Drop splash at 0.01 ms. ....   | 31   |
| Figure 3.20 Drop splash at 0.014 ms. ....  | 32   |
| Figure 3.21 Schematic of apparatus (axisymmetric geometry). ....   | 34   |
| Figure 3.22 Location of the electrodes. ....   | 35   |
| Figure 3.23 Electric field lines. ....   | 36   |
| Figure 3.24 Lines tangent to $\nabla E^2$ . ....   | 37   |
| Figure 3.25 X direction (axial) Kelvin force to mass ratio. ....   | 37   |
| Figure 3.26 X direction (axial) Kelvin force to mass ratio vs. radius. ....  | 38   |
| Figure 3.27 Y direction (radial) Kelvin force to mass ratio vs. radius. ....   | 38   |
| Figure 3.28 Case 1 at $t = 0.017\ 264$ s. ....   | 40   |
| Figure 3.29 Case 1 at $t = 0.056\ 22$ s. ....  | 40   |
| Figure 3.30 Case 1 at $t = 0.136\ 08$ s. ....  | 40   |
| Figure 3.31 Case 1 at $t = 0.144\ 2$ s. ....   | 41   |
| Figure 3.32 Case 1 at $t = 0.161\ 987$ s. ....   | 42   |
| Figure 3.33 Case 2 at $t = 0.024\ 245$ s. ....   | 43   |
| Figure 3.34 Case 2 at $t = 0.047\ 497$ s. ....   | 43   |
| Figure 3.35 Case 2 at $t = 0.063\ 007$ s. ....   | 44   |
| Figure 3.36 Case 2 at $t = 0.071\ 762$ s. ....   | 44   |
| Figure 3.37 Case 2 at $t = 0.079\ 455$ s. ....   | 45   |
| Figure 3.38 Case 3 at $t = 0.018\ 261$ s. ....   | 46   |
| Figure 3.39 Case 3 at $t = 0.035\ 454$ s. ....   | 46   |
| Figure 3.40 Case 3 at $t = 0.053\ 719$ s. ....   | 47   |

|   |    |
|---|----|
| Figure 3.41 Case 3 at $t = 0.059\,941$ s. ....  | 48 |
| Figure 3.42 Case 3 at $t = 0.081\,823$ s. ....  | 49 |
| Figure 3.43 Case 4 at $t = 0.012\,631$ s. ....  | 50 |
| Figure 3.44 Case 4 at $t = 0.025\,450$ s. ....  | 50 |
| Figure 3.45 Case 4 at $t = 0.042\,413$ s. ....  | 51 |
| Figure 3.46 Case 4 at $t = 0.047\,900$ s. ....  | 52 |
| Figure 3.47 Case 5 at $t = 0.034\,488$ s. ....  | 53 |
| Figure 3.48 Case 5 at $t = 0.042\,183$ s. ....  | 53 |
| Figure 3.49 Case 5 at $t = 0.049\,668$ s. ....  | 53 |
| Figure 3.50 Case 5 at $t = 0.058\,571$ s. ....  | 54 |
| Figure 3.51 Case 5 at $t = 0.063\,996$ s. ....  | 55 |
| Figure 3.52 Case 5 at $t = 0.069\,101$ s. ....  | 56 |
| Figure 3.53 Case 6 at $t = 0.0132\,82$ s. ....  | 57 |
| Figure 3.54 Case 6 at $t = 0.025\,813$ s. ....  | 57 |
| Figure 3.55 Case 6 at $t = 0.0351\,30$ s. ....  | 58 |
| Figure 3.56 Case 6 at $t = 0.041\,013$ s. ....  | 58 |
| Figure 4.1 Schematic of the nozzle, pedestal, heater spray, sump and cap. ....  | 62 |
| Figure 4.2 Overview of experimental apparatus for initial baseline data (Hunnell, 2005). ....   | 63 |
| Figure 4.3 Schematic of experimental flow loop, showing test fluid flow loop and cooling water<br>flow loop. ....   | 64 |
| Figure 4.4 Sump and pedestal, without a cap, inserted into the spray chamber. ....  | 64 |
| Figure 4.5 Thermocouple locations in the spray chamber. ....  | 65 |
| Figure 4.6 Comparison of vertical and horizontal spray heat flux as a function of surface<br>temperature for the unconfined geometry at two different flow rates. ....  | 68 |
| Figure 4.7 Comparison of vertical and horizontal spray heat flux as a function of surface<br>temperature for the straight cap geometry at two different flow rates. ....  | 68 |
| Figure 4.8 Comparison of vertical spray heat flux as a function of surface temperature for both<br>the ITO and TFR pedestals at a flow rate of 9.3 GPH. ....  | 69 |
| Figure 4.9 Heat transfer coefficient as a function of power for both the vertical downward spray<br>and horizontal spray with a straight cap. ....  | 70 |
| Figure 4.10 Comparison of vertical and horizontal spray non-dimensional heat flux as a function<br>of non-dimensional surface temperature difference for the unconfined geometry at two<br>different flow rates. ....   | 71 |
| Figure 4.11 Comparison of vertical and horizontal spray non-dimensional heat flux as a function<br>of non-dimensional surface temperature difference for the straight cap geometry at two<br>different flow rates. .... | 71 |
| Figure 4.12 Comparison of vertical spray non-dimensional heat flux as a function of non-<br>dimensional surface temperature difference for ITO and TFR heaters at a flow rate of 9.3<br>GPH. ....                       | 72 |
| Figure 4.13 Nusselt number as a function of non-dimensional heat flux for both the vertical<br>downward spray and horizontal spray with straight cap. ....  | 72 |
| Figure 4.14 Interaction between the spray droplets and the ITO pedestal heated surface at 1000<br>frames per second (fps) at a flow rate of 5.4 GPH and heat flux of $17\text{ W/cm}^2$ . ....                          | 73 |
| Figure 4.15 Sample video image of the liquid film and heated surface viewed through the<br>bottom of the pedestal at 3,000 fps at a flow rate of 5.4 GPH and heat flux of $17\text{ W/cm}^2$ . ....                     | 74 |

|  |    |
|--|----|
| Figure 4.16 Second sample video image of the liquid film and heated surface viewed through the bottom of the pedestal at 3,000 fps at a flow rate of 5.4 GPH and heat flux of 17 W/cm <sup>2</sup> . ..... | 74 |
| Figure 4.17 $G\Delta$ vs. $\Delta\theta$ for a PVC nozzle and two brass nozzles (unconfined flow). .....   | 75 |
| Figure 4.18 Nu vs. $G\Delta$ for a PVC nozzle and two brass nozzles (unconfined flow). .....   | 75 |
| Figure 4.19 $G\Delta$ vs. $\Delta\theta$ for variable nozzle-to-heater spacing (cap; $Q = 8 \times 10^{-6}$ m <sup>3</sup> /s). .....  | 77 |
| Figure 4.20 Nu vs. $G\Delta$ for PVC nozzle for variable nozzle-to-heater spacing (cap; $Q = 8 \times 10^{-6}$ m <sup>3</sup> /s). .....   | 77 |
| Figure 4.21 Electrode Geometries for electric body force studies: A) Example of initial electric Kelvin force electrode geometry, B) Example of inductive charging Coulomb force electrode geometry. ....  | 78 |
| Figure 4.22 Four initial electric Kelvin force electrode geometries; full cap geometry on right. 79  |    |
| Figure 4.23 $G\Delta$ vs. $\Delta\theta$ for full cap Kelvin force electrode: FC-72 for 0 kV-6 kV voltage. ....  | 80 |
| Figure 4.24 Nu vs. $G\Delta$ for PVC nozzle for full cap Kelvin force electrode: 0 kV-6 kV voltage. 80   |    |
| Figure 4.25 Calculated electric potential from CFD-ACE+ for full cap Kelvin force electrode at 6 kV electrode voltage. ....  | 81 |
| Figure 4.26 Calculated Kelvin force per mass normal to heater surface, from CFD-ACE+, for FC-72 and full cap Kelvin force electrode at 6 kV electrode voltage: various distances normal to heater. ....    | 81 |
| Figure 4.27 Second-generation Kelvin force electrode designed using CFD-ACE+. ....   | 82 |
| Figure 4.28 Heat transfer performance for second-generation Kelvin force electrode: $G\Delta$ vs. $\Delta\theta$ ; inset: enlarged view at high $G\Delta$ . ....   | 83 |
| Figure 4.29 Heat transfer performance for second-generation Kelvin force electrode: Nu vs. $G\Delta$ ; inset: enlarged view at high $G\Delta$ . ....   | 84 |
| Figure 4.30 Schematic of electrode configurations; left – electrode 1; right – electrode 2. ....   | 84 |
| Figure 4.31 Non-dimensional heat flux versus temperature difference for HFE-7000 using TFR heater and Coulomb force electrode 1 at flow rates of 6 and 8 GPH. ....   | 85 |
| Figure 4.32 Nusselt number versus non-dimensional heat flux for HFE-7000 using TFR heater and Coulomb force electrode 1 at flow rates of 6 and 8 GPH. ....   | 86 |
| Figure 4.33 Electric potential for Coulomb force electrode 1, computed using CFD-ACE+. ...   | 86 |
| Figure 4.34 E field magnitude (N/C) for Coulomb electrode 1, computed using CFD-ACE+. ...  | 87 |
| Figure 4.35 E field magnitude along the centerline for Coulomb force electrode 1, computed using CFD-ACE+, presented in N/C. ....  | 87 |
| Figure 5.1 Sample video images of liquid film on heater surface, at heater power = 57 W, FC-72 flow rate = 9.5 GPH. ....   | 90 |

## LIST OF TABLES

|  | Page |
|--|------|
| Table 2.1 Properties of coolant liquids at 25°C and 1 atmosphere pressure.....   | 8    |
| Table 2.2 Contact angle of FC-72 on various surfaces.....  | 9    |
| Table 2.3 Contact angle of HFE-7000 on various surfaces. ....  | 9    |
| Table 3.1 Parameters for simulatons of Labus’s experiments. Fluid properties at 20°C.....  | 17   |
| Table 3.2 Properties of water for simulations of the Liu and Lienhard (1989) experiment. ....                                      | 23   |
| Table 3.3 Computed results and experimental data for local Nusselt numbers.....  | 24   |
| Table 3.4 Parameters for the 100 $\mu\text{m}$ FC-72 drop splash simulation. ....  | 28   |
| Table 3.5 Parameters in the jet impingement simulations. ....  | 39   |
| Table 4.1 Computed droplet charge and resulting Coulomb force exerted on the droplet at the<br>top and bottom of electrode 1. .... | 88   |
| Table 5.1 Assumed parameter values for time scale analysis using FC-72 properties.....   | 90   |
| Table 5.2 Estimated time scales using parameters from Table 5.1.....   | 91   |

## CHAPTER 1 INTRODUCTION

In order to reach the higher levels of performance required in future aircraft and spacecraft, improved methods of thermal management must be developed. Beam (2000) reported that the Air Force envisioned future airborne laser and radar systems requiring heat rejection rates of between 100 kW and 1 MW. Marhefkey et al. (2004) noted that the total heat load from a Mach 2-4 Long Range Strike Aircraft could be about 15 MW, and estimated that laser weapon platforms may generate waste heat fluxes as high as  $1 \text{ kW/cm}^2$  ( $10 \text{ MW/m}^2$ ). Nor is the need for cooling at such high heat fluxes limited to aerospace applications. The ever increasing component density of integrated circuits tends to create higher heat fluxes in many electronic devices. Additionally, the quest for more compact and energy efficient devices of all kinds generally leads to designs involving higher temperatures, energy densities, and heat fluxes.

To achieve very high cooling rates, it is convenient (perhaps essential) to exploit the large latent heat of evaporation that characterizes boiling. Cooling by means of liquid to vapor phase change can be achieved in various configurations including pool boiling, flow boiling, liquid jet impingement boiling, and spray impingement boiling. The latter is believed to have the greatest potential in many cases. Spray cooling has achieved higher heat transfer coefficients and critical heat fluxes (CHF) than pool boiling or liquid jet impingement boiling (Mudawar, 2000; Chow et al., 1997; Tilton, 1989). With water as the working fluid, spray cooling has achieved a heat flux on the order of  $1 \text{ kW/cm}^2$  in terrestrial gravity (Lin and Ponnappan, 2003). Furthermore, the spatial distribution of the heat transfer coefficient is much more uniform in spray impingement boiling than in liquid jet impingement boiling (Bernardin et al., 1996). The main applications of spray cooling to date have been in quenching of aluminum and steel, in nuclear reactor safety devices, and in cooling lasers and electronic equipment.

For dense sprays directed normal to an upward-facing heated surface in a gravitational field, a liquid film forms on the surface and flows away from the stagnation point. At sufficiently high heat rejection rates vapor bubbles are formed in the film at nucleation sites as shown in Figure 1.1. These vapor bubbles tend to rise due to gravitational buoyancy and to be swept along the heater surface by the radial motion in the liquid film, resulting in efficient rewetting of the heated surface. The latter mechanism for rewetting of the heater surface is absent in pool boiling. As more of the impinging liquid boils, the vapor flowing away from the heated surface may prevent the smaller spray droplets from reaching the heater surface; this effect is thought to contribute to the onset of CHF (Chow et al., 1997).

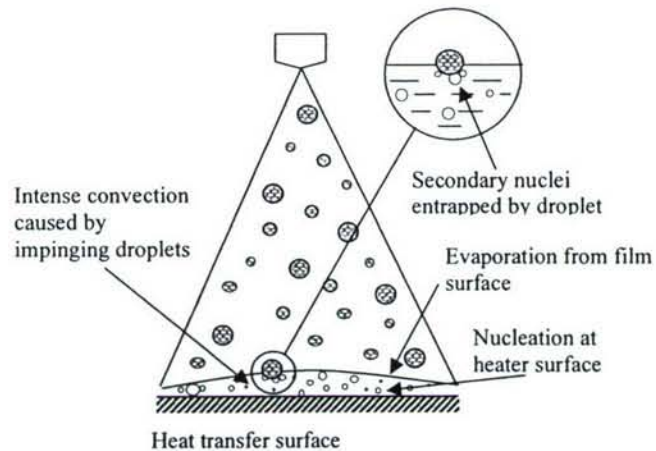


**Figure 1.1 Schematic of spray cooling droplet impingement (Redrawn from Chow et al. 1997).**

Tilton (1989) speculated that one reason spray cooling may be ideal for spacecraft is that it does not rely solely upon buoyancy forces for vapor removal and liquid supply. Yoshida, et al. (2001) found that spray cooling in the nucleate boiling regime was more effective in simulated microgravity ( $\mu g$ ) than in terrestrial gravity when water was used, but when the commercial coolant FC-72 was used, only a slight improvement was seen. Yoshida et al. simulated  $\mu g$  conditions by rotating their apparatus 180 degrees, changing the direction of the heated surface from upward facing to downward facing. (The degree to which changing surface orientation in terrestrial gravity accurately simulates  $\mu g$  is not clear.) Kato et al. (1994) also used orientation to simulate  $\mu g$  conditions, although they used a horizontal spray to simulate conditions of  $\mu g$ , and found data that was comparable to that of Yoshida et al.

A group at the Air Force Research Laboratory, Propulsion Directorate, Power Division (AFRL/PRPS) under the direction of Dr. Kirk L. Yerkes has been investigating the ability of spray impingement boiling to achieve higher heat transfer performance in a space and weight efficient manner under conditions of variable gravity. Baysinger et al. (2004) and Yerkes et al. (2006) describe the AFRL experiment, which has been flown several times on NASA variable gravity research aircraft. From its inception, the present (WVU) investigation of electrical body forces in spray impingement boiling has been closely coordinated with AFRL so as to complement and extend the non-electrical AFRL research. WVU researchers spent more than 6 man-months in residence at AFRL and held over a dozen meetings with AFRL personnel. The experimental apparatus used in the WVU research has been patterned closely after the AFRL design.

At the time when the WVU project was proposed, it was believed that  $\mu g$  conditions would limit spray impingement boiling heat transfer. If boiling takes place on Earth in the flowing film on an upward-facing surface, gravity creates a buoyant force that causes the vapor to rise, allowing the liquid to maintain contact with the surface. In the absence of gravity, it was thought that a

low thermal conductivity vapor blanket might form and remain at the surface, reducing the heat transfer coefficient and CHF dramatically and potentially leading to catastrophic overheating. Therefore, the original approach of the WVU project was to use electrical or magnetic forces to create an artificial “gravity” field directed toward the heated surface that would help to maintain liquid contact with the surface, thus enhancing  $\mu\text{g}$  heat transfer.

But as data from AFRL flight tests became available, it became apparent that spray impingement boiling heat transfer was actually somewhat enhanced under  $\mu\text{g}$  conditions, contrary to expectations (Yerkes, personal communication). This enhancement is now well established, although the mechanism remains unexplained. As a consequence of this discovery, the approach of the WVU project was changed to demonstrating the use of electrical or magnetic forces to produce a body force directed away from the upward facing heated surface. Such a force could cancel gravity near the heated surface, thus enhancing heat transfer and allowing the study of “ $\mu\text{g}$ ” heat transfer in Earth laboratories, with substantial savings of time and money compared to experiments on variable gravity research aircraft or other  $\mu\text{g}$  platforms.

The primary goal of the WVU project was to discover if electrical or magnetic forces could enhance spray impingement boiling; and, if this was possible, how it could be done most effectively. As will be explained in subsequent chapters, ground-based experiments, supported by computational modeling, did achieve modest increases in heat transfer coefficient and Nusselt number by using electrical forces. Further increases in performance are likely to result from more extensive parametric studies and from a better understanding of the relevant microphysics.

Chapter 2 of this report explains the physical basis and mathematical formulation of the electrical and magnetic forces that act on fluids. Chapter 3 describes the computational methods that were used, the modifications made to the commercial multiphysics code CFD-ACE+, and the results of the simulations. The experimental phase of this project is the subject of Chapter 4. Chapter 5 presents estimates of the time scales involved in spray impingement boiling. Conclusions and recommendations are summarized in Chapter 6.



## CHAPTER 2. PHYSICAL BASIS

### 2.1 Electromagnetic Body Forces in Fluids

For linear, isotropic media moving at nonrelativistic velocities, the general electromagnetic body force per volume can be written in SI units as (Hughes and Young, 1966, page 87)

$$\begin{aligned} \mathbf{f} = & \rho_e \mathbf{E} - (\epsilon_0 / 2) E^2 \nabla \kappa + (\epsilon_0 / 2) \nabla \left( E^2 \frac{\partial \kappa}{\partial \rho} \rho \right) \\ & + \mathbf{J} \times \mathbf{B} - (\mu_0 / 2) H^2 \nabla \kappa_m + (\mu_0 / 2) \nabla \left( H^2 \frac{\partial \kappa_m}{\partial \rho} \rho \right) \end{aligned} \quad (2.1)$$

where  $\mathbf{f}$  is the electromagnetic body force per volume [N/m<sup>3</sup>]

$\rho_e$  is the free electric charge per volume [C/m<sup>3</sup>]

$\mathbf{E}$  is the electric field [V/m]

$\epsilon_0$  is the permittivity of free space [F/m]

$E$  is the magnitude of the electric field [V/m]

$\kappa$  is the relative permittivity (a.k.a. dielectric constant) [dimensionless]

$\rho$  is the density (mass per volume) [kg/m<sup>3</sup>]

$\mathbf{J}$  is the current density [A/m<sup>2</sup>]

$\mathbf{B}$  is the magnetic induction [T]

$\mu_0$  is the permeability of free space [H/m]

$H$  is the magnitude of magnetic field [A/m]

$\kappa_m$  is the relative permeability [dimensionless]

Each term on the right side of Equation (2.1) represents a distinct force that in principle could be exploited to control fluid motion, although some can be readily dismissed from further consideration in the present context. The first term is the Coulomb force on free charges. It impels positive charges in the direction of the electric field vector and negative charges in the opposite direction. This force can be used to control the spray droplets if they are given a net charge, for example by means of an electrode. Motion induced by the Coulomb force is known as electrophoresis.

The second and third terms on the right side of Equation (2.1) result from the interaction of the electric field with induced or structural molecular electric dipoles. The second term is the permittivity gradient force and the third is the electrostrictive force. Motion due to the interaction of electric dipoles with a nonuniform electric field is known as dielectrophoresis. The physical interpretation of these terms is more immediate if they are rewritten, without approximation, as

$$\begin{aligned}
& -(\epsilon_0/2)E^2\nabla\kappa + (\epsilon_0/2)\nabla\left(E^2\frac{\partial\kappa}{\partial\rho}\rho\right) \\
& = (\epsilon_0/2)(\kappa-1)\nabla E^2 - \nabla\left\{\frac{\epsilon_0}{2}E^2\frac{\partial[(\kappa-1)\rho]}{\partial(1/\rho)}\right\}
\end{aligned} \tag{2.2}$$

The first term on the right side of Equation (2.2) is the electric Kelvin force. The permittivity of free space  $\epsilon_0$  is a positive universal constant, and the electric susceptibility  $(\kappa - 1)$  is positive for all types of matter. Therefore, the coefficient of the electric Kelvin force term is always positive. This means that the electric Kelvin force is always directed toward higher electric field regions. Because it is proportional to the gradient of the squared magnitude of the electric field, it is independent of the direction of the electric field. The electric susceptibilities of gases under ordinary conditions are on the order of  $10^{-2}$  or less while those of most liquids are of order 1 or greater. Therefore, in a liquid-gas two phase region, the electric Kelvin force on the liquid is much stronger than on the gas. The last term in Equation (2.2) is the gradient of an electric pressure. As such, it is an irrotational force. Usually, permittivity is proportional to density, and the term in braces is identically zero.

The fourth term on the right side of Equation (2.1) is the ponderomotive force. It represents the macroscopic integration of the Lorentz forces experienced by individual charges moving in a magnetic field. It becomes important in electrically conducting fluids such as liquid metals or plasmas and is the dominant force in the discipline known as magnetohydrodynamics. For electrically insulating coolants such as FC-72 and HFE-7000, the  $\mathbf{J} \times \mathbf{B}$  force is negligible. The fifth and sixth terms on the right side of Equation (2.1) result from the interaction of the magnetic field with induced or structural molecular magnetic dipoles and are magnetic analogs of the second and third terms. They are known as the permeability gradient force and the magnetostrictive force. As in the electric case, the physical interpretation of these terms is more immediate if they are rewritten, without approximation, as

$$\begin{aligned}
& -(\mu_0/2)H^2\nabla\kappa_m + (\mu_0/2)\nabla\left(H^2\frac{\partial\kappa_m}{\partial\rho}\rho\right) \\
& = (\mu_0/2)(\kappa_m-1)\nabla H^2 - \nabla\left\{\frac{\mu_0}{2}H^2\frac{\partial[(\kappa_m-1)\rho]}{\partial(1/\rho)}\right\}
\end{aligned} \tag{2.3}$$

The first term on the right side of Equation (2.3) is the magnetic Kelvin force. In contrast to the analogous electric term, its coefficient can be negative or positive depending on whether the fluid is diamagnetic or paramagnetic. In diamagnetic liquids such as FC-72, HFE-7000, or water, the magnetic volumetric susceptibility  $(\kappa_m-1)$  is about  $-10^{-5}$ ; for diamagnetic gases such as nitrogen it is about  $-10^{-8}$  at room conditions. In either case, the result is a force independent of the direction of the magnetic field vector and directed toward lower magnetic field regions. For realistically achievable magnetic fields, the

magnetic Kelvin force on diamagnetic fluids is negligible. For paramagnetic liquids such as liquid oxygen, the volumetric magnetic susceptibility is about  $+10^{-3}$ ; for paramagnetic gases such as gaseous oxygen it is about  $+10^{-6}$  at room conditions. Thus the magnetic Kelvin force impels paramagnetic fluids toward higher magnetic field regions. Owing to their larger magnetic susceptibilities, the magnetic Kelvin force could be significant in spray impingement boiling in  $\mu\text{g}$  if the coolant were paramagnetic. The last term on the right side of Equation (2.3) is the gradient of a magnetic pressure. It vanishes in the common case of permeability proportional to density.

It should be noted that artificial ferrofluids, which are suspensions of polymer coated ferromagnetic nanoparticles in dielectric liquids, have such large positive values of magnetic permeability that it is easy to create large magnetic Kelvin forces with rather weak magnets.

## 2.2 Coolant Properties

The selection of a coolant liquid plays a large role in determining which of the electromagnetic forces can have a significant magnitude in a given system. Many factors must be considered in making this selection. One of the most important properties of a coolant liquid for the spray cooling of electronic devices is that its boiling point be in the range of desired operating temperatures for the device to be cooled. A coolant should have high values of latent heat of evaporation, thermal conductivity, and specific heat to be a good heat transfer medium. It should have a low viscosity to reduce pumping costs and a low density to save weight in aerospace applications. It must be compatible with the materials of the system and have a high electrical resistivity and dielectric strength to avoid compromising electronic components. Other important considerations are flammability, toxicity, potential for environmental damage, cost, and availability.

Among the common choices for heat transfer liquids are water, water-ethylene glycol solutions, ethanol, carbon dioxide, and ammonia. In electronic applications, chlorofluorocarbons were widely employed for many years, but their use has been prohibited due to their adverse effects on the atmospheric ozone layer. They have been largely superseded by perfluorocarbons such as FC-72 ( $\text{C}_6\text{F}_{14}$ ) and segregated hydrofluoroethers such as HFE-7000. FC-72 and HFE-7000 are products of the 3M Company.

All of the fluids mentioned in the preceding paragraph are diamagnetic, so it is not practical to generate a significant magnetic Kelvin force in any of them. Significant magnetic Kelvin forces can be exerted on paramagnetic fluids, but liquid and gaseous oxygen are the only common fluids in this class. The cryogenic boiling point and reactivity of oxygen make it a poor candidate for the applications of present interest. Very large magnetic Kelvin forces can be created in ferrofluids, but they would be likely to deteriorate over time in a recirculating phase change system. Because no practical paramagnetic coolant was identified, it was decided to abandon the effort to use magnetic forces and to concentrate on using electrical forces.

The coolant in all of the AFRL experiments and many of the WVU experiments has been FC-72, a nonpolar dielectric. Unfortunately, liquid FC-72 has a rather small relative permittivity of 1.74 which limits the magnitude of the electric Kelvin force that can be developed. HFE-7000, a nonpolar dielectric with a significantly higher relative permittivity (7.4), was used in some of the WVU experiments in order to increase the electric Kelvin force. HFE-7000 was also used in some of the WVU Coulomb force experiments because it has a much lower resistivity than FC-72. The relevant mechanical, thermal, and electrical properties of FC-72 and HFE-7000 are compared to those of water in Table 2.1.

**Table 2.1 Properties of coolant liquids at 25°C and 1 atmosphere pressure.**

| Property                                | Water                    | FC-72                  | HFE-7000                |
|---|--------------------------|------------------------|-------------------------|
| Density [kg/m <sup>3</sup> ]            | 997.0                    | 1680                   | 1400                    |
| Dynamic viscosity [Pa·s]                | 8.904 x 10 <sup>-4</sup> | 6.4 x 10 <sup>-4</sup> | 4.48 x 10 <sup>-4</sup> |
| Surface tension [N/m]                   | 0.0718                   | 0.0085                 | 0.0124                  |
| Specific heat [J/kg·K]                  | 4180.9                   | 1100                   | 1300                    |
| Thermal conductivity [W/m·K]            | 0.6110                   | 0.057                  | 0.075                   |
| Prandtl number [-]                      | 6.093                    | 12.6                   | 7.92                    |
| Boiling Point [°C]                      | 100                      | 56                     | 34                      |
| Latent heat of vaporization [kJ/kg]     | 2260                     | 88 @ 56°C              | 142                     |
| Relative permittivity [-]               | 78.4                     | 1.72                   | 7.4                     |
| Resistivity [Ω·cm]                      | 18.18 x 10 <sup>6</sup>  | 1.0 x 10 <sup>15</sup> | 10 <sup>8</sup>         |
| Dielectric strength [kV] @ 0.1 inch gap | -                        | 38                     | ~ 40                    |

Mechanical and thermal properties of water are from Gebhart et al., 1988.

Electrical properties of water are from M. Chaplin, January 24, 2007. “Water Structure and Behavior,” <http://www.lsbu.ac.uk/water/data.html>, London South Bank University.

Properties of FC-72 are from “3M Fluorinert Electronic Liquid FC-72 Product Information”, undated.

Properties of HFE-7000 are from “3M Novec Engineered Fluid HFE-7000”, undated.

Because values of contact angle for FC-72 and HFE-7000 had not been published, WVU undergraduate student Ben Truschel used macrophotography of sessile drops in a purpose-built environmental chamber to measure contact angles of these liquids on the materials used in the WVU and AFRL experiments. The results presented in Tables 2.2 and 2.3 show that the fully wetted condition (0°) is a good approximation for these cases.

**Table 2.2 Contact angle of FC-72 on various surfaces.**

|                | <b>Contact angle in degrees</b> |             |             |             |
|----------------|---------------------------------|-------------|-------------|-------------|
| <b>Surface</b> | <b>15°C</b>                     | <b>25°C</b> | <b>35°C</b> | <b>40°C</b> |
| Teflon         | 2.0                             | 1.8 +/- 1   | 0           | 0           |
| Aluminum       | 3.7                             | 3.4 +/-1    | 3.8 +/-1    | 4.2 +/-1    |
| Plexiglas      | 3.0                             | 1.8 +/-1    | 2 +/-1      | 2.4 +/-1    |
| Glass          | 0                               | 0           | 0           | 0           |
| TFR            | 0                               | 0           | 0           | 0           |
| Stainless      | 0                               | 0           | 0           | 0           |

**Table 2.3 Contact angle of HFE-7000 on various surfaces.**

|                | <b>Contact angle in degrees</b> |             |             |
|----------------|---------------------------------|-------------|-------------|
| <b>Surface</b> | <b>15°C</b>                     | <b>25°C</b> | <b>35°C</b> |
| Teflon         | 2.2                             | 1.9 +/-1    | 1.7 +/-1    |
| Aluminum       | 3.5                             | 3.6 +/-1    | 5 +/-1      |
| Plexiglas      | 2.0                             | 2.5 +/-1    | 3 +/-1      |
| Glass          | 0                               | 0           | 0           |
| TFR            | 0                               | 0           | 0           |
| Stainless      | 0                               | 0           | 0           |



## CHAPTER 3. COMPUTATIONAL INVESTIGATIONS

This chapter reports the work performed in the computational phase of the project. Section 3.1 describes the computer program that was the main tool in these studies. Section 3.2 presents the results of simulations in which no electrical forces were present. Section 3.3 explains the simulations involving the Coulomb and electric Kelvin forces.

### 3.1 The Multiphysics Code CFD-ACE+

The motion of a fluid in an electric field, like the electric field itself, is governed by partial differential equations (PDEs) which express the governing physical laws in mathematical form. These equations are too complex to be solved analytically (except in strongly idealized cases), but they can be approximated numerically using the computer. To do so the equations are discretized so as to obtain a large set of coupled algebraic equations in which the unknowns are the values of the variables at discrete locations in the solution domain called nodes.

CFD-ACE+ uses the finite volume method explained in Patankar (1980) for the discretization of the partial differential equations. The solution domain is divided into a number of cells or control volumes, each with a node its centroid. The equations are integrated over each cell, and the resulting expressions are approximated using the current nodal values for that cell and its nearest neighbors. The resulting algebraic equations contain terms for accumulation, convection, diffusion, and creation of the various quantities. The result is a very large set of coupled algebraic equations, usually nonlinear ones, which must be solved iteratively at each time step. The solution of fluid flow problems in this manner is known as Computational Fluid Dynamics (CFD). When additional physical laws, such as the laws of electromagnetism, are considered, the term multiphysics is often applied.

The commercial multiphysics computer code CFD-ACE+, developed by CFD Research Corporation (CFDRC), was selected for use in this project, in part because it boasted the ability to simulate all of the physical processes of interest. A further reason was the opportunity for synergistic cooperation with an SBIR Phase 2 contract between CFDRC and AFRL. The goal of that contract was to enhance the microgravity ( $\mu g$ ) spray impingement boiling capabilities of the code. During the second year of the WVU project, the commercial rights to CFD-ACE+ were acquired by ESI Group, although CFDRC retained the rights to use and further develop the code. All of the simulations in this report were performed using single processor (Intel Pentium 4 or AMD Athlon XP 2800+) personal computers running Windows XP Professional.

CFD-ACE+ may be thought of as a computational Swiss Army knife. In addition to graphical pre- and post-processors, it contains 17 modules, each dealing with different physical phenomena. Unlike a Swiss Army knife, the modules are intended to be used in combination to model different types of problems. With a code of such factorial

complexity, it is impossible to exercise all of the allowable combinations of modules and options, much less to verify their accuracy. Consequently, it was necessary devote substantial effort to testing combinations of the modules of interest: Flow (the basic finite volume CFD solver), Free Surfaces (which uses the volume of fluid (VOF) technique to compute free surface motion), Heat Transfer, Spray, Electric, and Chemistry (which computes evaporation, as well as reactions).

Several cases in which the modules did not interact properly were discovered and corrected with assistance from the code developers. As an example, the Flow, Heat Transfer, and Spray modules were used to simulate an axisymmetric spray impinging on a heated surface. Initially the air and spray parcels were at 300 K and the surface was held at 360 K. Although evaporation was not simulated (the Chemistry module was not active), computations predicted a region of sub-300 K fluid. This physically impossible result was traced to an incorrect redistribution of thermal energy between the spray parcels and the air. The problem was corrected, and physically reasonable results were obtained.

The Flow module solves the basic continuity and momentum equations. The continuity or mass conservation equation requires that the time rate of change of mass in a control volume be equal to the net mass flowrate into the control volume. This may be written as

$$\frac{\partial \rho}{\partial t} + \nabla \cdot (\rho \mathbf{V}) = 0 \quad (3.1)$$

where  $\rho$  is the fluid density

$t$  is the time

$\nabla = \frac{\partial}{\partial x} \mathbf{i} + \frac{\partial}{\partial y} \mathbf{j} + \frac{\partial}{\partial z} \mathbf{k}$  is the del operator

$x$ ,  $y$ , and  $z$  are the coordinate directions

$\mathbf{i}$ ,  $\mathbf{j}$ , and  $\mathbf{k}$  are the unit vectors in the  $x$ ,  $y$  and  $z$  directions respectively

$\mathbf{V} = u \mathbf{i} + v \mathbf{j} + w \mathbf{k}$  is the velocity vector

$u$ ,  $v$ , and  $w$  are the velocity components in the  $x$ ,  $y$  and  $z$  directions respectively

The momentum equation has components in all three directions. The  $x$  momentum equation as given in the CFD-ACE+ manual (2004) is

$$\frac{\partial (\rho u)}{\partial t} + \nabla \cdot (\rho u \mathbf{V}) = \frac{\partial (-p + \tau_{xx})}{\partial x} + \frac{\partial \tau_{yx}}{\partial y} + \frac{\partial \tau_{zx}}{\partial z} + S_{Mx} \quad (3.2)$$

where  $p$  is the pressure

$\tau_{ij}$  are the nine viscous stress components.

$S_{Mx}$  is the source term for  $x$  momentum equation

In the present study, the source term expresses the electrical force per volume. Similarly the  $y$  and  $z$  momentum equations can be written as

$$\frac{\partial(\rho v)}{\partial t} + \nabla \cdot (\rho v \mathbf{V}) = \frac{\partial(-p + \tau_{yy})}{\partial y} + \frac{\partial \tau_{xy}}{\partial x} + \frac{\partial \tau_{zy}}{\partial z} + S_{My} \quad (3.3)$$

where  $S_{My}$  is the source term for y momentum equation and

$$\frac{\partial(\rho w)}{\partial t} + \nabla \cdot (\rho w \mathbf{V}) = \frac{\partial(-p + \tau_{zz})}{\partial z} + \frac{\partial \tau_{xz}}{\partial x} + \frac{\partial \tau_{yz}}{\partial y} + S_{Mz} \quad (3.4)$$

where  $S_{Mz}$  is the source term for z momentum equation.

For a Newtonian fluid the viscous stresses are proportional to the deformation rates of the fluid element. Using the Stokes hypothesis, the relation is (White, 1991)

$$\begin{aligned} \tau_{xx} &= 2\mu \frac{\partial u}{\partial x} - \frac{2}{3}\mu(\nabla \cdot \mathbf{V}) \\ \tau_{yy} &= 2\mu \frac{\partial v}{\partial y} - \frac{2}{3}\mu(\nabla \cdot \mathbf{V}) \\ \tau_{zz} &= 2\mu \frac{\partial w}{\partial z} - \frac{2}{3}\mu(\nabla \cdot \mathbf{V}) \\ \tau_{xy} &= \tau_{yx} = \mu \left( \frac{\partial u}{\partial y} + \frac{\partial v}{\partial x} \right) \\ \tau_{yz} &= \tau_{zy} = \mu \left( \frac{\partial v}{\partial z} + \frac{\partial w}{\partial y} \right) \\ \tau_{xz} &= \tau_{zx} = \mu \left( \frac{\partial u}{\partial z} + \frac{\partial w}{\partial x} \right) \end{aligned} \quad (3.5 \text{ a, b, c})$$

where  $\mu$  is the dynamic viscosity.

Substitution into the momentum equations results in the Navier-Stokes equations.

Although CFD-ACE+ allows other options, first order upwind differencing was used to approximate the convection terms in all of the simulations reported below. The pressure gradient in the momentum equation was solved using SIMPLEC algorithm (Van doormaal and Raithby, 1984) in which a guessed pressure field is updated and corrected until the velocity distribution satisfies the continuity equation. The Flow module contains no options for modeling turbulence. Turbulence can be modeled in CFD-ACE+ using the Turbulence module, but it was not used in this project.

Problems involving a deformable interface (free surface) separating immiscible fluids can be solved using the Free Surfaces module which tracks the interface location using the

Volume of Fluid (VOF) method invented by Hirt and Nichols (1981). In the VOF method, the two fluids are called the primary and secondary fluids. The secondary fluid volume fraction  $F$  is defined as the fraction of a cell filled by the secondary fluid. A cell containing only primary fluid has  $F = 0$ ; a cell filled by secondary fluid has  $F = 1$ . Any value of  $F$  between 0 and 1 in a cell means that it contains the fluid interface. Since the value of  $F$  for each fluid is conserved, the material derivative of  $F$  is zero.

$$\frac{\partial F}{\partial t} + \mathbf{V} \cdot \nabla F = 0 \quad (3.7)$$

The Free Surfaces module solves equation (3.7) simultaneously with the continuity and momentum equations. Given the value of  $F$  at every node, the free surface geometry is approximated according to the piecewise linear interface construction (PLIC) method. PLIC allows the fluid-fluid interface to take any orientation within the cell.

The value of  $F$  is also used to compute average values when a cell contains both primary and secondary fluids. If  $\varphi_1$  and  $\varphi_2$  represent the nodal values of any quantity per volume possessed by the primary and secondary fluids respectively, the value of  $\varphi$  assigned to that node is

$$\varphi = (1 - F)\varphi_1 + F\varphi_2 \quad (3.8)$$

Similarly, for any quantity per mass  $\lambda$ , the average value in a cell is obtained from

$$\lambda = [(1 - F)\rho_1\lambda_1 + F\rho_2\lambda_2] / \rho \quad (3.9)$$

The Heat Transfer module couples the energy equation to the continuity and Navier-Stokes equations so that nonisothermal flows can be modeled. Pure conduction in solid regions can also be solved using the Heat Transfer module. CFD-ACE+ solves the enthalpy form of the energy equation which is (ESI, 2004)

$$\begin{aligned} \frac{\partial(\rho h_o)}{\partial t} + \nabla \cdot (\rho V h_o) = \nabla \cdot (k \nabla T) + \frac{\partial p}{\partial t} + \left[ \frac{\partial(u\tau_{xx})}{\partial x} + \frac{\partial(u\tau_{yx})}{\partial y} + \frac{\partial(u\tau_{zx})}{\partial z} \right] \\ + \left[ \frac{\partial(v\tau_{xy})}{\partial x} + \frac{\partial(v\tau_{yy})}{\partial y} + \frac{\partial(v\tau_{zy})}{\partial z} \right] + \left[ \frac{\partial(w\tau_{xz})}{\partial x} + \frac{\partial(w\tau_{yz})}{\partial y} + \frac{\partial(w\tau_{zz})}{\partial z} \right] \end{aligned} \quad (3.10)$$

where  $h_o = i + (p/\rho) + (u^2 + v^2 + w^2)/2$  is the total enthalpy per mass  
 $i$  is the internal energy per mass  
 $k$  is the thermal conductivity.

The electric field  $\mathbf{E}$ , which is needed to calculate the electrical body forces that appear in the momentum equation, was computed using the Electric module of CFD-ACE+. In this module it is assumed that rate at which the magnetic field varies with time is small enough that the electrostatic form of the Maxwell equations govern the problem.

$$\nabla \times \mathbf{E} = 0 \quad (3.11)$$

$$\nabla \cdot \mathbf{D} = \rho_e \quad (3.12)$$

where  $\mathbf{E}$  is the electric field

$$\mathbf{D} = \varepsilon \mathbf{E} = \varepsilon_0 (1 + \chi) \mathbf{E} \quad \text{is the electric displacement} \quad (3.13)$$

$\varepsilon$  is the electric permittivity

$\varepsilon_0$  is the permittivity of free space

$\chi$  is the electric susceptibility

$\rho_e$  is the free electric charge per volume.

The irrotationality of the electric field expressed by Equation (3.11) which rests on the negligibility of  $(\partial \mathbf{B} / \partial t)$ , where  $\mathbf{B}$  is the magnetic induction, allows the introduction of the electrostatic potential  $\Phi$  such that its negative gradient is the electric field.

$$\mathbf{E} = -\nabla \Phi \quad (3.14)$$

Substituting equations (3.13) and (3.14) into Gauss's law (3.12) gives

$$\nabla \cdot [\varepsilon_0 (1 + \chi) (-\nabla \Phi)] = \rho_e \quad (3.15)$$

In regions of constant electric susceptibility, this reduces to the Poisson equation.

$$\nabla^2 \Phi = -\rho_e / \varepsilon \quad (3.16)$$

The Electric module distinguishes between metals and dielectrics (insulators). Metals are assumed to be at constant electric potential (voltage); therefore, the electrostatic equations are not solved inside the metal. However, Equation (3.16) is solved inside the dielectric regions of uniform permittivity. The appropriate jump conditions are automatically enforced between dielectrics of differing permittivity.

### 3.2 Simulations Without Electric Forces

In order to gain confidence in the code and to develop the capabilities needed to support the AFRL experiments, considerable effort was devoted to performing simulations in which there were no electric forces.

### 3.2.1 Round Jet Hitting a Sharp Edge Disk in Microgravity

The  $\mu\text{g}$  jet impingement experiments of Labus (1977) (see also Labus and DeWitt, 1978) were used to validate the Flow and Free Surfaces modules. Labus performed experiments in which a round liquid jet impinged on a sharp edge circular disk. The axis of the jet was normal to the disk and passed through its center, creating an axisymmetric geometry. The tests were made in a drop tower which provided about 2.2 s of  $\mu\text{g}$ . Labus reported 47 experiments in which he varied the jet velocity, jet diameter, disk diameter, and liquid (anhydrous ethanol and Freon TF (trichlorotrifluoroethane)).

These experiments were characterized by the radius ratio (jet radius over disk radius), the Reynolds number (Re), and the Weber number (We), defined as follows.

$$\text{Re} = \frac{\rho V R_o}{\mu} \quad (3.17)$$

where  $V$  is the jet velocity  
 $R_o$  is the nozzle radius.

$$\text{We} = \frac{\rho V^2 R_o}{\sigma} \quad (3.18)$$

where  $\sigma$  is the surface tension.

In all but two of his tests, Labus estimated that the Reynolds number was high enough to neglect the influence of viscosity. For each radius ratio, Labus observed three flow patterns. In order of increasing Weber number, he called them surface tension flow, transition flow, and inertial flow. Labus defined surface tension flow as the regime in which the liquid flows completely around the disk and along the support, with no separation at the disk edge. In transition flow, the liquid separates from the disk and the resulting liquid sheet either forms or tends to form a closed “water bell”. Inertial flow occurs when the liquid leaves the disk radially with no tendency to turn back towards the jet centerline during the experiment. As the radius ratio increased, the critical Weber numbers separating each flow regime decreased.

Three of Labus’s experiments were simulated. Case 1 was a surface tension flow; Cases 2 and 3 were inertial regime flows. Cases 1 and 2 had a jet radius to disk radius ratio of 0.33; Case 3 had a radius ratio of 0.5. All were modeled as two dimensional axisymmetric flows. The parameters used in these simulations are listed in Table 3.1.

**Table 3.1 Parameters for simulations of Labus's experiments. Fluid properties at 20°C.**

| Parameter                           | Case 1            | Case 2   | Case 3            |
|-------------------------------------|-------------------|----------|-------------------|
| Flow Regime                         | Surface tension   | Inertial | Inertial          |
| Fluid                               | anhydrous ethanol | Freon TF | anhydrous ethanol |
| Density $\rho$ [kg/m <sup>3</sup> ] | 789               | 1579     | 789               |
| Dynamic viscosity $\mu$ [Pa·s]      | 0.0012            | 0.0007   | 0.0012            |
| Surface tension $\sigma$ [N/m]      | 0.0223            | 0.0186   | 0.0223            |
| Nozzle Radius $R_o$ , [m]           | 0.005             | 0.005    | 0.005             |
| Nozzle radius / disk radius         | 0.33              | 0.33     | 0.5               |
| Inlet velocity $V$ [m/s]            | 0.377             | 0.4275   | 0.475             |
| Weber Number We                     | 25.1              | 77.6     | 59.6              |
| Reynolds Number Re                  | 1240              | 4830     | 2347              |

### 3.2.1.1 Surface Tension Flow Regime

The domain was sized to encompass the complete free surface of the impinging jet. It is bounded in part by the nozzle inlet, the sharp edge disk, the support column, and the axis of rotational symmetry. The remaining boundaries were modeled as fixed pressure outlets through which fluid can flow without restriction. At the inlet a constant velocity was specified. The contact angle of the liquid at the solid walls of the disk and the supporting column was specified to be 0° (fully wetting). The domain was divided into 14 different zones, each with a different grid resolution. The grid was refined near the disk edge where the flow was expected to turn inward to improve the accuracy of the solution. The complete domain comprised 10 182 nodes.

Initially the domain contained only air at rest. At  $t = 0$ , the liquid entered the domain at a velocity of 0.38 m/s. The jet hit the disk normally, turned, and started moving radially. Once the liquid reached the edge of the disk it turned around the sharp edge due to surface tension. The simulation was performed for 1.2 s of physical time and did not reach a steady state. Comparison of the computer animation with the high speed movie taken by Labus revealed good qualitative agreement. Figure 3.1 shows the simulated flow after 1.2 s. In this and many subsequent figures, the axisymmetric solution for positive radius is shown mirrored about the rotational axis to give a more realistic picture of the results. Figure 3.1 shows that the ethanol has turned around the sharp edge without separation. It may be compared with Figure 3.2, a photograph of a flow in the surface tension flow regime taken by Labus (1977). (Note that the numerical parameters for this photograph were not reported by Labus.) The flow pattern is similar except for the presence of three dimensional features in the experimental flow. Figure 3.3 shows the streamlines at  $t = 1.2$  s.

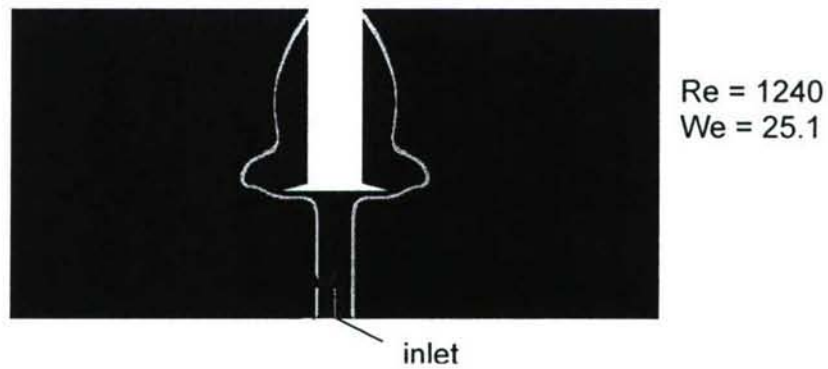
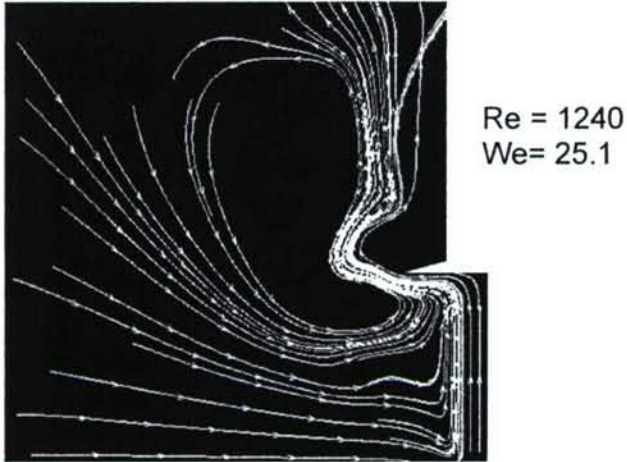


Figure 3.1 Labus Case 1 simulation at  $t = 1.2$  s mirrored on axis of symmetry. (Red represents ethanol and blue represents air.)



Figure 3.2 Surface tension case photographed by Labus (1977).



**Figure 3.3** Streamlines for Case 1 at 1.2 s. (Red represents ethanol and blue represents air.)

### 3.2.1.2 Inertial Flow Regime

The two dimensional axisymmetric computational domain for Cases 2 and 3 was generally similar to the Case 1 domain. The contact angle at solid boundaries was specified to be  $0^\circ$ . The grid was structured with 9 different zones and contained 22 357 cells. The grid distribution was refined near the sharp edge disk.

The Case 2 simulation was run for 0.5 s of flow time. The fluid entered the domain at a fixed velocity of 0.43 m/s, hit the disk normally, and spread radially past the edge of the disk. The radial spread of the liquid was always positive because inertia did not allow it to turn around the disk edge. Unlike the surface tension regime, there was no flow back toward the axis of symmetry. Figure 3.4 shows the flow at  $t = 0.3$  s. The leading edge of the liquid formed a ring (seen as a circular region in cross section) due to surface tension. This should be born in mind when comparing Figure 3.4 with the photograph of an inertial flow shown in Figure 3.5. (Again, Labus did not report the parameter values for Figure 3.5) There was no video available for this case. Figure 3.6 shows the streamlines at  $t = 0.3$  s.

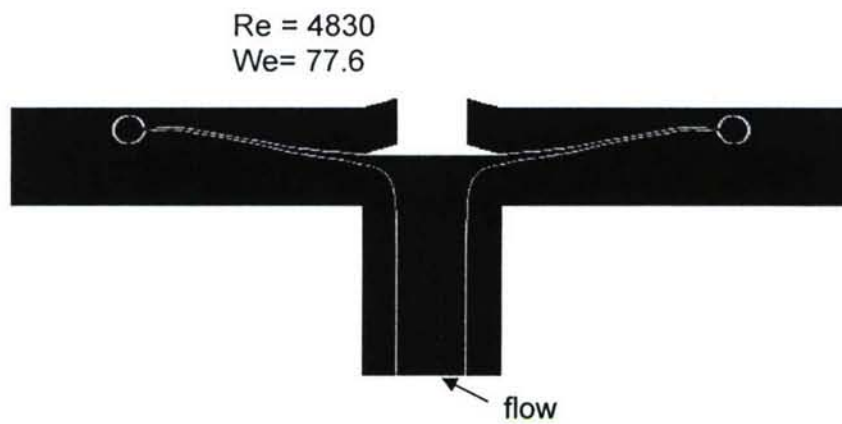


Figure 3.4 Labus Case 2 simulation mirrored on y axis at  $t = 0.3$  s. (Red represents Freon TF and blue represent air.)

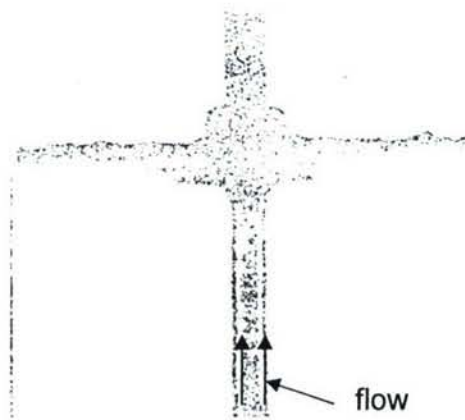
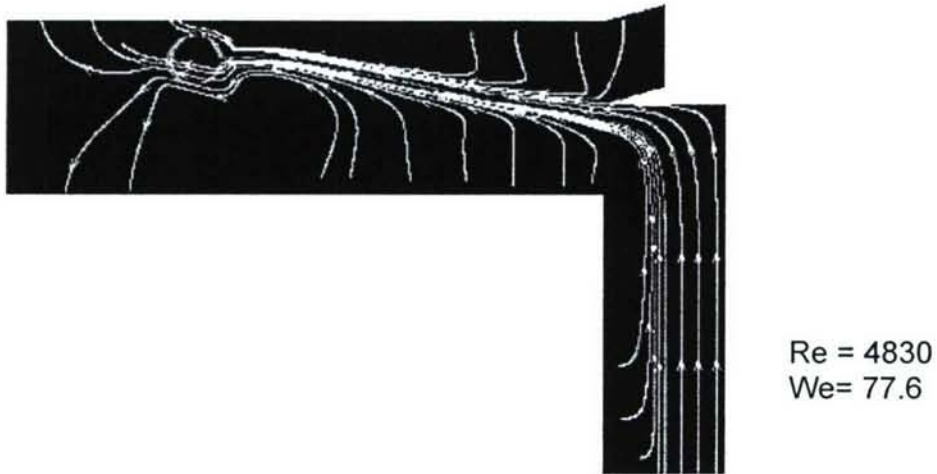
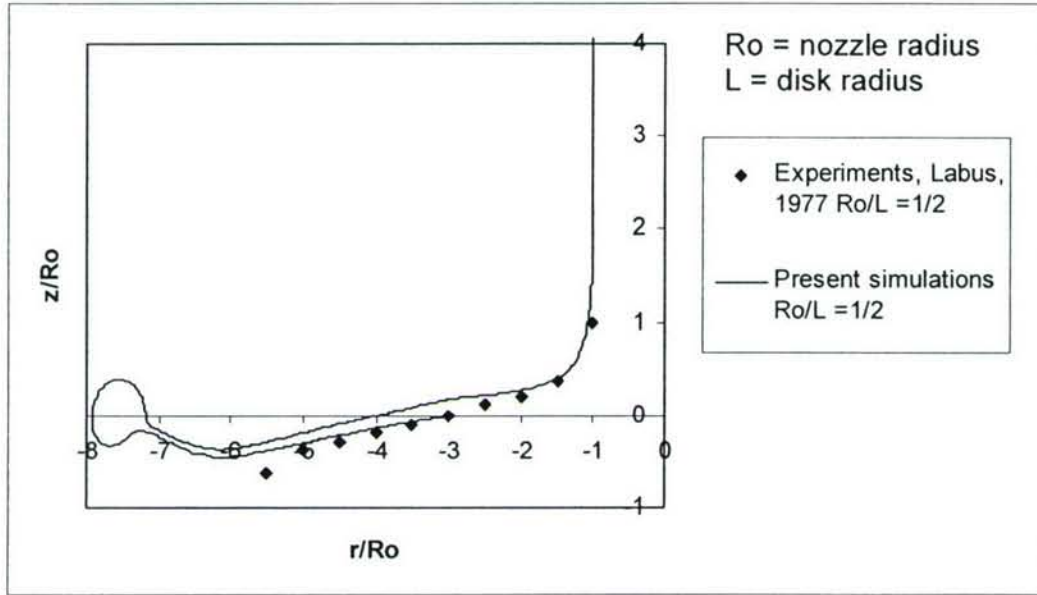


Figure 3.5 Inertial flow photographed by Labus (1977).



**Figure 3.6** Streamlines for Labus Case 2 simulation at  $t = 0.3$  s.

Figure 3.7 compares the nozzle-side free surface location measured by Labus with the Case 3 simulation. The comparison looks reasonably good but Labus did not specify the numerical values of the parameters in the experiment. Thus there may be a potentially significant difference in the  $We$  and  $Re$  numbers between the computation and the experiment. In addition, the simulation assumes axisymmetric flow whereas the experimental data is the average of the free surface coordinates on either side of the centerline as determined by Labus from photographs.



**Figure 3.7** Location of free surface for inertial flow in experiment (Labus, 1977, Figure 25) and Case 3 simulation.

### 3.2.2 Round Jet Hitting a Heated Surface

The nonisothermal capability of the CFD-ACE+ code was validated by simulating one of the experiments performed by Liu and Lienhard (1989). They studied the convective heat transfer to a circular free jet impinging normally at the center of an upward facing heated surface kept at uniform heat flux. The jet liquid was water at a temperature of 288 K, and the tests were done in Earth gravity. The dimensions of the rectangular surface were 78 mm by 152 mm. by 0.10 mm thick. The surface temperature distribution was inferred from measurements made by twelve evenly spaced thermocouples which were attached to the underside of the heater with glue. Free convection losses through the back of the heater were estimated by the experimenters to be negligible. The data obtained from the thermocouples along with the properties of water were used to calculate the local Nusselt numbers. Liu and Lienhard varied the heat flux and jet diameter.

The computational model was a two dimensional axisymmetric flow where the smaller dimension of the rectangular plate was taken as the radius of the surface. The Flow, Heat Transfer, and Free Surfaces modules were active. For small values of  $z/d$  (nozzle to surface distance  $z$  divided by the jet diameter  $d$ ),  $z/d$  does not influence the flow significantly. Since the distance between the orifice and the plate was not clearly defined in the paper, the simulation assumed  $z/d = 5$  with  $d = 2.58$  mm. The uniform heat flux was specified to be  $12\,378\text{ W/m}^2$ . The properties of water used in the simulations are shown in Table 3.2.

**Table 3.2 Properties of water for simulations of the Liu and Lienhard (1989) experiment.**

| Density [ $\text{kg/m}^3$ ]<br>[ $T$ ] = K | Kinematic viscosity [ $\text{m}^2/\text{s}$ ] | Surface tension (N/m) | Thermal expansion coefficient [ $\text{K}^{-1}$ ] | Thermal conductivity [ $\text{W}/(\text{m}\cdot\text{K})$ ] | Velocity (m/s) | Heat flux ( $\text{W}/\text{m}^2$ ) |
|--|---|-----------------------|---|---|----------------|-------------------------------------|
| 1206.68-<br>$0.6957\cdot T$                | 1E-6  | 0.0725                | 0.0004  | 0.597   | 24.2           | 12 378                              |

A unique modeling technique was used to accelerate the solution to a steady state since the conventional method was excessively time consuming. First, a fine (33 048 cell), nonuniform grid was used to obtain an isothermal steady state solution. Then a coarse grid containing 2580 cells but covering the same domain was used to obtain a steady state heat transfer solution. The temperature distribution from the coarse grid steady state heat transfer solution was mapped onto the fine grid steady state isothermal solution and used as an initial condition to obtain the final coupled steady state heat transfer solution. The steady state flow pattern and streamlines from the fine grid are shown in Figure 3.8.

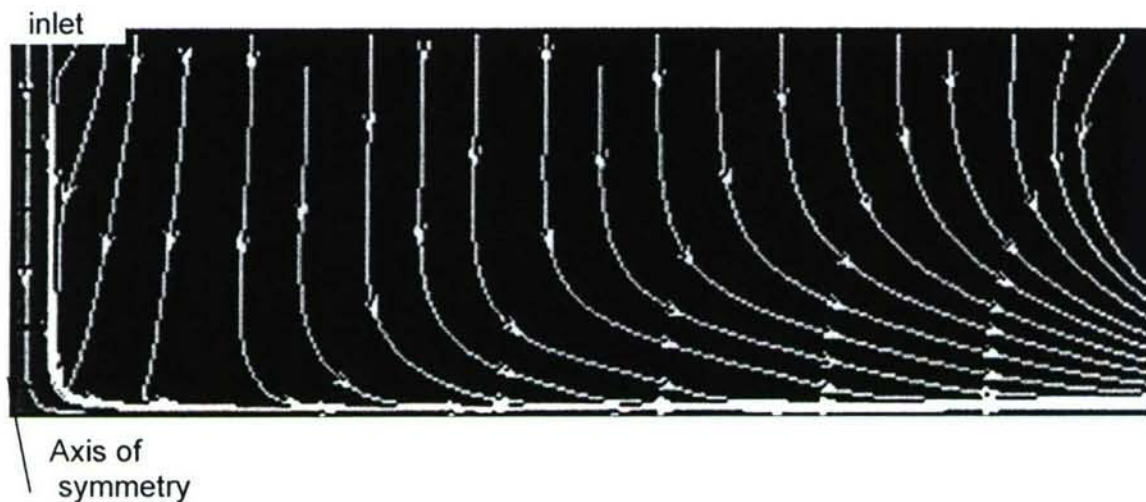


**Figure 3.8 Streamlines for liquid jet impingement on a uniformly heated surface at steady state conditions. (Red represents water, blue represents air.)**

Beyond the jet radius, the heat transfer solutions for the coarse and fine grids matched well. However, there was a significant difference within the jet radius between the coarse and fine grids. This is most likely due to the thinness of the thermal boundary layer in the liquid jet impingement area. The grid was not refined further to avoid excessive computational time since the current solution was already close to the experimental result, as shown below.

The local Nusselt number  $Nu_r$  is defined as

$$Nu_r = \frac{q r}{k(T_w(r) - T_f)} \quad (3.19)$$

where  $q$  is the wall heat flux

$r$  is the radial position

$T_w(r)$  is the local wall temperature

$T_f$  is the fluid temperature at impingement.

The computed and experimental Nusselt numbers (digitized from Liu and Lienhard, 1989, Figure 6a) are compared in Table 3.3. The difference at  $r/d = 3.3$  is 13.6%, slightly above than the reported experimental uncertainty of 13%. At the larger radii, the discrepancy is well within the experimental uncertainty.

**Table 3.3 Computed results and experimental data for local Nusselt numbers.**

| $r/d$ | $Nu_r$<br>experiment | $Nu_r$<br>computed | Percent<br>difference |
|-------|----------------------|--------------------|-----------------------|
| 3.3   | 555                  | 631                | 13.64                 |
| 7.75  | 795                  | 842                | 5.91                  |
| 11.6  | 900                  | 955                | 6.06                  |

### 3.2.3 Drop Hitting a Wall

A spray consists of a large number of discrete liquid droplets, so a single droplet can be thought of as the limiting case of a dilute spray. A droplet may impact a dry wall or a wall covered by a liquid film, which may be generated by the spray itself. Discrete droplets can be solved using Lagrangian equations whereas a fluid in continuous form can best be solved using Eulerian equations. To correctly model the details of the interaction of a spray drop and a liquid layer requires coupling the Lagrangian and Eulerian forms of the conservation equations. The nozzles in the WVU experiments are estimated to generate about  $10^8$  drops/s so a detailed simulation is practically impossible at present and for the foreseeable future. Therefore, some parameterization of the process is necessary.

The physics of the interaction of a spray with a solid surface depends upon a large number of factors which may include the surface roughness, surface orientation, liquid-wall contact angle, wall temperature, droplet size, droplet momentum, film depth, film velocity, and liquid properties. Because of this complexity, much of what is known about drop and spray interactions with solid surfaces has come from experimental studies.

Mundo et al. (1995) performed experiments on single liquid droplets impinging on a dry wall to establish a splashing limit. Their definition of splashing was satisfied when

secondary droplets were ejected with some liquid left behind on the wall. Mundo et al. found that splashing from a smooth wall occurred for

$$K = Oh Re^{1.25} > 57.7 \quad \text{with } Re > 150. \quad (3.20)$$

where  $K$  is the Mundo et al. dry wall splash parameter

$$Oh = \frac{\mu}{\sqrt{\rho \sigma d}} \text{ is the Ohnesorge number}$$

$d$  is the droplet diameter.

Mundo et al. based their Reynolds number on the drop diameter and the component of droplet velocity normal to the wall.

### 3.2.3.1 Drop Hitting a Dry Wall

Pasandideh-Fard et al. (1996) performed experiments with water droplets of 2 mm diameter hitting a dry wall normally at 1 m/s. The droplet spread to a maximum diameter and then rebounded from the wall. This case was simulated as an axisymmetric flow using the Flow and Free Surfaces modules with a uniform 4800 cell grid. Gravity was not included due to the small size of the droplet. The liquid was water at standard conditions and  $We = 200$ . Contact angles of  $90^\circ$ ,  $100^\circ$ , and  $120^\circ$  were simulated because Pasandideh-Fard et al. reported a contact angle of  $90^\circ$  for equilibrium and an advancing contact angle of  $110^\circ$ . Figures 3.9 through 3.13 show the evolution of the spreading droplet at various times for a contact angle of  $100^\circ$ . The expansion and subsequent contraction of the drop are evident. Note the formation of a bubble as the droplet rebounds.

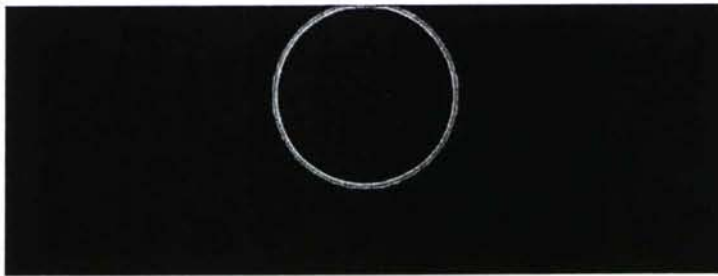


**Figure 3.9** Water droplet at time = 0 s.

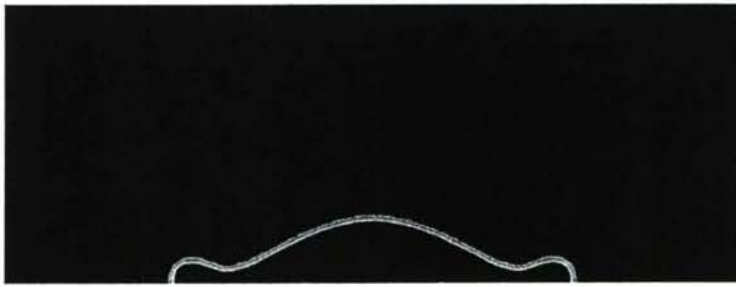


Figure 3.10 Water droplet with  $100^\circ$  contact angle at time = 2.5 ms.

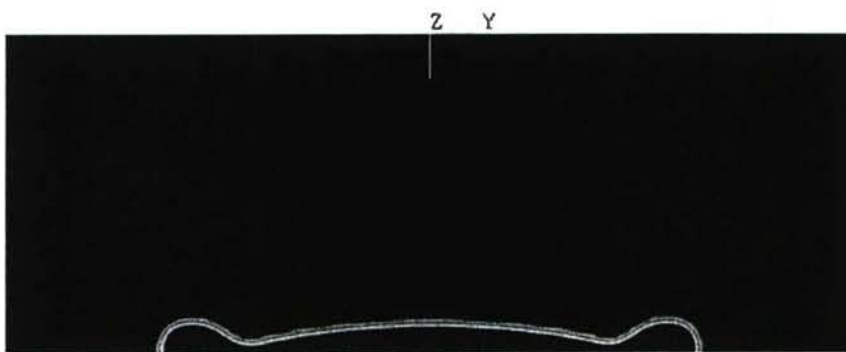
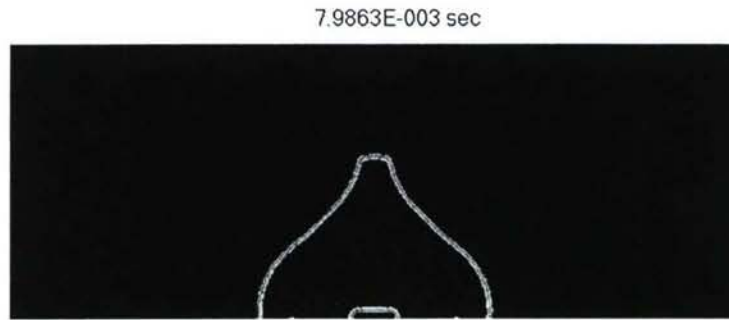


Figure 3.11 Water droplet with  $100^\circ$  contact angle at time = 3.5 ms.

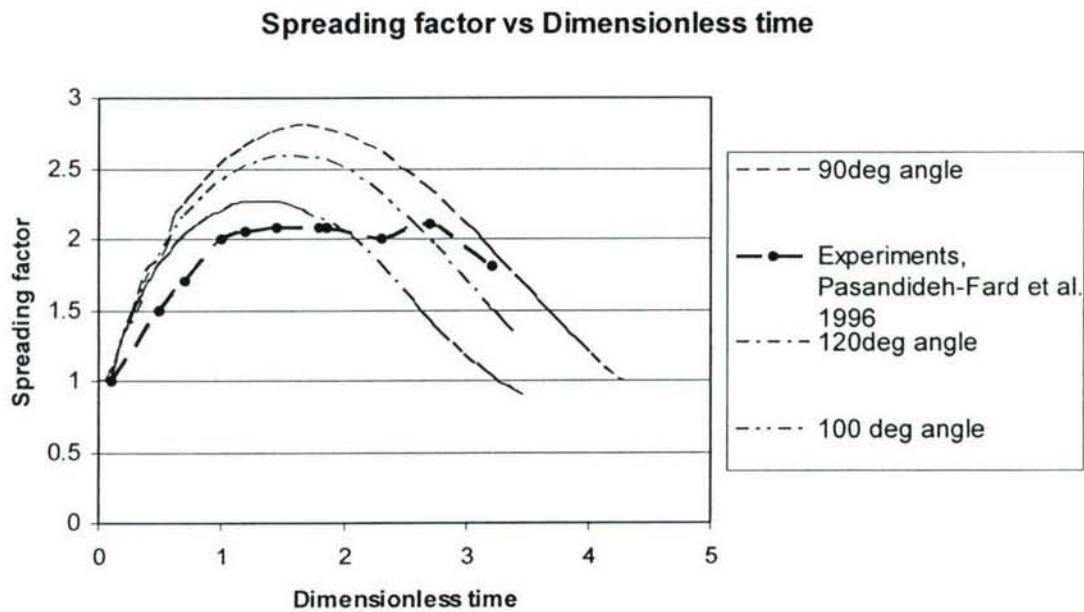


Figure 3.12 Water droplet with  $100^\circ$  contact angle after time = 6.5 ms.



**Figure 3.13** Water droplet with  $100^\circ$  contact angle at time = 8 ms.

These simulations reveal the sensitive dependence of spreading factor (diameter of the wetted surface to the droplet diameter) on contact angle shown in Figure 3.14. The time was made dimensionless by the ratio of the initial droplet diameter to its initial velocity.



**Figure 3.14** Droplet spreading factor as a function of time for various static contact angles.

### 3.2.3.2 Drop Hitting a Wet Wall

Cossali et al. (1997) reported experiments on the impact of single droplets on surfaces coated by a pre-existing liquid film. Cossali et al. describe the thin film case as consisting of two different regimes depending upon the surface roughness. When the film thickness is much greater than the surface roughness, roughness is not expected to influence splashing significantly, whereas when the film thickness is of the order of the surface roughness it will have a significant effect on splashing. Cossali et al. found that splashing occurred for

$$Y = \frac{We Oh^{-0.4}}{2100 + 5880 \delta^{1.44}} > 1 \quad \text{for } 0.1 < \delta < 1 \quad \text{and} \quad Oh > 0.007 \quad (3.21)$$

where  $Y$  is the Cossali et al. wet wall splash parameter

$$\delta = h / d$$

$h$  = fluid layer height.

At first glance, criteria (3.20) and (3.21) appear quite different, but it can be shown that  $We Oh^{-0.4} = (Re^{1.25} Oh)^{1.6}$ . Although not intended for the dry wall case, criterion (3.21) with  $\delta = 0$  reduces to the same form as (3.20), but with a different critical  $K$  (119 rather than 57.7).

Several simulations were performed with FC-72 at standard atmospheric conditions. The properties of FC-72 that were used are given in Table 1.1 except that the surface tension was taken as 0.01 N/m. The simulations were for single drop impingement normal to a liquid layer with different drop velocities and layer thicknesses. Gravity was neglected due to the small size of the droplets. The results were in agreement with the splashing criterion (13.22) of Cossali et al..

As an example, consider the simulation of an FC-72 droplet of 100  $\mu\text{m}$  diameter hitting a motionless liquid layer of 80  $\mu\text{m}$  thickness with a velocity of 10 m/s. The parameters defining this case are shown in Table 3.4.

**Table 3.4 Parameters for the 100  $\mu\text{m}$  FC-72 drop splash simulation.**

| $d$ [m]  | $h$ [m]  | $V$ [m/s] | Re   | We   | Oh     | $\delta = h/d$ | $Y$  | K   |
|----------|----------|-----------|------|------|--------|----------------|------|-----|
| 1.00E-04 | 8.00E-05 | 10        | 2630 | 1680 | 0.0156 | 0.800          | 1.39 | 293 |

The two dimensional axisymmetric domain extended 1500  $\mu\text{m}$  in the radial direction and 900  $\mu\text{m}$  normal to the wall. The outer vertical boundary was impermeable and the upper boundary was a constant pressure surface. The domain was uniformly discretized with 54 000 cells. The location of the droplet and the liquid layer at  $t = 0$  is shown in Figure 3.15.

Figure 3.16 shows the crown formed after the droplet hits the layer at  $t = 0.15$  ms. In Figure 3.17 the crown has collapsed into the film and the liquid has started moving in to form a central jet containing a bubble. Figure 3.18 shows the central jet, sometimes known as a Worthington jet, after pinching off a droplet from its top surface. Note that the bubble is in the drop.

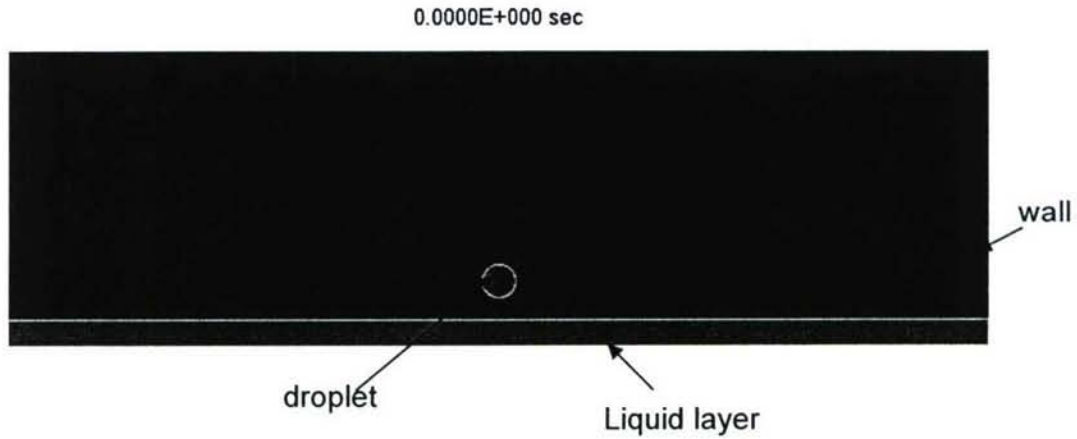


**Figure 3.15** Droplet and liquid layer at zero time. (Blue represents air and pink represents FC-72.)

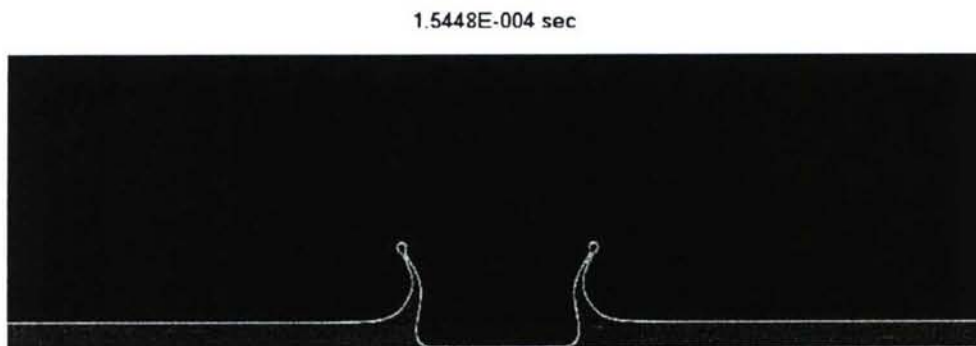


**Figure 3.16** Drop splash at 0.15 ms.

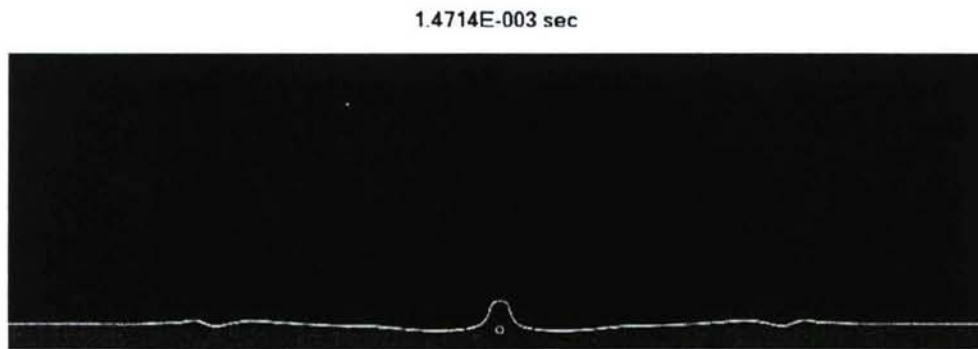


**Figure 3.17** Drop splash at 1.5 ms.

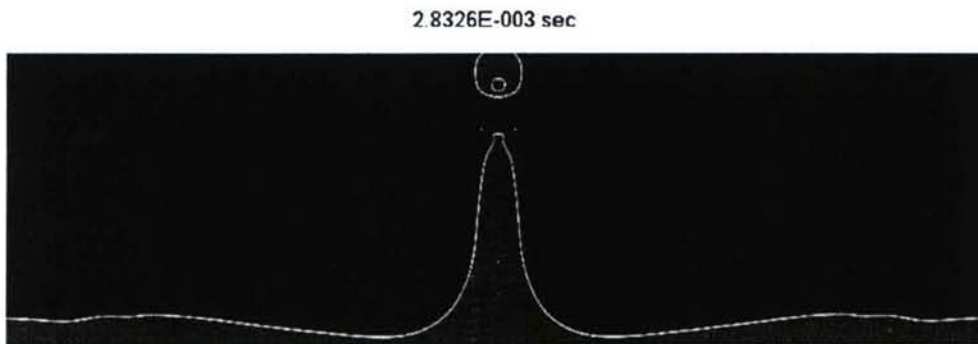


**Figure 3.18** Drop splash at 2.8 ms.

Because certain features of the flow were thin compared to the cell size, this simulation was rerun with a much finer grid. A special technique called block coarsening was used to save a significant amount of simulation time. While generating the grid in the CFD-ACE+ preprocessor CFD GEOM, the domain can be subdivided into smaller blocks. With block coarsening two adjacent blocks can have different numbers of cells. For example, at the interface one block can have two cells matched to one cell of the adjacent block, thus creating two to one cell matching. The primary advantage of this technique is that the grid can be refined only where it is needed most.

The refined grid contained 398 242 cells at the start of the simulation. The developing simulation was halted to further refine the grid where needed to completely resolve the

flow. This was done repeatedly so that the number of cells kept increasing during the simulation. Details not seen in the original uniform grid simulation were revealed with the finer grid. Figures 3.19 and 3.20 show the formation and evolution of a thin jet prior to the formation of the crown seen in Figure 3.16. This jet is apparently the jet first observed by Thoroddsen (2002) in his single drop physical experiments. Thoroddsen reported runs with  $(Re, We)$  pairs of (1080, 4170), (4640, 2190), and (480, 2370). The values of the present simulation (2630, 1680) are close to this range. Figure 3 of Mundo et al. (1998) shows a similar jet appearing in their numerical simulation of a drop impacting a liquid layer, but they do not report values of  $Re$  or  $We$ . In the present simulation, there were 429 510 cells in the grid when this jet was observed. The simulation was suspended at this time since it became impractical to run it any further. The maximum resolution used  $0.3 \times 0.3 \mu\text{m}$  cells which are 333 times smaller than the diameter of the droplet. Even at this resolution there were only four cells across the width of the jet ( $1.2 \mu\text{m}$ ). This simulation showed that even though a relatively coarse grid can reproduce the experimental splashing criterion, the fine details of the flow can be captured only with an extremely fine grid.

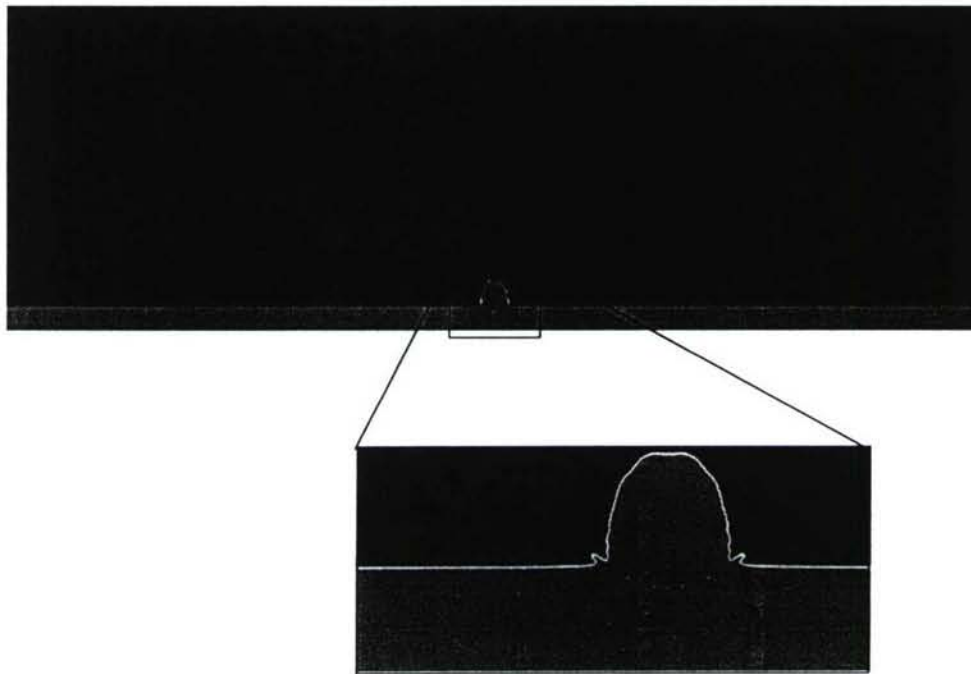


**Figure 3.19** Drop splash at 0.01 ms.

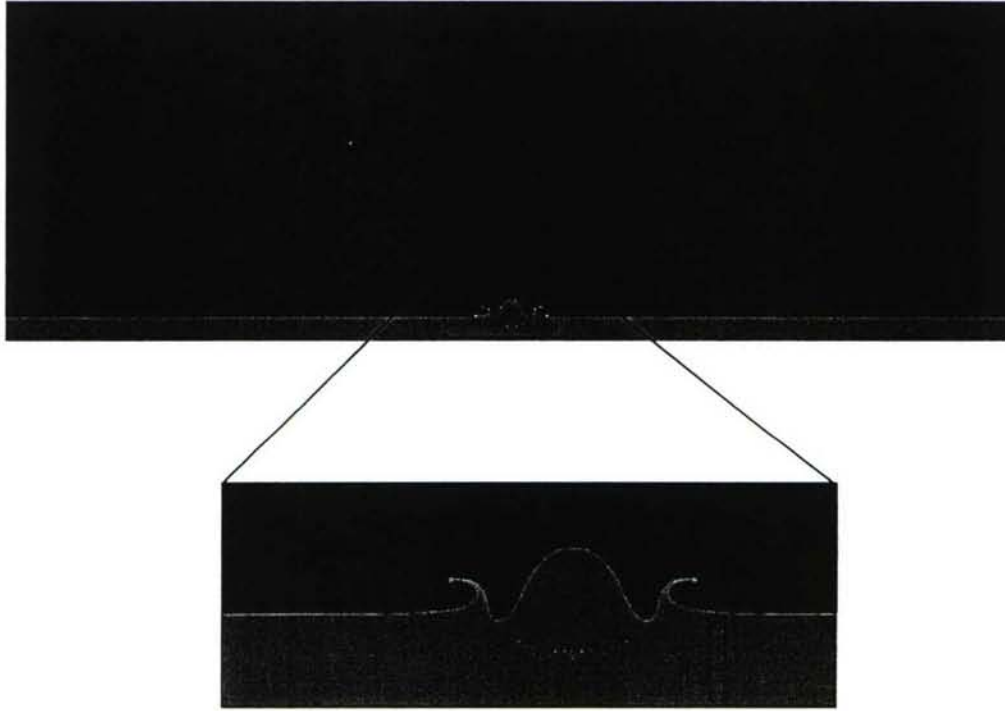


**Figure 3.20 Drop splash at 0.014 ms.**

### **3.3 Simulations with Electric Forces**

As noted in Section 2.1, there are two types of electrical forces that offer the potential to control spray heat transfer in  $\mu\text{g}$  or to mimic  $\mu\text{g}$  conditions on Earth: the Coulomb force and the Kelvin force. This section describes the modifications that were made to the CFD-ACE+ code to simulate these forces.

#### **3.3.1 Coulomb Force**

By comparing Equation (2.1) and Equations (3.2), (3.3), and (3.4) it can be seen that the momentum source term for the Coulomb force is given in vector form by

$$\mathbf{S}_M = \rho_e \mathbf{E} \quad (3.22)$$

The Coulomb force has long been used to control the motion of paint and pesticide sprays because the droplets can be readily charged by means of contact or induction mechanisms. The magnitude of the Coulomb force is restricted only by the limit on the droplet charge (the Rayleigh limit to prevent drop disintegration) and the limit on the electric field to avoid dielectric breakdown of the air (arcing). Given the spatial distribution of  $\rho_e$ , Equation (3.15) is solved by the Electric module for the electric potential  $\Phi$  from which  $\mathbf{E}$

can be found using Equation (3.14). This allows the momentum source term to be determined. In the case of a spray, this force alters the charge distribution which then changes the electric field. In its commercial form, CFD-ACE+ did not account for the change in the electric field due to the change in the charge distribution. Nor did it allow for the Coulomb forces between droplets to be found. These capabilities were added to the code by modifying eight files in the source code. Simulations of the motions of two like point charges were compared to analytical solutions in order to verify that these changes were done correctly. The modifications were communicated to the code developers for incorporation in future versions of CFD-ACE+.

As described in Section 3.2.3, the mechanical interaction of a droplet with a dry wall or a liquid film is quite complicated. When the droplet is charged, the situation becomes even more complex. For example, the disposition of the charge carried by an incoming droplet when it impacts a wall is poorly understood. Two new wall boundary conditions were added to the code to address this issue in an approximate manner for two common situations. If the wall is specified as insulating, the droplet maintains its charge when it meets the wall. If the wall is specified as grounded, the droplet instantly loses its charge upon contact. However, no boundary condition was formulated to deal with the general case.

In principle, the interaction between a spray and a liquid layer should be modeled by using the Spray and Free Surfaces modules. In this case the commercial version of the code allows the user to select from three options: convert the spray material to the primary fluid, convert to the secondary fluid, or convert to neither fluid. It is clear that none of these options is realistic for the present problem, so the transfer of mass, momentum, and energy between a spray and a film cannot be accurately modeled using the commercial code. What happens to the charge when a charged spray impacts a liquid film covering a wall remains a question whose answer appears to be of paramount importance when boiling takes place.

### 3.3.2 Electric Kelvin Force

By comparing Equation (2.2) and Equations (3.2), (3.3), and (3.4), it can be seen that the momentum source term for the electric Kelvin force is given in vector form by

$$\mathbf{S}_M = (\epsilon_0/2)(\kappa - 1)\nabla E^2 \quad (3.23)$$

This force depends on the pattern of the electric field and on the distribution of material. The electric Kelvin force was incorporated in the CFD-ACE+ code such that the Electric and Flow modules were fully coupled.

The present project included experimental studies of spray impingement cooling. As described in greater detail in Chapter 4, the WVU apparatus was patterned after one used in an AFRL research program which did not consider electrical forces. Figure 3.21 shows the key parts of the apparatus schematically. These include the spray nozzle, cap, pedestal,

sump, and electric heater. The spray from the nozzle impinges normally on the heated top surface of the cylindrical pedestal. The cap confines the flow and thus aids in the fluid management. The slots in the sump provide a way for excess fluid to be diverted back into the flow loop. The cap, pedestal, and sump are nonconducting dielectrics whereas the heater is a metallic conductor. Both conducting and nonconducting nozzles were used in the experiments. In the Kelvin force experiments, the nozzle was nonconducting.

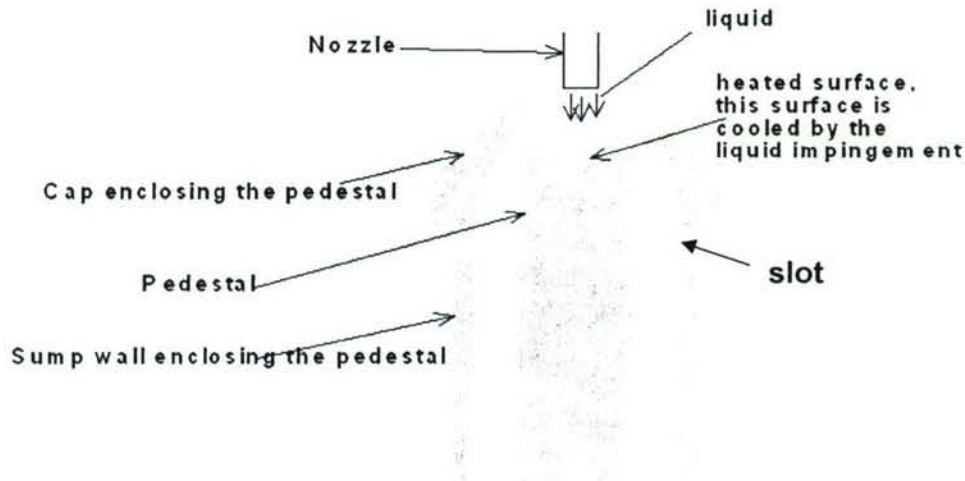


**Figure 3.21 Schematic of apparatus (axisymmetric geometry).**

In the WVU experiments, various electrode geometries were tested in order to produce Coulomb and Kelvin forces with the intention of increasing the heat transfer. After several intuitively designed Kelvin force electrodes failed to produce a significant effect, a second-generation Kelvin force electrode system was designed using the CFD-ACE+ multiphysics code. Since it is proportional to  $\nabla E^2$ , a Kelvin force will be present as long as the electric field varies in space. It was desired that this force be as uniform as possible in the region near the impingement surface and be directed away from the surface. Knowing that electric field lines needed to get denser when moving away from the heated surface, several electrode configurations were tested using the CFD-ACE+ Electric module. The goal was maximize the magnitude and uniformity of the surface-normal component of  $\nabla E^2$  in the region where the liquid film would form.

The final system consisted of three electrodes. As shown in Figure 3.22 one electrode was attached to the spray nozzle, another to the conical flow management cap, and the third was attached to the cylindrical pedestal. The electrode attached to the cap forced the electric field lines to turn towards it just above the impingement surface thus creating a significant gradient in  $E^2$ . Since the experimental geometry was essentially axisymmetric, the electrode design was also axisymmetric. The metallic heater is an equipotential surface so that the field lines must be normal to its surface. Thus if the heater would have

remained the top surface of the pedestal, the chance of getting a uniform Kelvin force adjacent to it would have been almost nil. Figure 3.22 shows that for this reason the heater was moved to be about 2 mm below the top surface of the pedestal. The electric field was calculated by assuming HFE-7000 was present in the region shown in Figure 3.22. The solid dielectrics (glass and PTFE) were assumed to have a dielectric constant of 5.

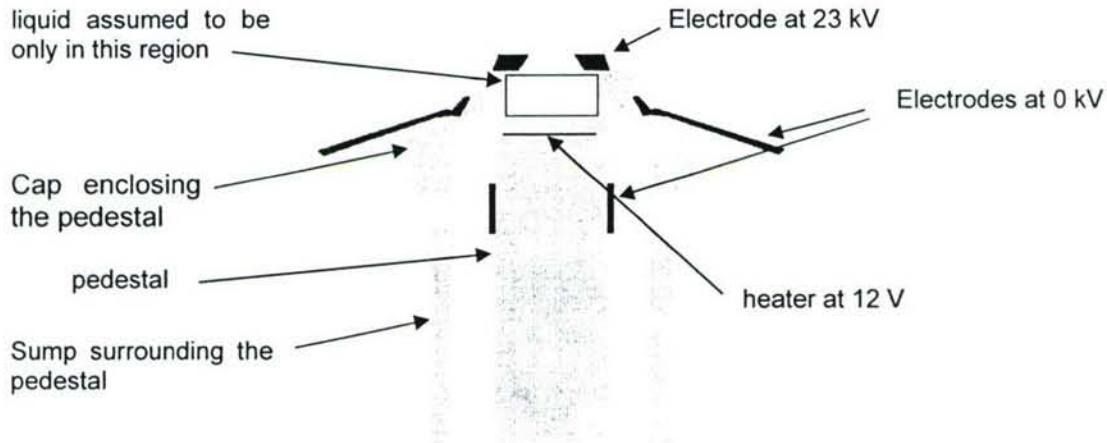


**Figure 3.22 Location of the electrodes. (Conductors are shown in red or black; dielectrics are shaded gray.)**

Figure 3.23 shows the electric field lines when potentials of 23 kV, 0 V, and 0 V are applied to the respective electrodes. The electric field lines begin on the high voltage electrode (shown in red in Figure 3.23) and terminate on the grounded electrodes (shown in black in the Figure 3.23) or extend to infinity.

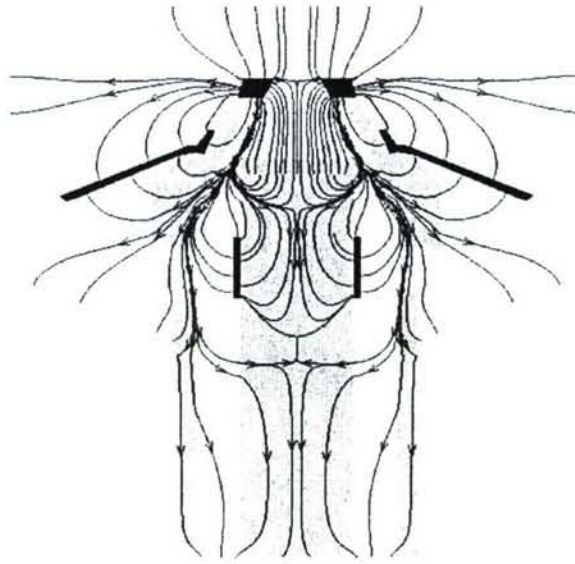


**Figure 3.23 Electric field lines.**

The values of  $\nabla E^2$  were obtained from the computed values of  $E$  by using backward or forward differencing next to the domain boundaries and central differencing in the interior. Lines tangent to  $\nabla E^2$  are shown in Figure 3.24. These lines point in the negative  $x$  direction, away from the impingement surface. The ratio of  $x$ -force to mass (N/kg) over the entire domain is shown in Figure 3.25. This ratio averages around 5 for the region within 200  $\mu\text{m}$  from the impingent surface. Figure 3.26 shows the  $x$  direction Kelvin force to mass ratio along the radius of the impingement surface at various axial distances from the surface. This force is directed away from the surface as desired. Figure 3.27 shows the  $y$  direction Kelvin force to mass ratio along the radius of the impingement surface at various axial distances. This force is in the positive radial direction and varies only slightly in the 175  $\mu\text{m}$  thick region adjacent to the surface.

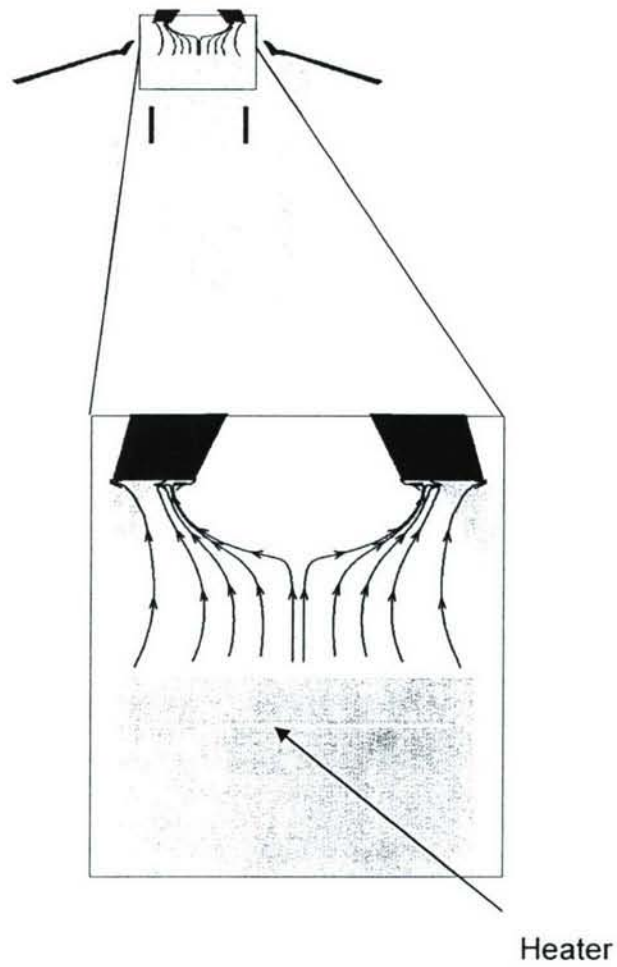


Figure 3.24 Lines tangent to  $\nabla E^2$ .

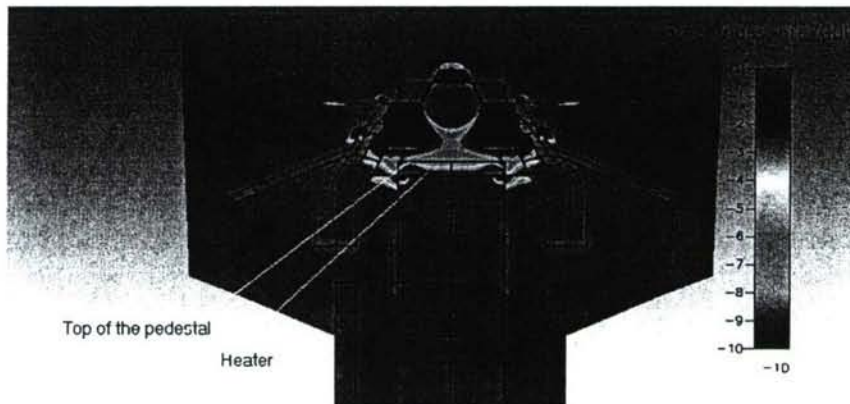


Figure 3.25 X direction (axial) Kelvin force to mass ratio.

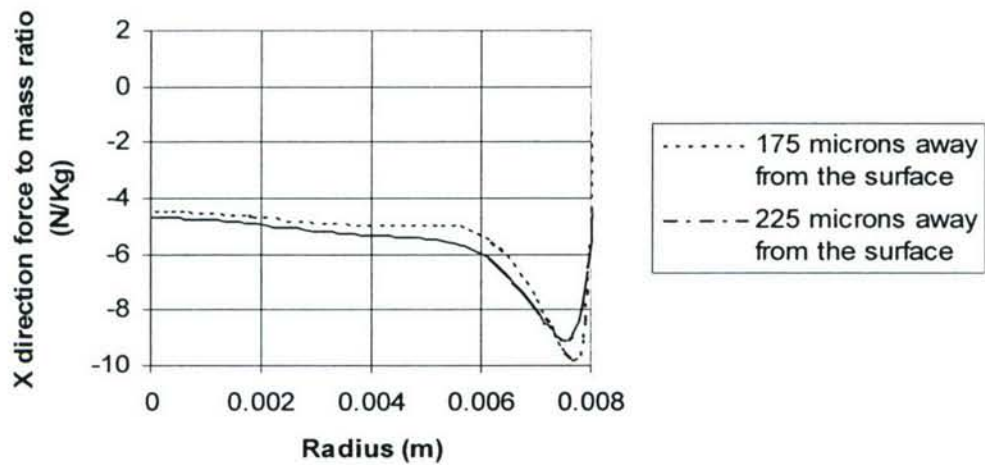


Figure 3.26 X direction (axial) Kelvin force to mass ratio vs. radius.

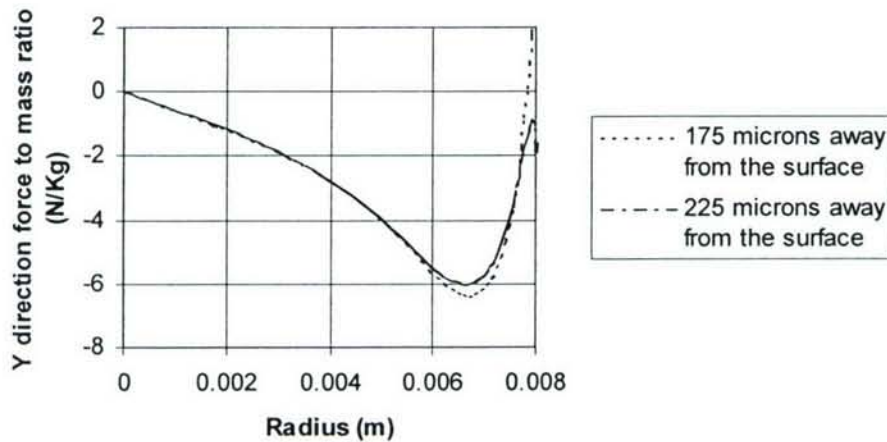


Figure 3.27 Y direction (radial) Kelvin force to mass ratio vs. radius.

### 3.3.2.1 Effect of Kelvin Force on Liquid Jet Hitting a Surface

In order to demonstrate the ability to simulate the electric Kelvin force, simulations were run using the WVU experimental geometry with the second generation electrode system, but with a liquid jet instead of the spray actually used in the physical experiments. As a further simplification, these simulations were isothermal. Table 3.5 shows that cases were run for two jet velocities, with and without uniform gravity and the Kelvin force produced by the second generation electrode system described in the Section 3.3.1. When the

Kelvin force was included (Cases 5 and 6), the Electric module was fully coupled with the Flow and Free Surfaces modules so that the Kelvin force was updated at each time step as the jet changed shape in order to account for the effect of the liquid permittivity on the electric field.

**Table 3.5 Parameters in the jet impingement simulations.**

|                            | Case 1 | Case 2 | Case 3 | Case 4 | Case 5 | Case 6 |
|----------------------------|--------|--------|--------|--------|--------|--------|
| Gravity ( $\text{m/s}^2$ ) | 0      | 9.8    | 0      | 9.8    | 9.8    | 9.8    |
| Voltage (kV)               | 0      | 0      | 0      | 0      | 24     | 24     |
| Velocity (m/s)             | 0.2263 | 0.2263 | 0.5    | 0.5    | 0.2263 | 0.5    |
| We                         | 23.4   | 23.4   | 114.2  | 114.2  | 23.4   | 114.2  |
| Re                         | 2828   | 2828   | 6250   | 6250   | 2828   | 6250   |

The simulations were axisymmetric, but the figures have been mirrored on the axis of symmetry. The computational domain contained 87 zones with a total of 55 711 cells, and the grid was refined near the top surface of the pedestal and at its edge. The properties of the liquid, HFE-7000, are given in Table 2.1. The Reynolds and Weber numbers in Table 3.5 were computed using the initial jet diameter (4 mm) as the length scale. These definitions give values twice as large as Labus's definitions (3.17 and 3.18) which are based on jet radius.

In every case the entire domain was filled with motionless air at  $t = 0$ . The entering jet velocity profile was specified to be flat in all cases. The initial time step was  $10^{-8}$  s, and time step was varied to maintain a value of 0.2 for the CFL (Courant-Friedrichs-Lewy) number. (A CFL value of 0.2 allows the fluid to cross at most 20% of the width of a cell in one time step.) The contact angle at the solid walls was  $0^\circ$ . At the open boundaries the pressure was fixed to be equal to the atmospheric pressure.

#### **3.3.2.1.1 Case 1: Low Velocity with No Gravitational Force and No Kelvin Force**

Figures 3.28 – 3.32 show the evolution of the flow as the jet hits the surface and flows around the edge without separation. In Figure 3.29 ( $t = 0.05622$  s) note that surface tension has caused the tip of the jet to become bulbous. The inset in Figure 3.31 ( $t = 0.1442$  s) shows that the HFE-7000 has already flowed around the edge of the pedestal. The hump in the free surface seen in Figure 3.32 ( $t = 0.1619$  s) suggests that a hydraulic jump is present even though gravity, the key factor required for the traditional hydraulic jump, is not active. Among the cases studied, this is the only one in which the hump was observed. This phenomenon should be studied further to determine the true nature of the hump. The simulation was stopped at  $t = 0.1619$  s without reaching steady state because of the excessive computational time. This simulation proves that the liquid jet under similar conditions will continue to climb “down” the pedestal in zero gravity.

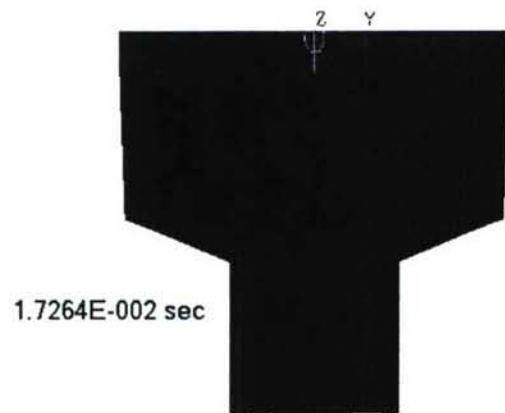


Figure 3.28 Case 1 at  $t = 0.017\,264\text{ s}$ .

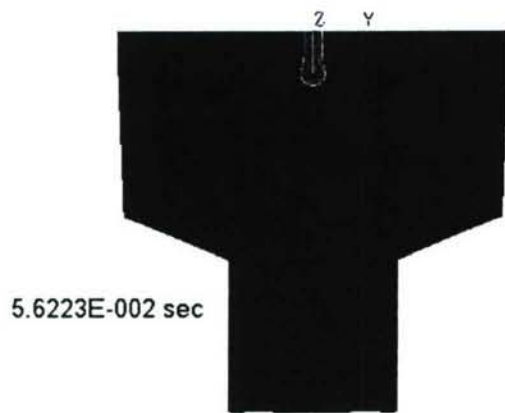


Figure 3.29 Case 1 at  $t = 0.056\,22\text{ s}$ .

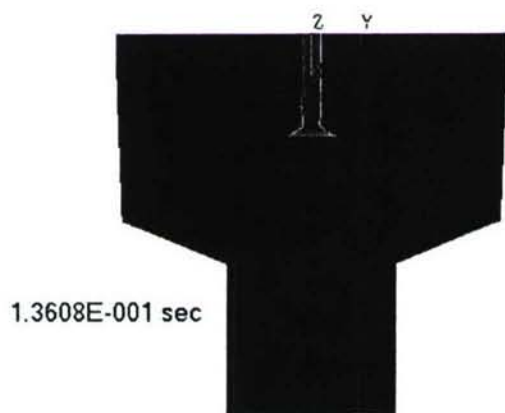


Figure 3.30 Case 1 at  $t = 0.136\,08\text{ s}$ .

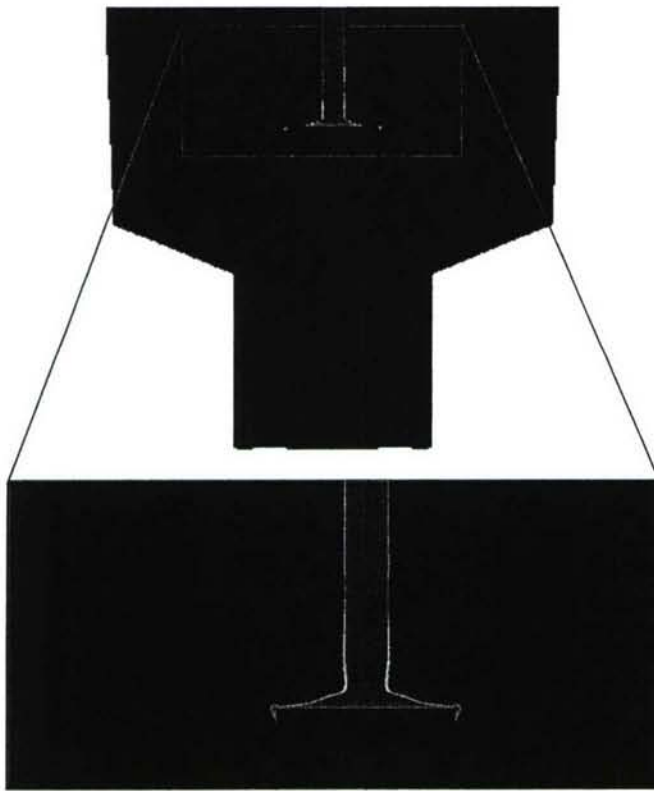
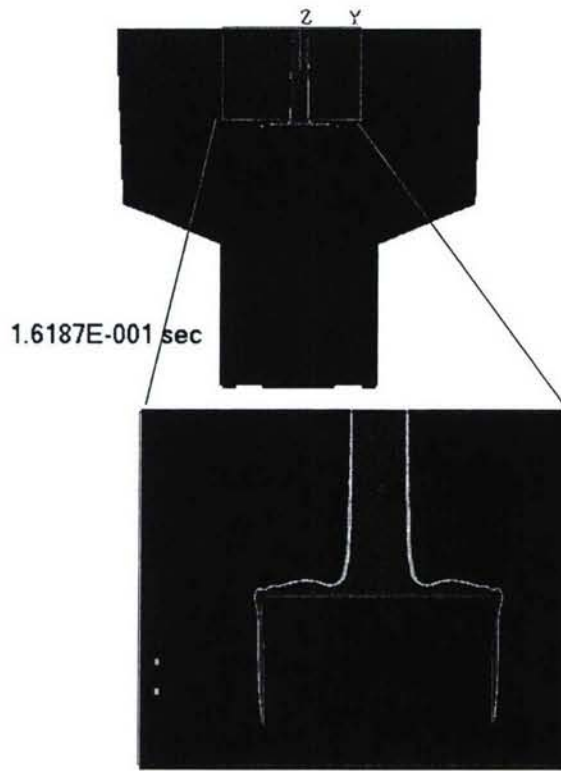


Figure 3.31 Case 1 at  $t = 0.1442$  s.



**Figure 3.32 Case 1 at  $t = 0.161\,987$  s.**

#### **3.3.2.1.2 Case 2: Low Velocity with Gravitational Force and No Kelvin Force**

Case 2 is identical to Case 1 except that normal Earth gravity ( $9.8\text{ m/s}^2$ ) acts in direction of the jet (positive  $x$  direction, shown as down in the figures). Although the low velocity of the jet means that surface tension continues to dominate the flow, gravity accelerates the jet, reducing the dominance of surface tension compared to Case 1. The evolution of the flow is seen in Figures 3.33 – 3.37. Figure 3.34 shows the liquid jet at  $t = 0.0475$  s just before it hits the surface. The influence of gravity is seen in the thinning of the jet, although surface tension still produces a bulbous head. Figure 3.35 ( $t = 0.063$  s) shows that the liquid is spreading radially but has not reached the edge of the pedestal. (The green color outlining the jet in many of these figures represents cells in which the liquid volume fraction is intermediate between 0 and 1, i.e.  $0 < F < 1$ ). In Figure 3.36 ( $t = 0.0718$  s) the jet has flowed around the edge without separation. The liquid has continued to flow down the pedestal in Figure 3.37 ( $t = 0.0795$  s). The gravitationally induced thinning of the jet prior to reaching the surface is easily seen in this figure. Compared to Case 1, the influence of gravity causes the liquid layer to be thinner in Case 2. Furthermore, the hump seen in Case 1 does not appear in Case 2, even though gravity is now acting.

Although not presented here, streamline plots showed that the cases which were run with gravity had a different pattern of air flow compared to those without gravity, apparently because the slight initial hydrostatic pressure variation in the air was neglected. When Case 2 was rerun with the correct initial hydrostatic pressure variation in the air, there was no change in the liquid flow pattern. Therefore the other cases with gravity were not rerun.

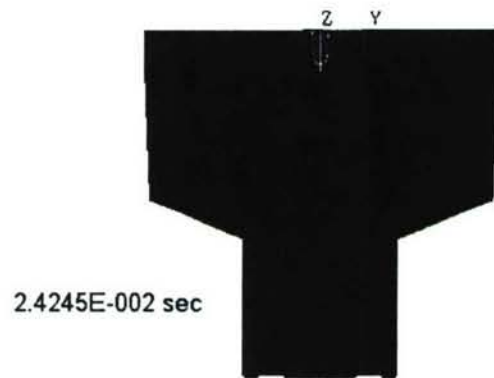


Figure 3.33 Case 2 at  $t = 0.024\ 245$  s.



Figure 3.34 Case 2 at  $t = 0.047\ 497$  s.

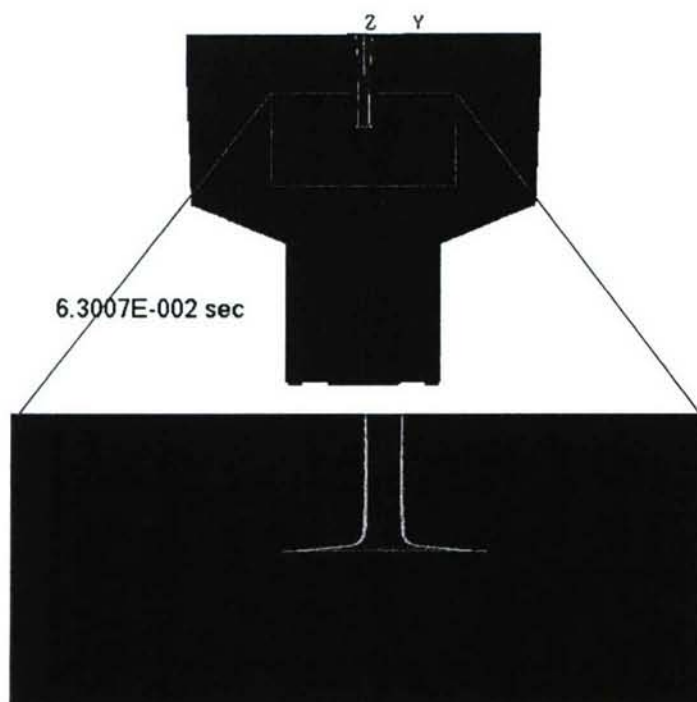


Figure 3.35 Case 2 at  $t = 0.063\ 007\ \text{s}$ .

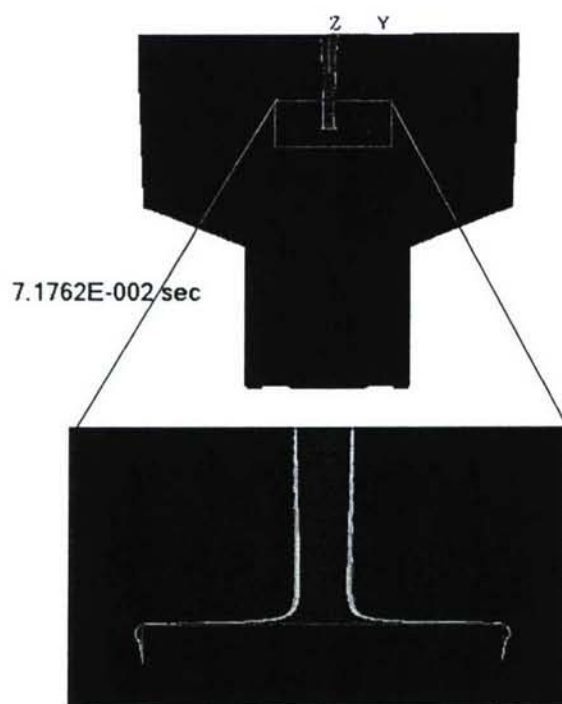
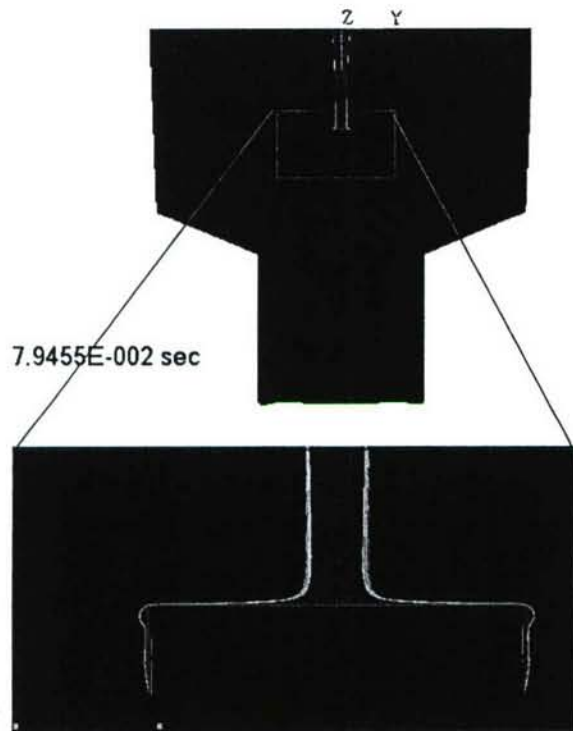


Figure 3.36 Case 2 at  $t = 0.071\ 762\ \text{s}$ .



**Figure 3.37** Case 2 at  $t = 0.079\,455$  s.

### 3.3.2.1.3 Case 3: Higher Velocity with No Gravitational Force and No Kelvin Force

Case 3 is identical to Case 1 except that the velocity of the incoming jet was increased to 0.5 m/s. The Reynolds number for this case is 6250 and the Weber number is 114.2. These values would correspond to Labus's inertial regime, but the geometry is different and the liquid continues to cling to the pedestal. The evolution of the flow is displayed in Figures 3.38 – 3.42. Most of the comments about Case 1 apply to Case 3 as well, except that the hump seen in Case 1 does not appear in Case 3. In Figure 3.41 ( $t = 0.0599$  s) the liquid has reached the edge of the pedestal and has started to move around the edge with no separation. Figure 3.42 shows the HFE-7000 at  $t = 0.0818$  s. The large bulge just below the top of the pedestal is evidence that the liquid possesses substantial radial momentum when it reaches the edge of the pedestal. The simulation was stopped at this time.

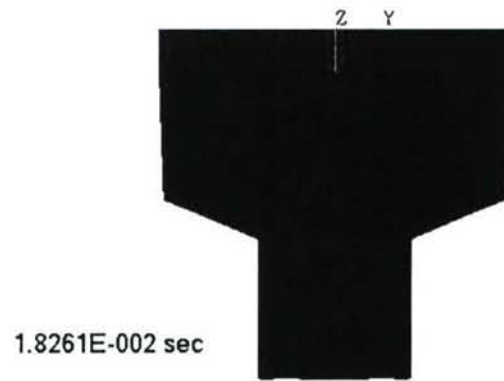


Figure 3.38 Case 3 at  $t = 0.018\,261$  s.

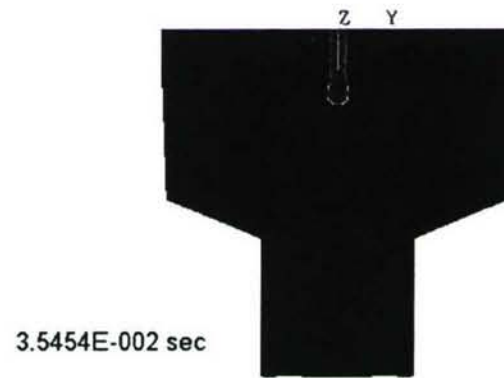


Figure 3.39 Case 3 at  $t = 0.035\,454$  s.

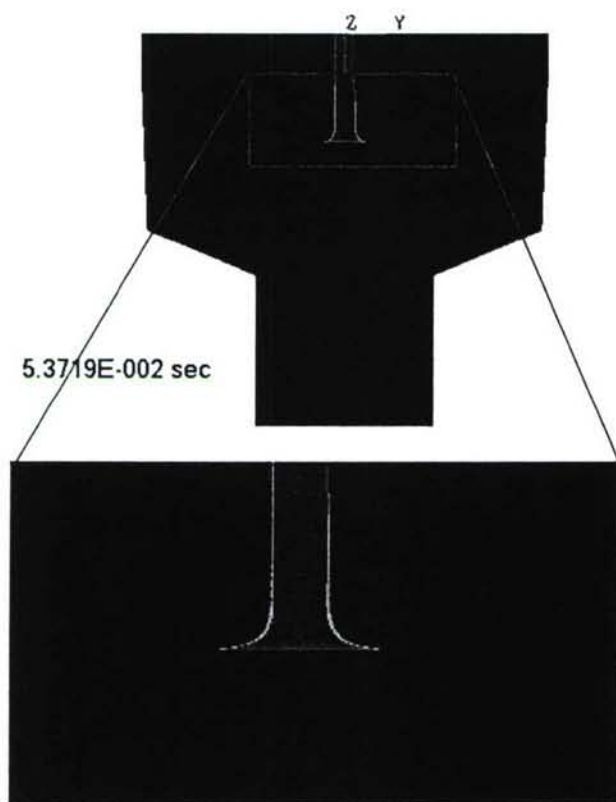


Figure 3.40 Case 3 at  $t = 0.053\,719\text{ s}$ .

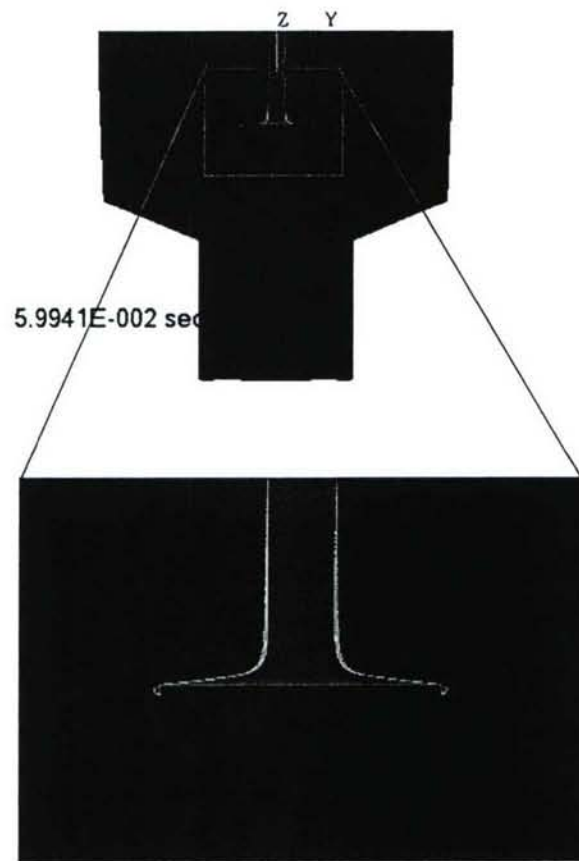


Figure 3.41 Case 3 at  $t = 0.059\,941\text{ s}$ .

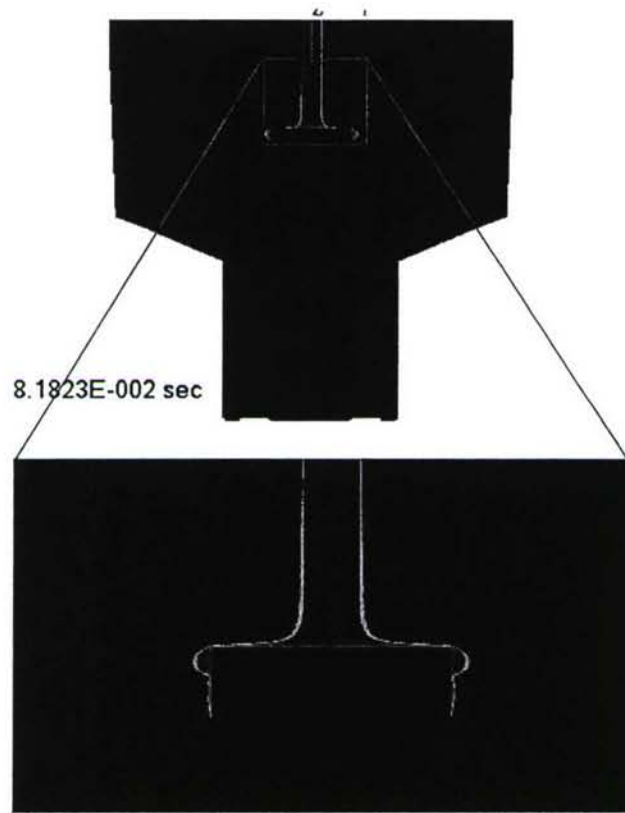


Figure 3.42 Case 3 at  $t = 0.081\,823$  s.

#### 3.3.2.1.4 Case 4: Higher Velocity with Gravitational Force and No Kelvin Force

Case 4 has an initial jet velocity of  $0.5\text{ m/s}$  and a gravitational acceleration of  $9.8\text{ m/s}^2$ . It can be thought of as Case 2 with a higher velocity or as Case 3 with gravity. The Reynolds number is 6250 and the Weber number is 114.2, the same values as Case 3. Figures 3.43 – 3.46 show the developing flow. Figure 3.45 shows that at  $t = 0.0424\text{ s}$ , the liquid has just begun to flow around the edge of the pedestal. In Figure 3.46 ( $t = 0.0479\text{ s}$ ) the flow is proceeding down the side of the pedestal without any separation. The bulge below the edge is less prominent than in Case 3. The simulation was stopped at this point. In Case 4 gravity accelerates the jet causing it to contract, but this effect is much less noticeable than in Case 2. Comparison with Case 3 shows that gravity causes the liquid layer to be slightly thinner. There is no evidence of a hump in the film.



Figure 3.43 Case 4 at  $t = 0.012\ 631\ \text{s}$ .

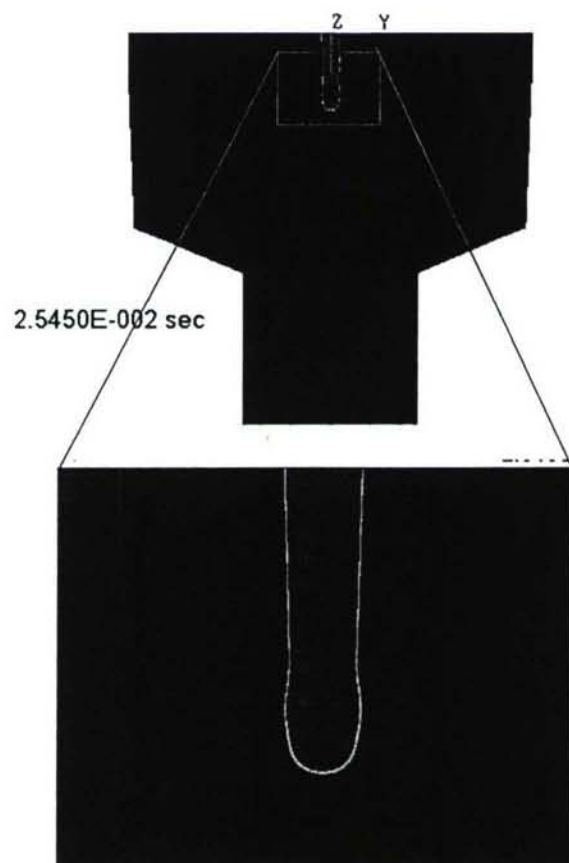


Figure 3.44 Case 4 at  $t = 0.025\ 450\ \text{s}$ .

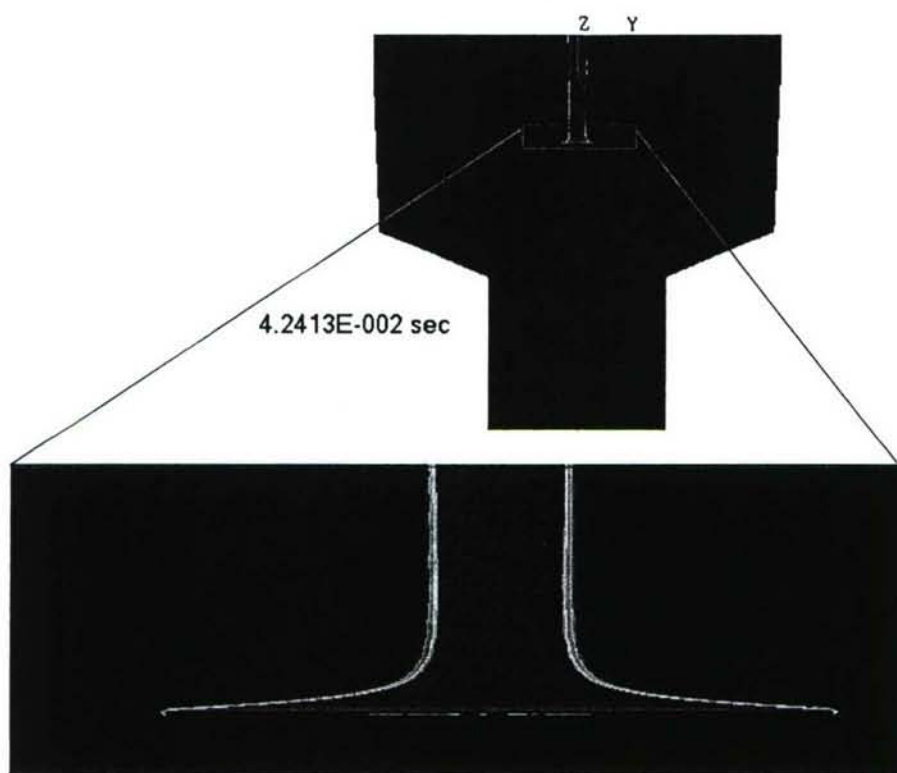
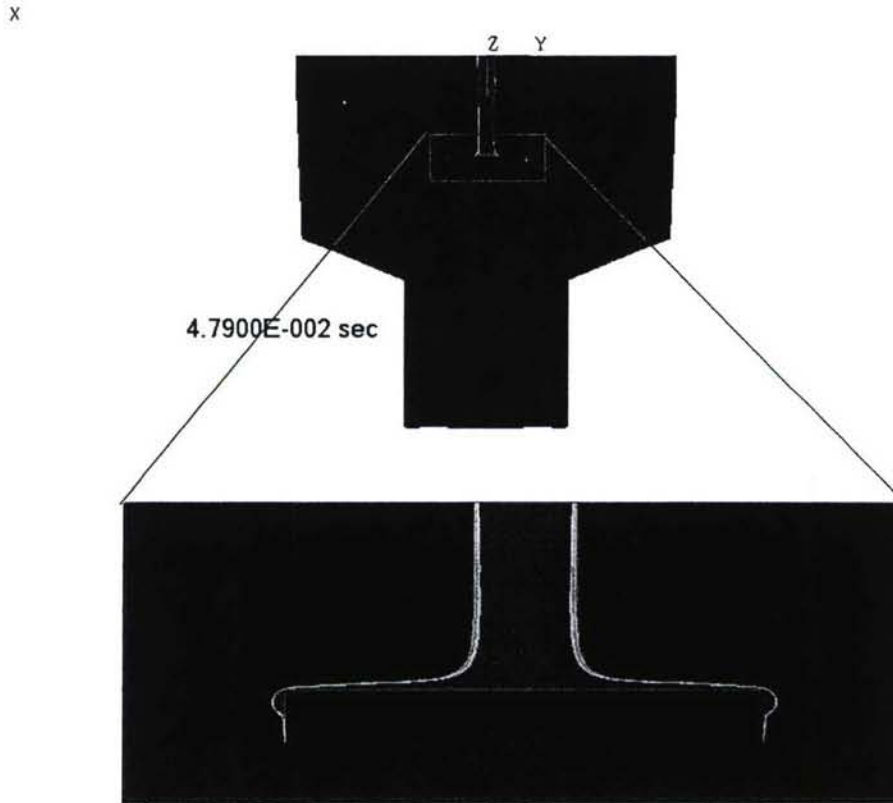


Figure 3.45 Case 4 at  $t = 0.042\,413\text{ s}$ .



**Figure 3.46 Case 4 at  $t = 0.047\ 900\ \text{s}$ .**

#### **3.3.2.1.5 Case 5: Low Velocity with Gravitational Force Opposed by Kelvin Force**

Case 5 differs from Case 2 only by the addition of the electric Kelvin force created by the second generation electrode system described in Section 3.3.1. The nozzle electrode was held at 24 kV and the other two electrodes were at 0 V. The heater was at 12 V, although the simulation was entirely isothermal. As in Case 2 the Reynolds number is 2828 and the Weber number is 23.4. The development of the flow with time is shown in Figures 3.47 – 3.52. In Figure 3.48 ( $t = 0.042\ \text{s}$ ) the leading edge of the jet has been obviously distorted by the Kelvin force which is directed toward the “lamp shade” electrode in that region. The distortion is even more pronounced in Figure 3.49 ( $t = 0.0496\ \text{s}$ ). Figure 3.50 ( $t = 0.0586\ \text{s}$ ) shows the liquid spreading across the surface and reveals surface waves just above the impact region. Because they are not seen in Case 2, these are probably caused by the Kelvin force, although the possibility that they are artifacts due to excessive grid size cannot be excluded. These waves are more prominent in Figure 3.51 ( $t = 0.064\ \text{s}$ ). Figure 3.52 ( $t = 0.0691\ \text{s}$ ) shows that the liquid has turned around the edge of the pedestal without separation and has started to flow down the pedestal.

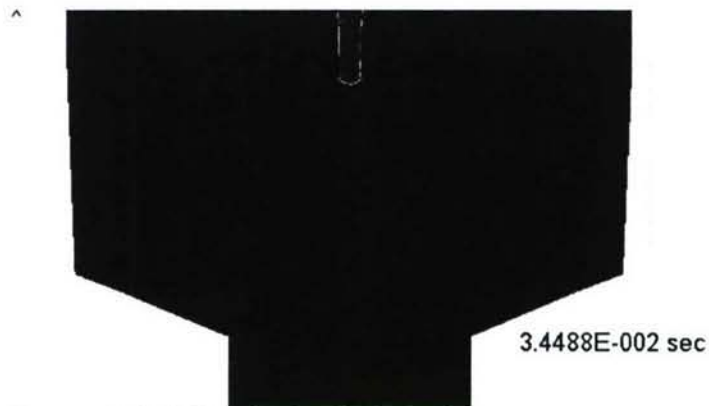


Figure 3.47 Case 5 at  $t = 0.034\ 488$  s.

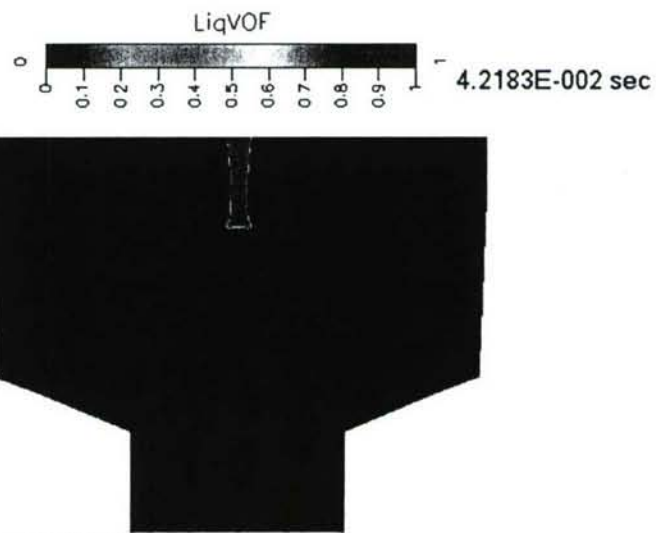


Figure 3.48 Case 5 at  $t = 0.042\ 183$  s.



Figure 3.49 Case 5 at  $t = 0.049\ 668$  s.

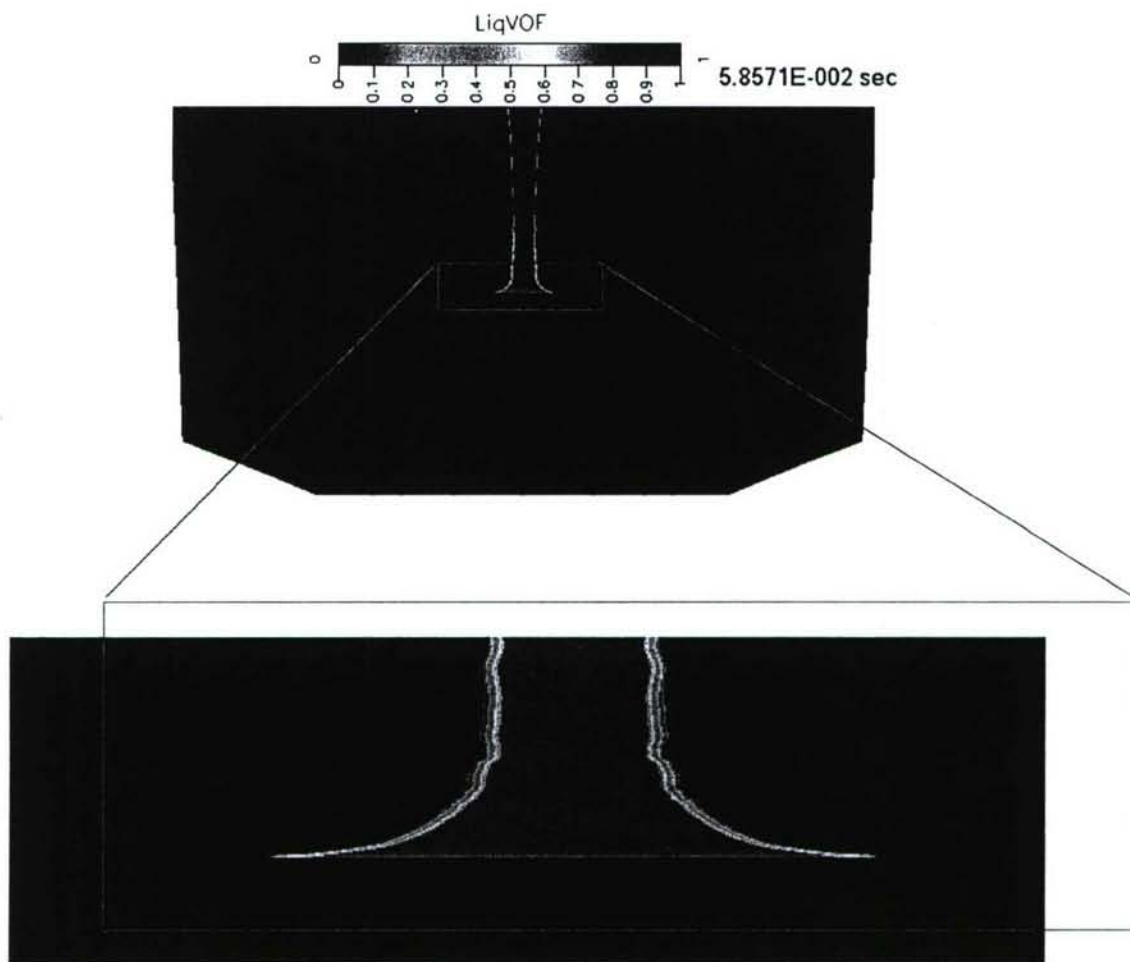


Figure 3.50 Case 5 at  $t = 0.058571$  s.

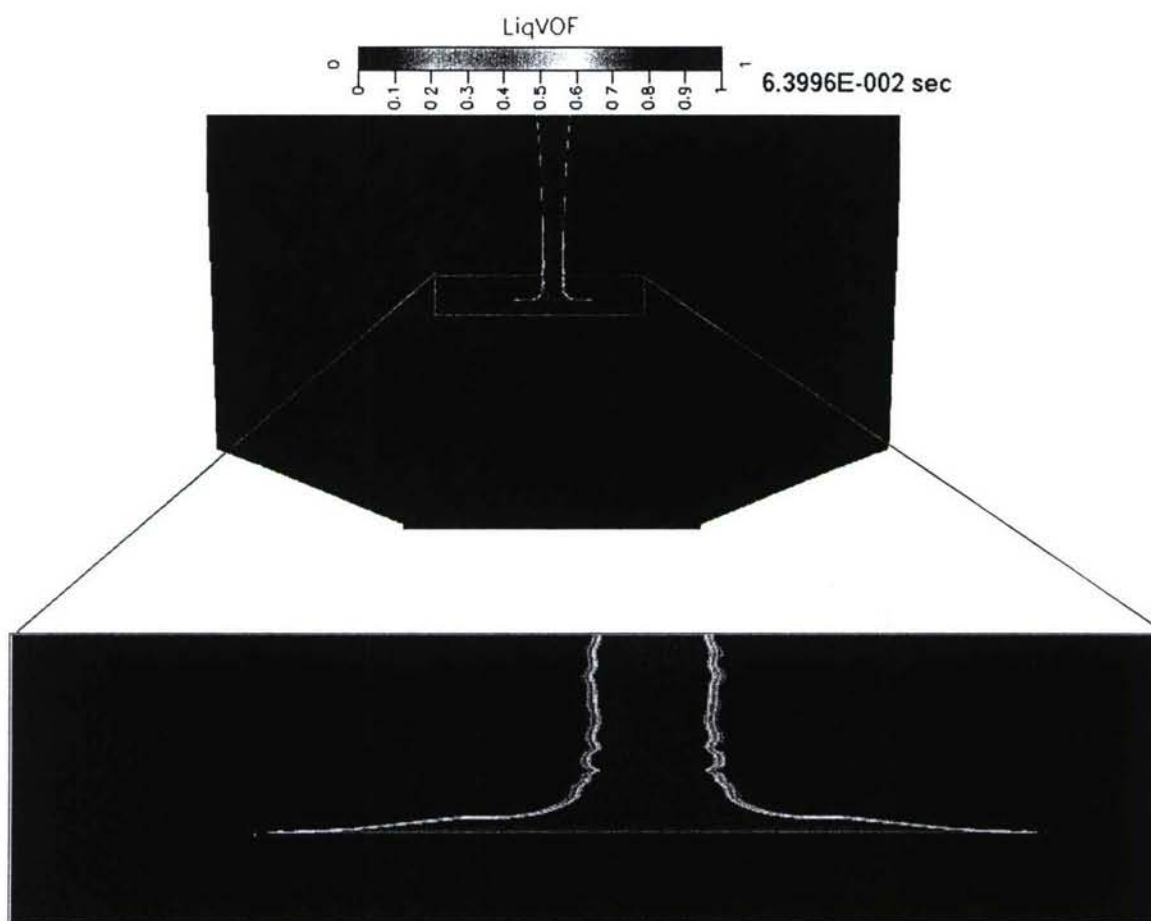
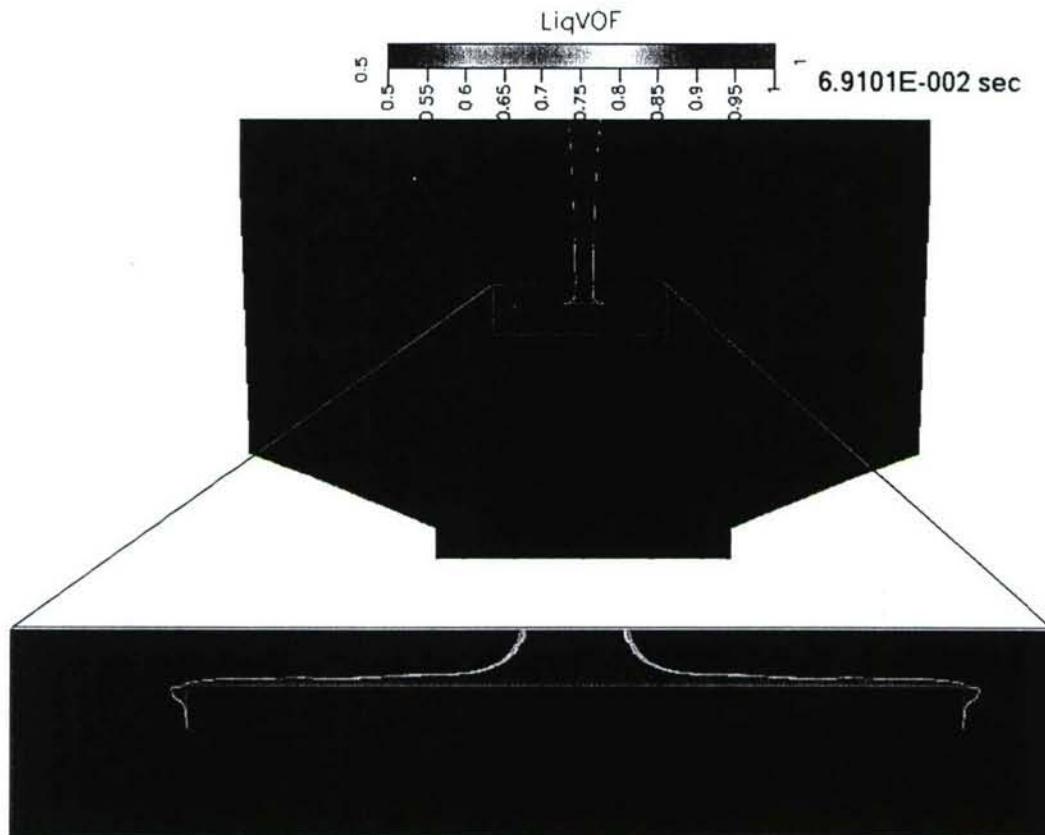


Figure 3.51 Case 5 at  $t = 0.063\,996$  s.



**Figure 3.52** Case 5 at  $t = 0.069\ 101\ \text{s}$ .

#### 3.3.2.1.6 Case 6: Higher Velocity with Gravitational Force Opposed by Kelvin Force

Case 6 differs from Case 4 only by the addition of the electric Kelvin force created by the second generation electrode system described in Section 3.3.1. The nozzle electrode was held at 24 kV and the other two electrodes were at 0 V. The heater was at 12 V, although the simulation was entirely isothermal. As in Case 4 the Reynolds number is 6250 and the Weber number is 114.2. Case 6 is the same as Case 5 except that initial jet velocity is higher. The development of the flow with time is shown in Figures 3.53 – 3.56. Figures 3.53 – 3.55 show the jet before it impinges. Prior to impingement, the tip of the jet is distorted, presumably by the Kelvin force, but the distortion is less than in Case 5. As the liquid spreads across the surface in Figure 3.56 ( $t = 0.041\ \text{s}$ ), disturbances are seen in the jet free surface above the impact zone which do not occur in Case 4, but they are smaller in amplitude than in Case 5. The simulation was terminated at this time even though the liquid had not reached the edge of the pedestal.

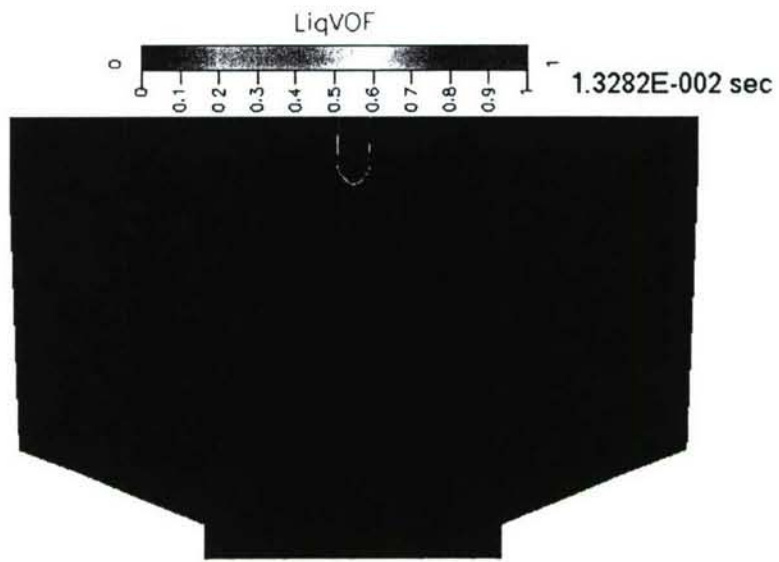


Figure 3.53 Case 6 at  $t = 0.013282$  s.

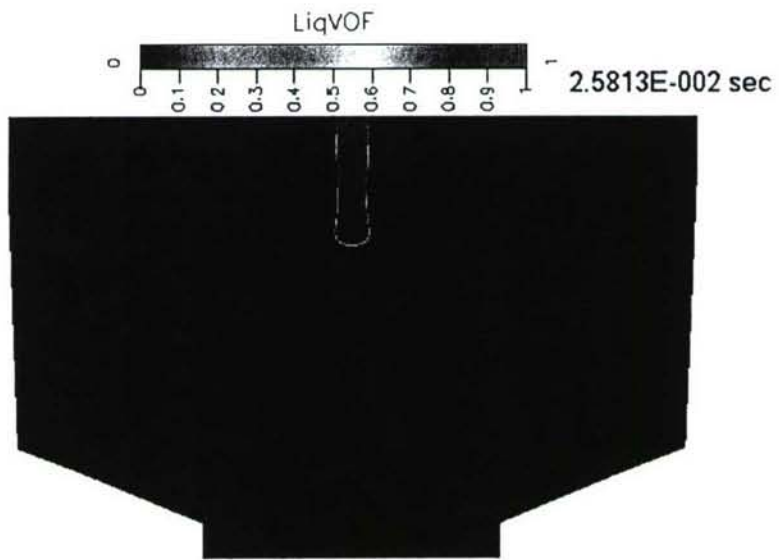


Figure 3.54 Case 6 at  $t = 0.025813$  s.

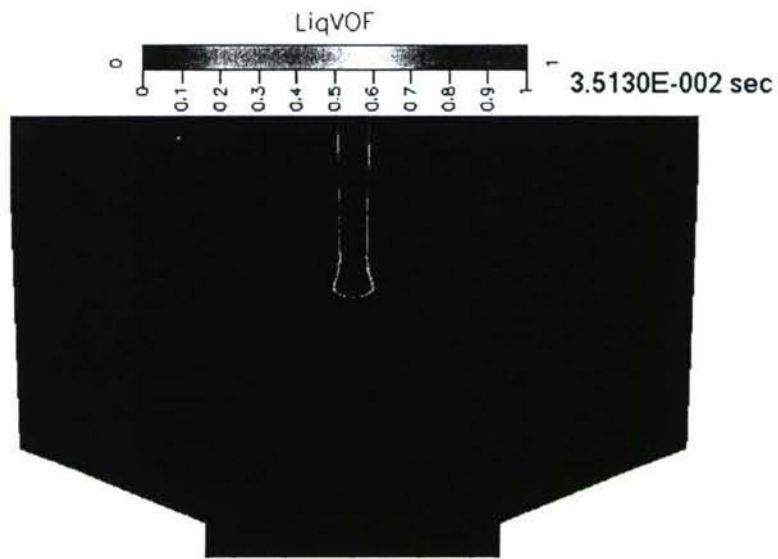


Figure 3.55 Case 6 at  $t = 0.035130$  s.

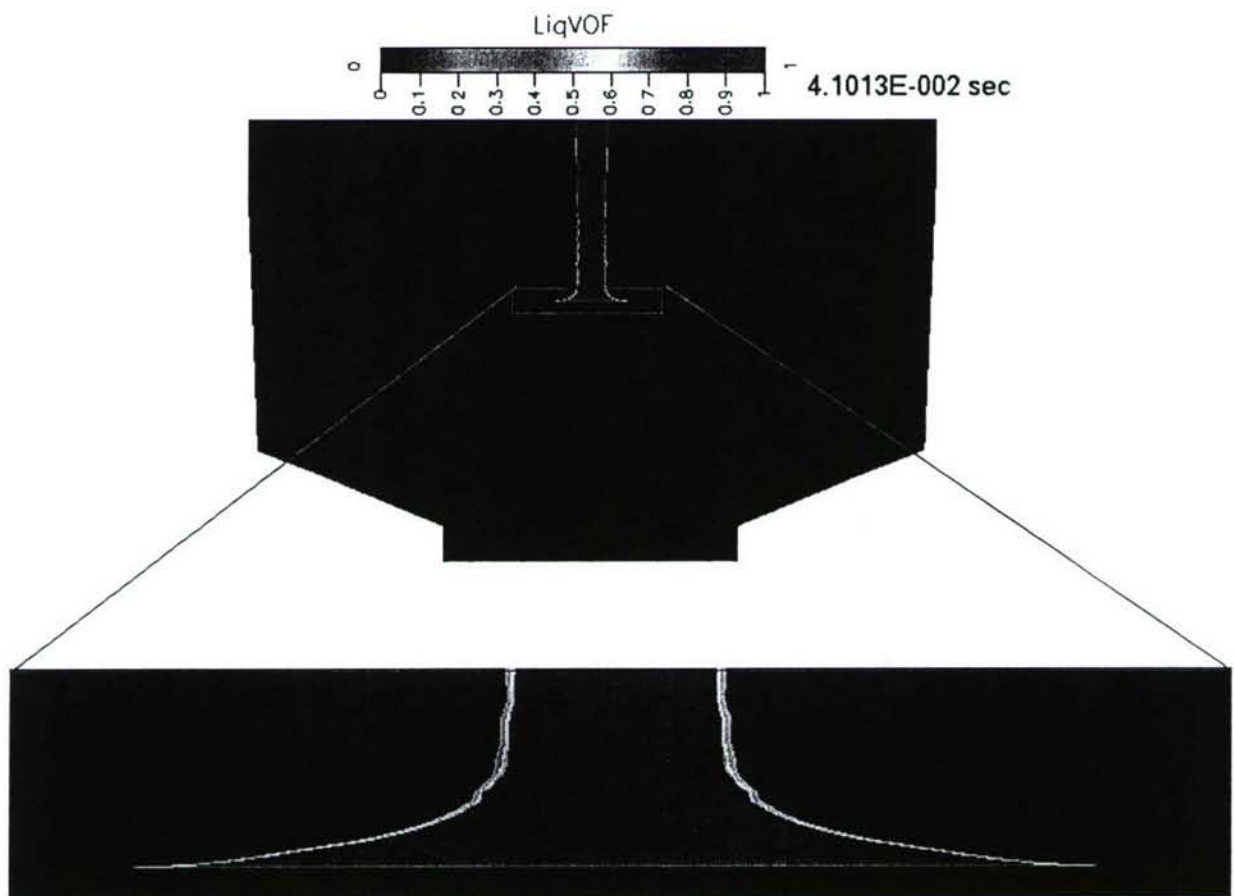


Figure 3.56 Case 6 at  $t = 0.041013$  s.

These simulations demonstrate that the electric Kelvin force has been implemented in CFD-ACE+ by incorporating the appropriate source terms in the momentum equations of the Flow module, and by linking the Electric module with the Flow and Free Surfaces modules. Although the Kelvin force is strongest just above the surface, it affects the flow visibly. With higher voltages or a fluid with a larger permittivity, the effects would be larger.



## CHAPTER 4 EXPERIMENTAL INVESTIGATIONS

This chapter reports the work done in the experimental phase of the project. Section 4.1 gives an introductory overview. Section 4.2 describes the experimental hardware and gives accuracy estimates. Section 4.3 presents the results of experiments without electrical forces. Section 4.3 presents the results of experiments with electrical forces.

### 4.1 Introduction

The primary goal of the present experimental work was to explore the effectiveness of electrical body forces to enhance spray impingement heat transfer in the laboratory. DiMarco and Grassi have demonstrated a significant increase in the CHF in pool boiling of FC-72 via the use of the electric Kelvin force at electric potentials of 10 kV (DiMarco and Grassi, 2002). Snyder et al. (2001) have obtained bubble detachment for pool boiling in microgravity ( $\mu g$ ) using two different electrode geometries at applied voltages of 6-16 kV. Feng and Bryan (2005) investigated the basic physics of EHD liquid jet and spray impingement. Darabi et al. (2000) have studied EHD enhancement of falling-film evaporation on horizontal tubes. Seyed-Yagoobi and Bryan (1999) have surveyed electrohydrodynamic enhancement of heat transfer results. The most dramatic heat transfer increases have generally been observed in condensation heat transfer. In the present work, a spray cooling experiment has been developed that is nearly identical to the AFRL apparatus, but with provision for generating controlled electric fields near the spray nozzle and heater surface. Heat transfer performance data are summarized for two different electrode designs that use the electric Kelvin force, and for two electrodes that have been designed to utilize the Coulomb force.

### 4.2 Experimental Apparatus

The present apparatus uses a spray nozzle, heater, and sump geometry that are nearly identical to the AFRL spray cooling experiment (Baysinger et al., 2004), and either uses the same working fluid of FC-72, or a second dielectric working fluid, HFE-7000. Theses by Hunnell (2005), Glaspell (2006), and Kreitzer (2006) have given detailed descriptions of the development of the current apparatus. A schematic of the spray nozzle, heater surface, pedestal, and sump is shown in Figure 4.1. The nozzle and heater surface have been housed in a spray chamber that has been fitted with optically transparent view ports for flow visualization. The geometry of this portion of the present apparatus is identical to the AFRL apparatus, except for electrical penetrations in the WVU spray chamber for the present study of the effects of electrical body forces on spray cooling performance.

Spraying Systems full cone 1/8G nozzles have been used in the present work; identical nozzles are being used by the AFRL team. Yerkes et al. (2006) have measured the spray droplet Sauter mean diameter and velocity for this nozzle type to be  $48 \mu m$  and  $12 m/s$ , respectively, at a flow rate of  $9.5 \times 10^{-6} m^3/s$ . Nozzle-heater spacing for the majority of the present results is  $13 mm$ , and heater diameter is  $16 mm$ . This spacing was chosen so that the outer edge of the spray cone coincides with the circumference of the heater. Two different types of heaters have been used in the present work: an optically transparent Indium-Tin-Oxide (ITO) heater, and a more robust

ceramic Thick-Film Resistor (TFR); these same heater types are being used in the AFRL work. The heaters are bonded to the top of either an optically transparent cylindrical glass pedestal or a PTFE pedestal (Figure 4.1); the pedestal is installed in an annular sump that is used to collect the excess liquid working fluid for recirculation. The sump can be fitted with a concentric hollow conical “cap” that is used to redirect the excess liquid into the sump and to aid in liquid flow management; see Figure 4.1. The cap also serves to simulate the effects of impingement of a regular array of neighboring sprays onto a large heater. Results have also been obtained without a cap fitted to the sump. The transparent pedestal allows viewing of the flow on the surface of the ITO heater from below, but the TFR is opaque.

The spray chamber housing the nozzle and sump has been fabricated from a flanged short pipe nipple (15 cm ID by 15 cm long) fitted with two smaller-diameter flanged side ports: one for the spray nozzle supply piping, and a second for the heater/pedestal/sump assembly. The spray chamber is sealed by 2.5 cm thick polycarbonate transparent blanks bolted to the flanges; these ports are used for visualization of the spray. This spray chamber has been pressure tested to 1.4 MPa. It is this portion of the apparatus that is essentially identical to the AFRL design. Figure 4.2 shows the spray chamber mounted to an experiment base that houses the necessary pumps, valves, flowmeters, pressure and temperature instrumentation, and heat exchangers needed to allow continuous operation.

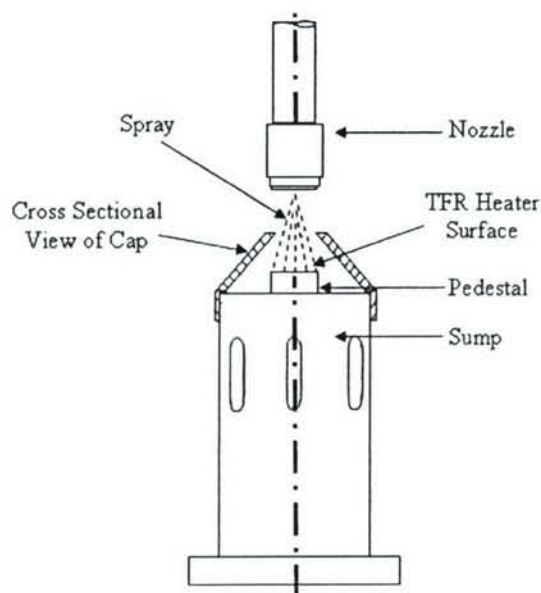


**Figure 4.1** Schematic of the nozzle, pedestal, heater spray, sump and cap.

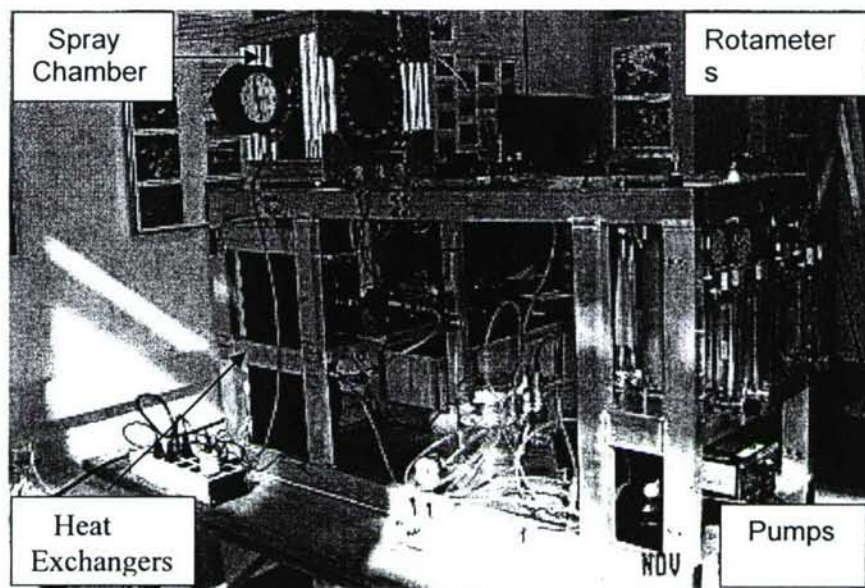


**Figure 4.2 Overview of experimental apparatus for initial baseline data (Hunnell, 2005).**

A schematic of the flow loops housed in the experiment base is shown in Figure 4.3. A positive-displacement gear pump pumps the working fluid from a reservoir to the spray nozzle. Setting the pump speed controls the flow rate, and a rotameter monitors the flow rate. The spray impinges on the heater surface, and the excess liquid is collected in the sump. The vapor is condensed on the chamber walls and is collected in the sump. A positive-displacement diaphragm pump sends the working fluid through a liquid-air heat exchanger back into the reservoir. Spray chamber temperature is controlled by water flowing through tubes cemented to its outside cylindrical surface. This flow is created by a separate flow loop, consisting of a water reservoir, liquid-air heat exchanger, centrifugal pump, and rotameter. Both flow loops contain filters, as well as pressure and temperature instrumentation. A close-up photo of the heater, pedestal, and sump installed in the spray chamber, without a cap installed, is shown in Figure 4.4.

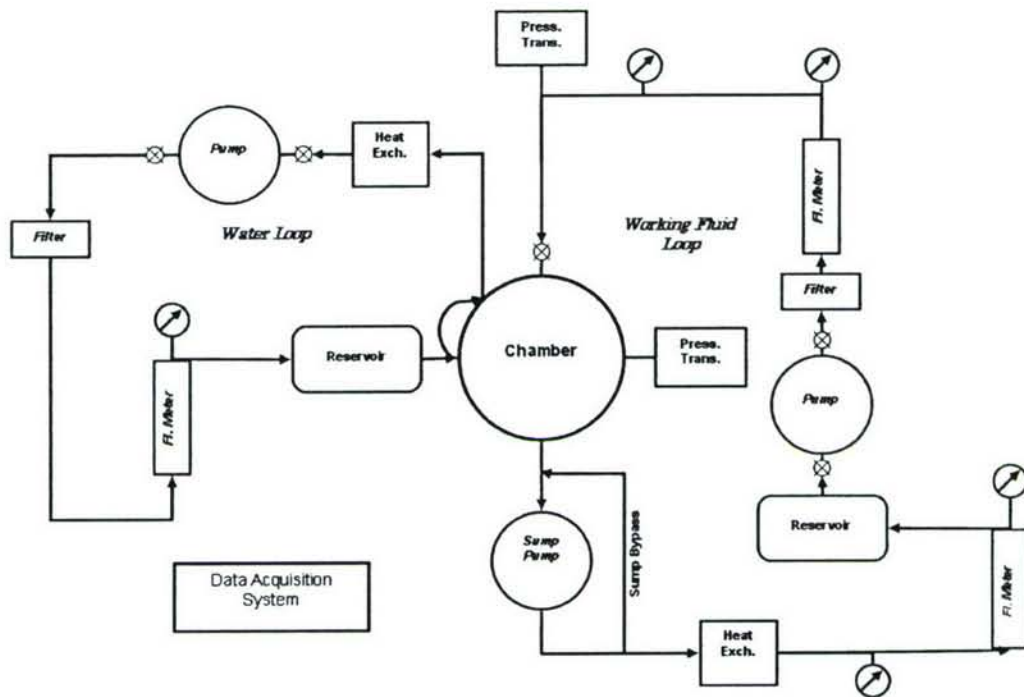


Figure 4.3 Schematic of experimental flow loop, showing test fluid flow loop and cooling water flow loop.

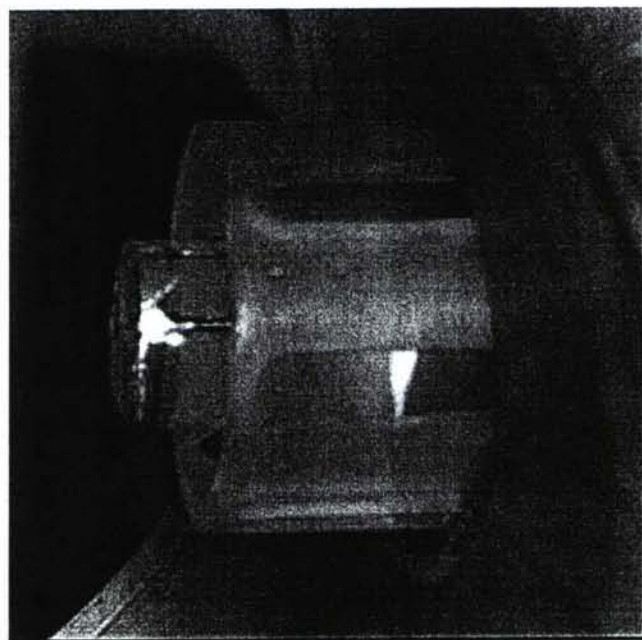
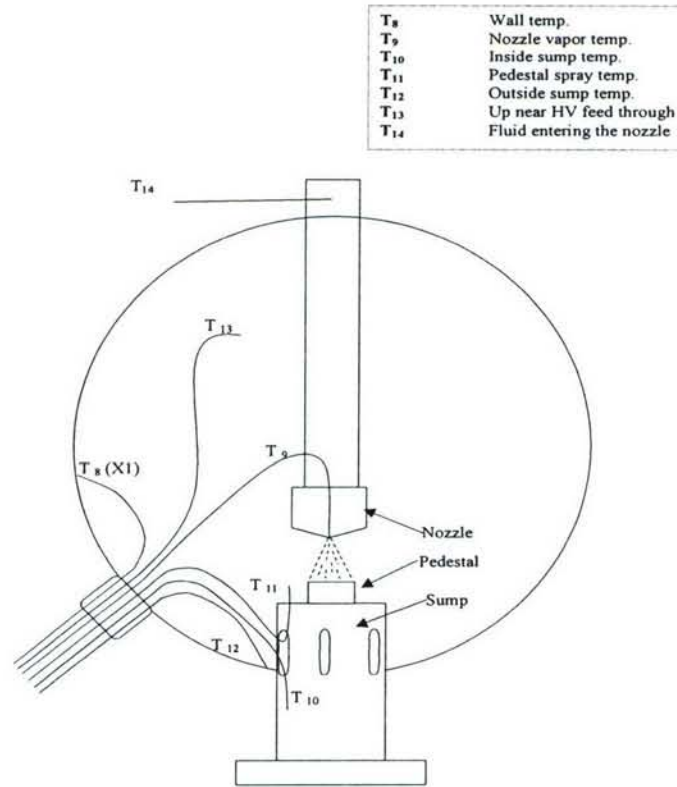


Figure 4.4 Sump and pedestal, without a cap, inserted into the spray chamber.

The glass pedestal onto which the heater has been mounted has seven 0.25 mm (0.01”) type E thermocouples installed in the same locations as those used for the AFRL apparatus (Baysinger et al., 2004). The thermocouple labeled as “T<sub>1</sub>” is installed immediately beneath the heater, approximately 0.5 mm from the heater surface that is contacted by the spray. The analysis developed by Yerkes et al. (2006) has been used to compute the heater surface temperature from the measured temperature 0.5 mm below the heater surface in contact with the working fluid. Other thermocouples have been mounted inside the spray chamber, as indicated in Figure 4.5. The thermocouples have been calibrated against precision mercury-in-glass thermometers and/or an RTD standard thermometer with 0.1 °C resolution in a stirred liquid bath.



**Figure 4.5 Thermocouple locations in the spray chamber.**

Dimensional performance results have been analyzed in the non-dimensional form developed by Yerkes et al. (2006), in which the heat flux has been non-dimensionalized as the parameter,  $G\Delta$ , defined as:

$$G\Delta = \dot{Q} / [\pi b (T_{sat} - T_{\infty wall}) k_{hr}] \quad (4.1)$$

where  $\dot{Q}$  is the power supplied to the heater

$b$  is the radius of the heater

$T_{sat}$  is the saturation temperature

$T_{\infty wall}$  is the average temperature of the spray liquid as it travels through the sump

$k_{hr}$  is the thermal conductivity of the heater material.

The initial baseline data without electric field effects by Hunnell (2005) has been non-dimensionalized using a slightly different non-dimensional heat flux, called  $(G\Delta)_{init}$  herein; this was the initial definition used by Yerkes et al. (2005). In this definition, the temperature difference in Equation (4.1) was replaced by  $T_{\infty wall}$ .

The temperature difference,  $(T_s - T_{\infty top})$ , has been non-dimensionalized for all results by dividing by  $(T_{sat} - T_{\infty wall})$ . The reference temperature  $T_{\infty top}$  is the average temperature of the liquid film on the heater surface, taken as the average of the initial liquid spray temperature and the temperature of the spray as it leaves the heater surface.  $T_s$  is the heater surface temperature, computed from the measured interface temperature at the bottom of the heater substrate. The heat transfer model developed by Yerkes et al. (2006) for the ITO heater has been extended in an approximate way to include the effect of the insulating glass layer on the top side of the TFR ceramic heater in the calculation of the heater surface temperature,  $T_s$  (Hunnell et al., 2006). A simple one-dimensional conduction heat transfer thermal resistance across the insulating glass layer on the side of the TRF heater in contact with the working fluid has been used to estimate a temperature drop across this glass layer in order to get an estimate of  $T_s$ . This results in a reduction of the heater surface temperature of approximately 5°C at a heater power of 60 W. The computed heat transfer coefficients have been non-dimensionalized as the Nusselt number, Nu, defined as:

$$Nu = \frac{hb}{k_{fluid}} \quad (4.2)$$

where  $h$  is the heat transfer coefficient  
 $k_{fluid}$  is the liquid thermal conductivity.

#### 4.2.1 Statement of Experimental Accuracy

Estimates of measurement uncertainty for the present system have been made by Hunnell (2005), Glaspell, (2006), and Kreitzer (2006). Flow meter repeatability is estimated as  $\pm 3\%$  to  $5\%$ , based on the manufacturer's specifications. Heater power accuracy has been estimated as  $\pm 0.2$  to  $0.8$  W, and estimated temperature resolution is  $\pm 0.1$  °C. Temperature measurement accuracy is estimated as  $\pm 0.2$  °C for all calibrated thermocouples, and as  $\pm 0.6$  °C for uncalibrated thermocouples (Glaspell, 2006). Propagation of these measurement errors yielded the following estimates of uncertainty for the calculated results:  $\pm 3\text{-}5\%$  for high heat flux results,  $\pm 3\text{-}5\%$  for the larger temperature differences, and  $\pm 5\text{-}7\%$  for higher values of heat transfer coefficient. Larger percent uncertainties are estimated at lower heat fluxes. It is believed that repeated data runs made without any changes to the experimental setup should repeat to within these estimated error bounds that are based on instrumentation error estimates. Significantly larger run-to-run variations in the experimental results are observed whenever the experimental setup has been modified or reassembled, as will be discussed below.

### 4.3 Experiments Without Electrical Forces

Baseline spray cooling performance results for the present apparatus without electrical body force effects have been presented by Hunnell (2005) and by Hunnell et al. (2006) under conditions of terrestrial gravity for both vertically-downward and horizontal sprays. These results were obtained for spray flow rates between  $4.8 \times 10^{-6} \text{ m}^3/\text{s}$  and  $9.8 \times 10^{-6} \text{ m}^3/\text{s}$  (4.6 GPH to 9.3 GPH), and heater power levels from 10 W to 70 W at a nozzle-to-heater spacing of 13 mm, for three different sump geometries: an unconfined flow (no cap installed on sump), and two confined flows (straight-walled cap, identical to the AFRL geometry, and curved-wall cap). Heat flux has been computed as the ratio of the heater power divided by the heater surface area. No correction has been made for heat lost down the pedestal; Baysinger (2004) showed that this effect was only about 1.5% of the heater power. The heater surface temperature,  $T_s$ , was computed from the measured temperature 0.5 mm beneath the upper heater surface, as described above. For all geometries, at a constant heater power as the spray flow rate was increased cooling of the heater surface and heat transfer coefficient were increased, as expected (Hunnell, 2005). At the higher spray flow rates, the unconfined flow geometry had the most efficient heat transfer (cooler at equal heat fluxes) and the highest heat transfer coefficient, but for the vertically-downward flow this trend was reversed at the lowest flow rates.

The spray droplet Reynolds, Weber, and capillary numbers have been computed (Hunnell, 2005) based on FC-72 liquid properties and the droplet diameter and velocity measurements obtained by Baysinger et al. (2004) for an identical spray nozzle. Weber and Reynolds numbers were 1140 and 1650 respectively. The relatively large values of the Weber and Reynolds numbers indicate that droplet momentum dominates over both surface tension and viscous forces. The capillary number  $[(\mu V)/\sigma]$  was 0.7. A capillary number of 1 indicates that surface tension forces are comparable to viscous forces.

As examples of the non-electric field baseline results presented by Hunnell (2005), Figures 4.6 and 4.7 compare the dimensional heat transfer performance for vertical downward and horizontal sprays at similar saturation temperatures and subcooling levels, at flow rates of 9.3 and 6.2 GPH. Heat flux has been computed as the ratio of the heater power divided by the heater surface area. No correction has been made for heat lost down the pedestal; Baysinger (2004) showed that this effect was only from 1 to 3% of the heater power. Unconfined flow results are shown in Figure 4.6, while results for the straight-walled cap are shown in Figure 4.7. Uncertainty estimates for the heat flux and temperature difference are shown. For the unconfined spray, the vertical spray is slightly more efficient than the horizontal spray at a flow rate of 6.2 GPH. This is opposite to trends observed by Kato, et al. (1994) and Yoshida, et al. (2001). At 9.3 GPH, the opposite trend is observed for the unconfined flow. No significant difference between the vertical and horizontal spray is observed for the straight cap geometry (Figure 4.7).

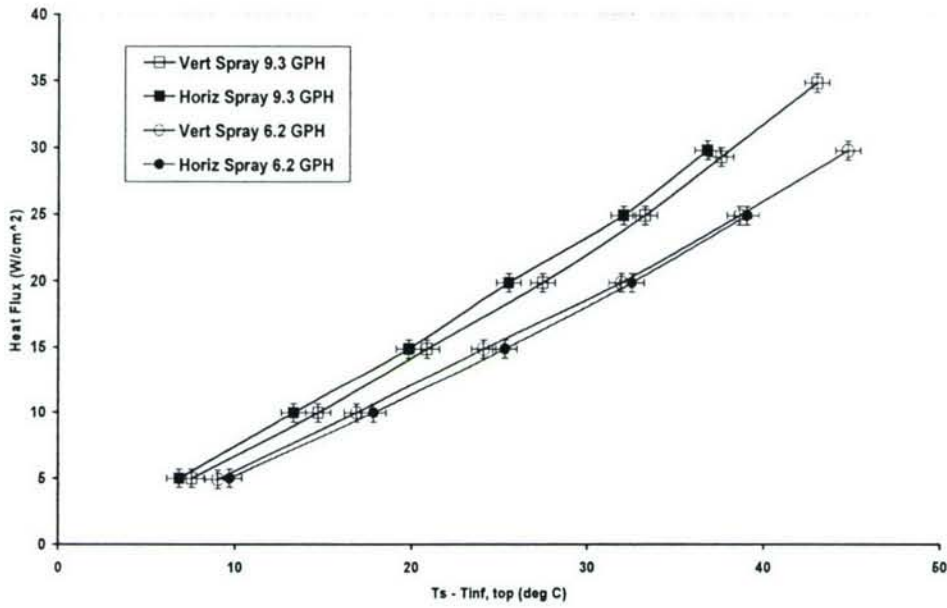


Figure 4.6 Comparison of vertical and horizontal spray heat flux as a function of surface temperature for the unconfined geometry at two different flow rates.

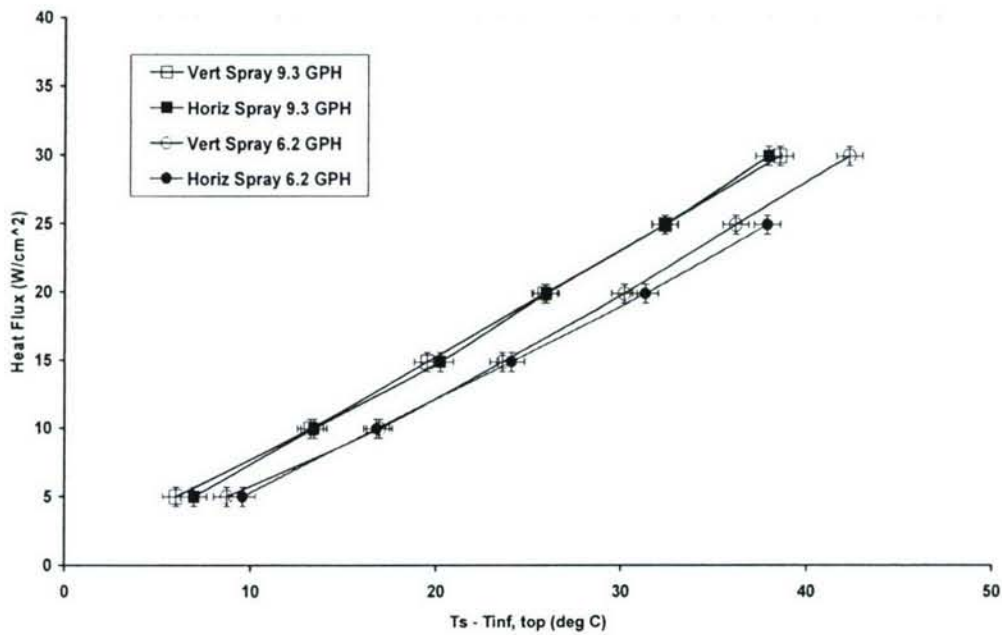
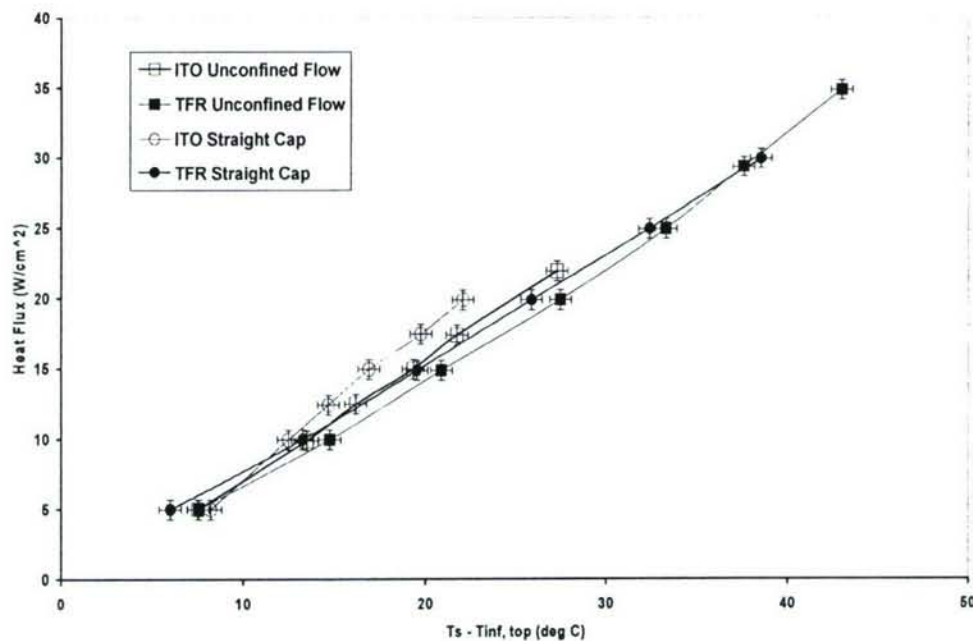


Figure 4.7 Comparison of vertical and horizontal spray heat flux as a function of surface temperature for the straight cap geometry at two different flow rates.

A comparison of the heat transfer performance of the two different heater types (TFR and ITO) is shown in Figure 4.8 for a spray flow rate of 9.3 GPH. The ITO heater is consistently somewhat more efficient (cooler at equal heat fluxes); this is believed to be due to the differences in heater geometry. The ITO heater is formed by deposition of a thin ITO resistive film on the glass surface, and is thus in direct contact with the impinging FC-72 spray. The TFR heater, on the other hand, is a commercial resistor that has the resistive film sandwiched between a bottom substrate and a thin glass top layer that is in contact with the FC-72. It is believed that this glass coating causes the TRF heater to run hotter than the ITO heater, as measured by  $T_1$  located on the back side of the heater.

The computed heat transfer coefficients for the TFR heater with the straight-cap geometry are shown in Figure 4.9. For both heater orientations, Figure 4.9 shows that the heat transfer coefficient increases with spray flow rate, and is largely independent (increasing only slightly) of heater power. The heat transfer coefficient is nearly identical for horizontal and vertical sprays.



**Figure 4.8 Comparison of vertical spray heat flux as a function of surface temperature for both the ITO and TFR pedestals at a flow rate of 9.3 GPH.**

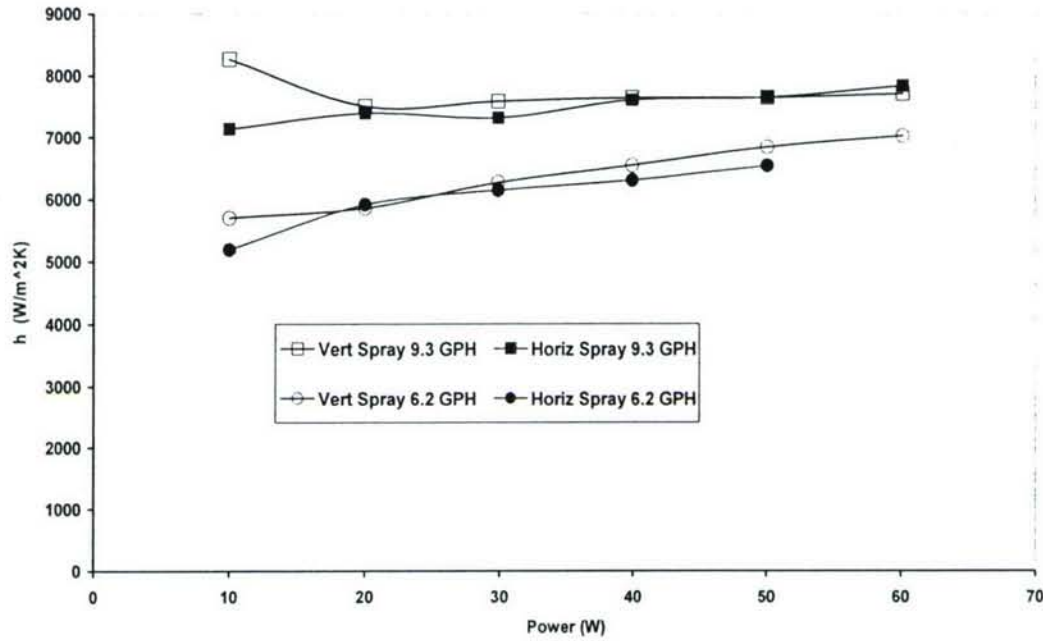


**Figure 4.9 Heat transfer coefficient as a function of power for both the vertical downward spray and horizontal spray with a straight cap.**

The same results that have been presented in dimensional form in Figures 4.6 - 4.9 are presented in the initial non-dimensional form developed by Yerkes, et al. (2005) in Figures 4.10 – 4.13. The heat flux has been non-dimensionalized as the parameter,  $(G\Delta)_{init}$ , defined as:

$$(G\Delta)_{init} = \dot{Q} / (\pi b T_{\infty, wall} k_{htr}). \quad (4.3)$$

Trends in the non-dimensional presentation of the current results are generally identical to those discussed above for the dimensional results. Not much difference is observed between the vertical and horizontal sprays at the same FC-72 flow rate and heater power (Figures 4.10 and 11). This is especially true for the straight cap geometry. The unconfined spray shows some improvement for the horizontal spray at the highest flow rate of 9.3 GPH (Figure 4.10).

The greater heat transfer efficiency of the ITO heater compared to the TFR heater remains in the non-dimensional presentation (Figure 4.12). Nusselt number (Figure 4.13) increases versus FC-72 flow rate, but there is not much difference between results for the vertical and horizontal sprays. Nusselt number increases only slightly versus  $(G\Delta)_{init}$  or heater power.

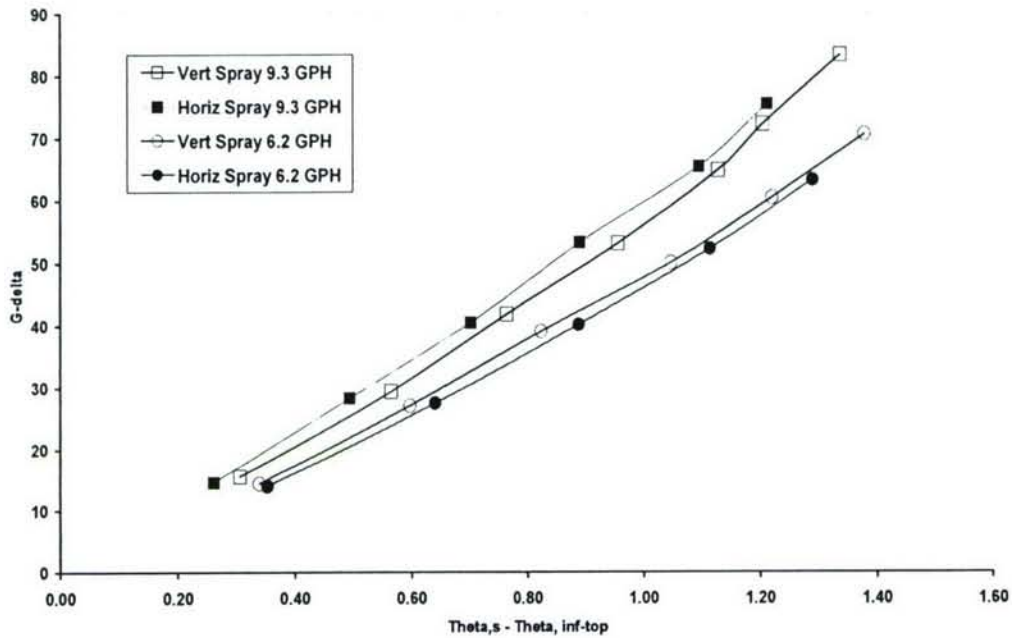


**Figure 4.10** Comparison of vertical and horizontal spray non-dimensional heat flux as a function of non-dimensional surface temperature difference for the unconfined geometry at two different flow rates.

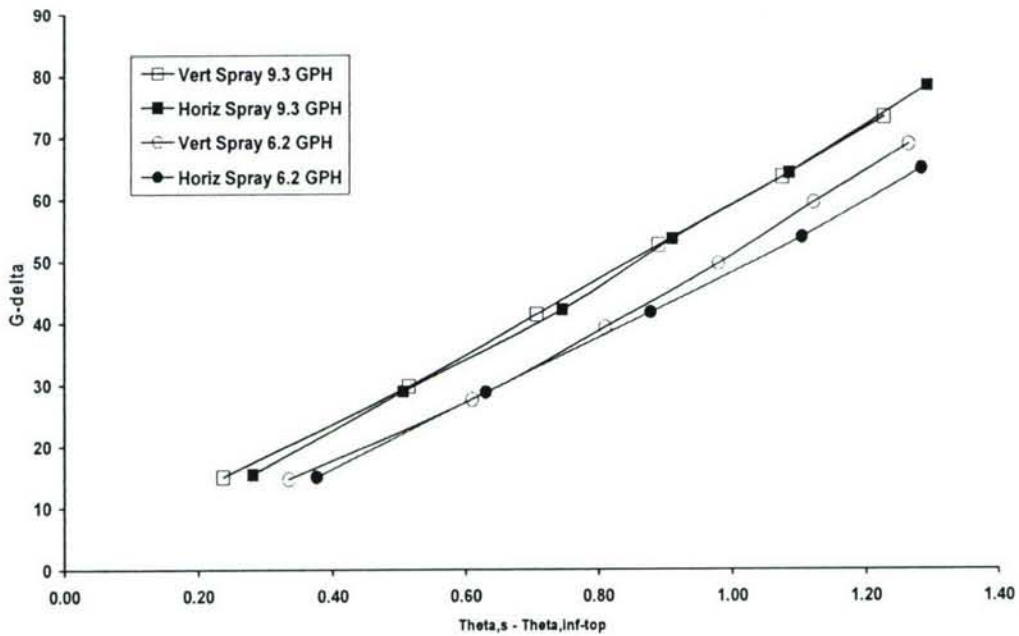


**Figure 4.11** Comparison of vertical and horizontal spray non-dimensional heat flux as a function of non-dimensional surface temperature difference for the straight cap geometry at two different flow rates.

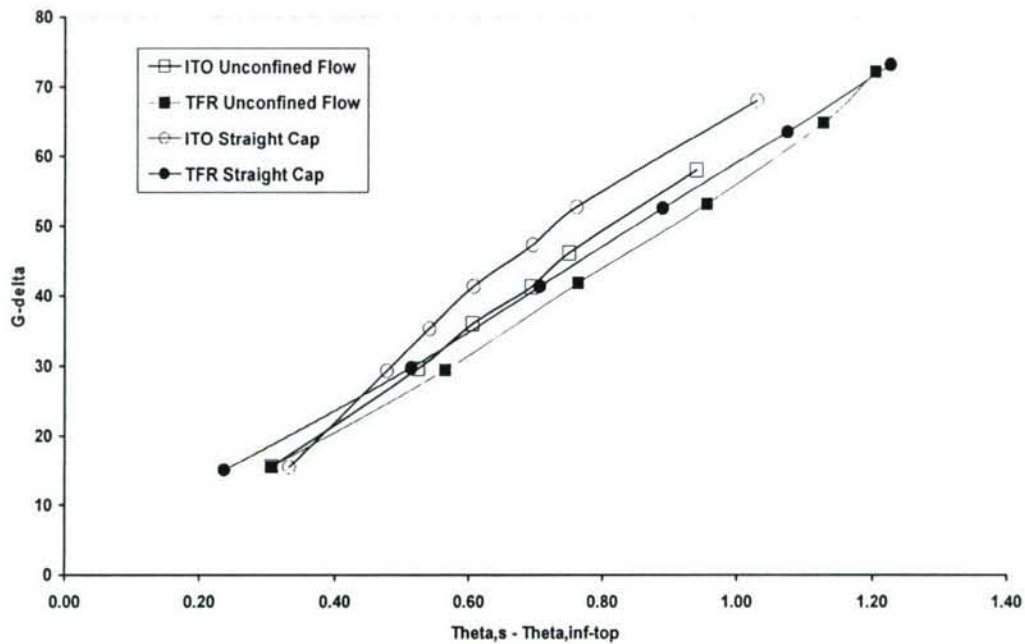


Figure 4.12 Comparison of vertical spray non-dimensional heat flux as a function of non-dimensional surface temperature difference for ITO and TFR heaters at a flow rate of 9.3 GPH.

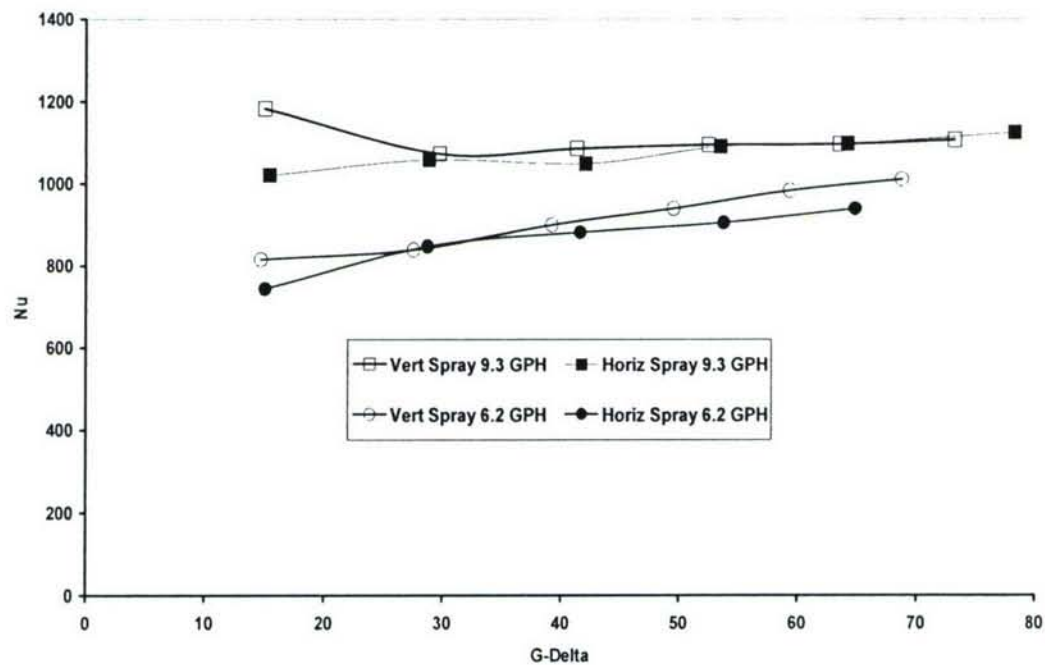
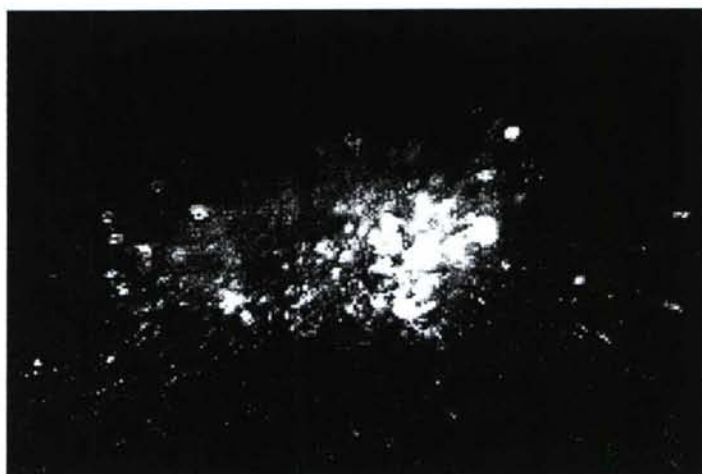
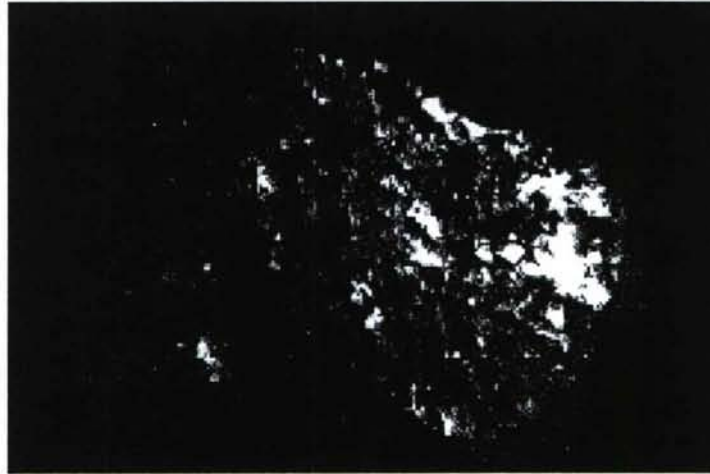


Figure 4.13 Nusselt number as a function of non-dimensional heat flux for both the vertical downward spray and horizontal spray with straight cap.

High speed video was obtained of the spray impingement and droplet ejection or splashing and the time-dependent behavior of the liquid film on the heater surface. A Redlake model SG-LE high-speed digital video camera has been used, in conjunction with a laser light sheet to illuminate slices of the flow (Hunnell, 2005). An example image from a video clip of the droplet impingement and ejection as viewed from the side of the impingement region is shown in Figure 4.14, while two images of the liquid film behavior, viewed from the underside of the transparent ITO heater are shown in Figures 4.15 and 4.16. These results were obtained for the vertical spray at an FC-72 flow rate of 5.4 GPH and a heater power of 17 W, at framing rates of 1000 to 3000 frames per second (fps). The ejected liquid drops appear to be much larger than the 48  $\mu\text{m}$  diameter impinging spray droplets, and move much more slowly (Figure 4.14). Liquid film motion (Figures 4.15 and 4.16) is also much slower than spray droplet velocity (about 1 m/s, versus about 10 m/s). The surface of the liquid film appears to be highly contorted (Figures 4.15 and 4.16), with a series of what appear to be deep craters and ridges apparently formed by the spray impingement and the ejection of the larger droplets. Motion of these larger droplets, as well as the motion of the craters and ridges observed on the surface of the liquid film, is always observed to be in the radial direction.



**Figure 4.14** Interaction between the spray droplets and the ITO pedestal heated surface at 1000 frames per second (fps) at a flow rate of 5.4 GPH and heat flux of  $17 \text{ W/cm}^2$ .



**Figure 4.15** Sample video image of the liquid film and heated surface viewed through the bottom of the pedestal at 3,000 fps at a flow rate of 5.4 GPH and heat flux of 17 W/cm<sup>2</sup>.

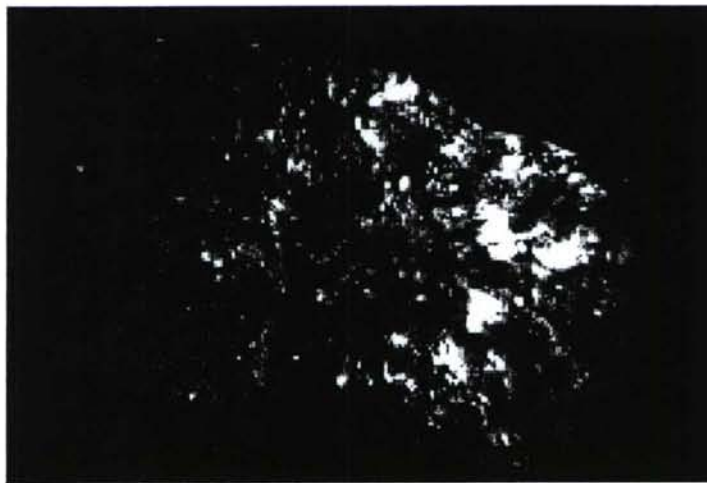


**Figure 4.16** Second sample video image of the liquid film and heated surface viewed through the bottom of the pedestal at 3,000 fps at a flow rate of 5.4 GPH and heat flux of 17 W/cm<sup>2</sup>.

A comparison between the baseline spray cooling performance of a PVC nozzle and two brass nozzles at three flow rates at a nozzle-to-heater spacing of 13 mm is presented in Figure 4.17 and Figure 4.18 (Kreitzer, 2006). These results are again presented in non-dimensional form as  $G\Delta$  versus non-dimensional temperature difference,  $(\Theta_s - \Theta_{\infty-top})$  (Figure 20), and Nusselt number versus  $G\Delta$  (Figure 4.18), as has been described above. Significant variability in the performance of the three nozzles is seen ( $\pm 5\%$  for  $G\Delta$  and  $\pm 10\%$  for Nu), with the two brass nozzles tending to perform somewhat better than the PVC nozzle (cooler surface temperature at the same heat

flux; see Figure 4.17, and higher Nu at the same  $G\Delta$ ; see Figure 4.18). Most of this variability is believed to be due to inaccuracy in realignment of the nozzle with respect to the heater surface when nozzles are replaced.

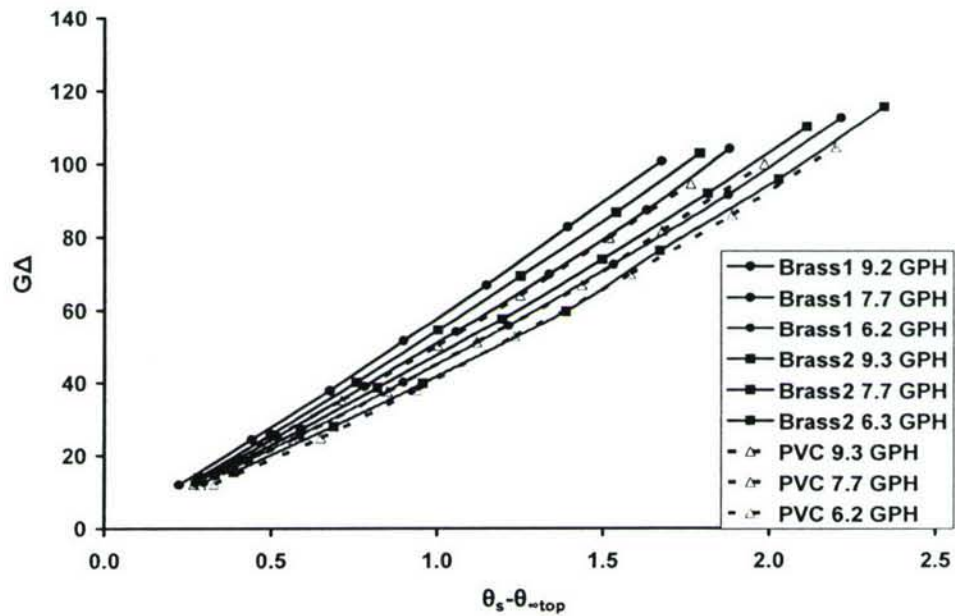


Figure 4.17  $G\Delta$  vs.  $\Delta\theta$  for a PVC nozzle and two brass nozzles (unconfined flow).

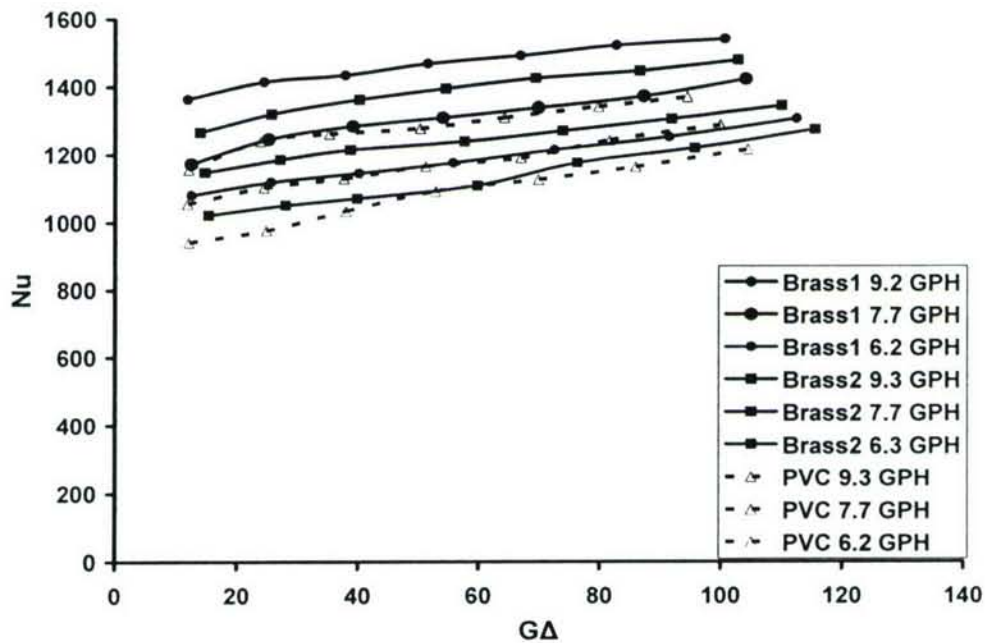


Figure 4.18 Nu vs.  $G\Delta$  for a PVC nozzle and two brass nozzles (unconfined flow).

Similar non-dimensional performance comparisons are shown in Figure 4.19 and Figure 4.20 for variable nozzle-to-heater spacing, with the cap fitted to the sump, for the PVC nozzle at a flow rate of  $8 \times 10^{-6} \text{ m}^3/\text{s}$  (7.7 GPH). Again, significant variations are seen ( $\pm 6\%$  for  $G\Delta$  at fixed temperature difference, and  $\pm 10\%$  for Nu at fixed  $G\Delta$ ), with the nozzle spacing of 9 mm clearly having the worst performance (highest heater surface temperature and lowest Nusselt number at fixed heat flux). Similar trends are seen in data taken without the cap installed on the sump, except that the variability without the cap installed is increased relative to the results shown with the cap in Figure 4.19 and Figure 4.20 ( $\pm 15\%$  for both  $G\Delta$  at fixed temperature difference and for Nu at fixed  $G\Delta$  without the cap; see Glaspell, 2006). The cap thus appears to help to guide any liquid that splashes away from the heater surface back into the liquid film that forms on the heater at the larger nozzle-to-heater spacing, thereby making performance less sensitive to both nozzle spacing and nozzle alignment. Also, results with no cap are consistently better than with the cap at the same flow rate of  $8 \times 10^{-6} \text{ m}^3/\text{s}$  (7.7 GPH). For example, at  $G\Delta = 100$ , the peak Nusselt number for the no cap case is almost 1900, while the confined flow case has a peak Nusselt number of just below 1700 (Glaspell, 2006). Hunnell (2005) saw the same trend for a vertically downward spray at this flow rate, but his trends were reversed at lower flow rates. For a horizontal spray his no cap configuration outperformed either cap geometry at all flow rates. One repeat run by Glaspell (2006) at the same spacing using the same nozzle gave  $\pm 7\text{-}10\%$  variation in both  $G\Delta$  at fixed temperature difference and for Nu at fixed  $G\Delta$ .

It is believed that this observed data variation of approximately  $\pm 5\text{-}15\%$  in either  $G\Delta$  at fixed temperature difference or in the Nusselt number at fixed  $G\Delta$ , both for different nozzles, as well as for the repeat run with the same nozzle at the same nozzle-to-heater spacing, is primarily due to inaccuracy in the re-centering of the spray cone with the centerline of the heater. This observed variability is larger than the nominal  $\pm 3\text{-}7\%$  estimated uncertainties in heat fluxes, temperature differences, and heat transfer coefficients at the higher heat fluxes due to measurement errors.

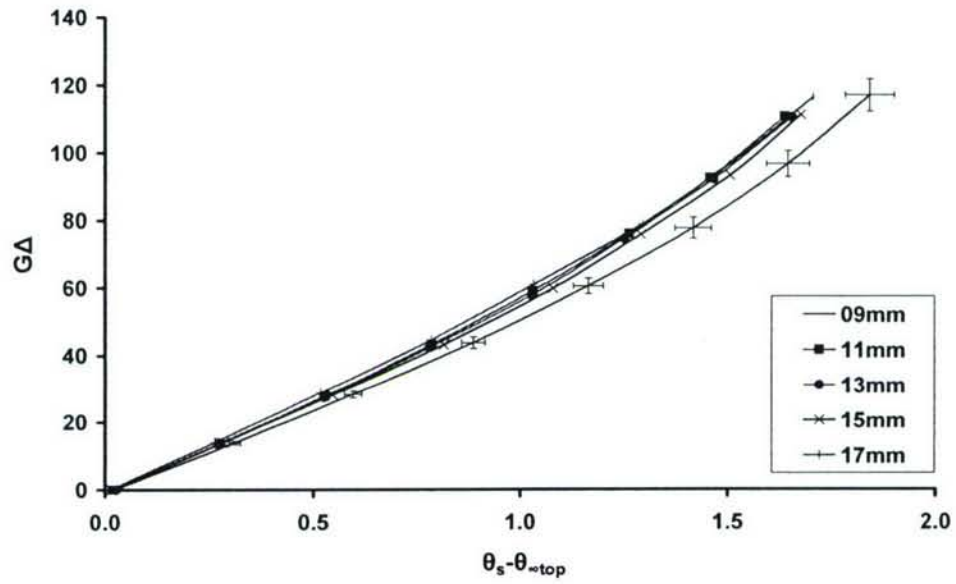


Figure 4.19  $G\Delta$  vs.  $\Delta\theta$  for variable nozzle-to-heater spacing (cap;  $Q = 8 \times 10^{-6} \text{ m}^3/\text{s}$ ).

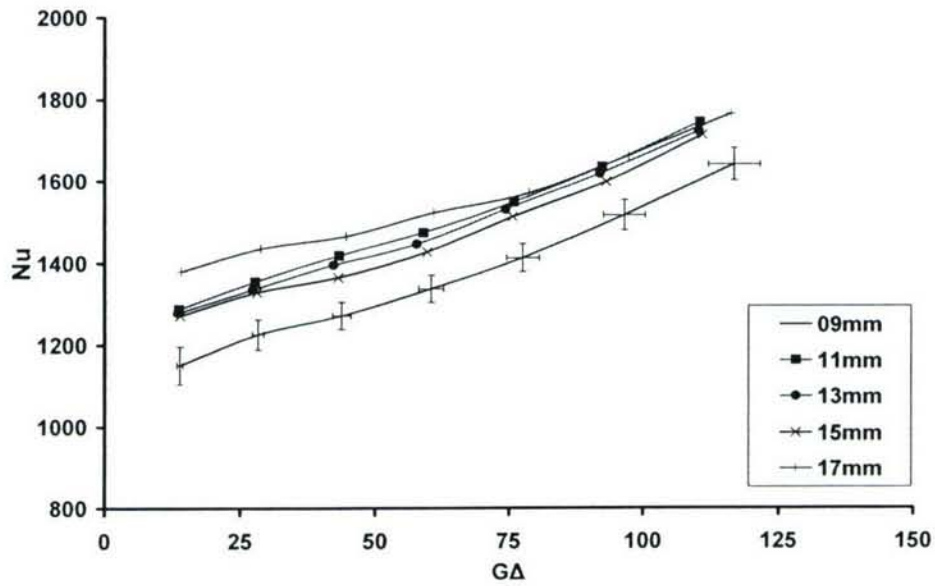
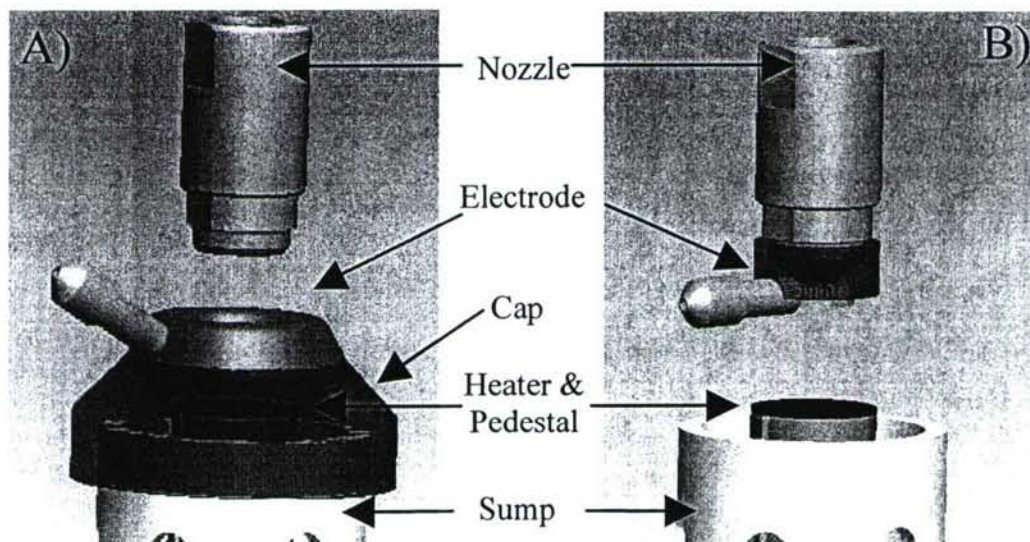


Figure 4.20  $Nu$  vs.  $G\Delta$  for PVC nozzle for variable nozzle-to-heater spacing (cap;  $Q = 8 \times 10^{-6} \text{ m}^3/\text{s}$ ).

## 4.4 Experiments with Electrical Forces

Two types of electrode geometries used in the current study are shown in Figure 4.21. Figure 4.21A shows one of four different electrode designs used in the initial Kelvin body force study. These electrodes are mounted in the cap that is attached to the sump housing the pedestal and heater. The nozzle used in the Kelvin force studies was nonconducting plastic. The electrodes used for Coulomb force studies attach to the spray nozzle as shown in Figure 4.21B. The nozzles used in the Coulomb force studies were made of brass. High voltage for all electrode designs was supplied using a Glassman model EL30R1.5 reversible 0-30 kV power supply, set to negative polarity.



**Figure 4.21** Electrode Geometries for electric body force studies: A) Example of initial electric Kelvin force electrode geometry, B) Example of inductive charging Coulomb force electrode geometry.

### 4.4.1 Electric Kelvin Force Experiments

All four initial Kelvin force electrode geometries are shown in Figure 4.22; results will only be presented for the electrode shown on the right hand side of this figure because the results were similar for all. The complete set of results for all four of these electrodes has been presented in the thesis by Glaspell (2006). The electrode on the right of Figure 4.22 is termed the “full cap” electrode since it extends the full length of the inside of the flow confining cap. The initial Kelvin force electrodes were designed simply based on geometrical constraints to fit inside of the flow management cap. A second-generation Kelvin force electrode was designed using the multiphysics code, CFD-ACE+ as explained in Chapter 3, Section 3.3.2.

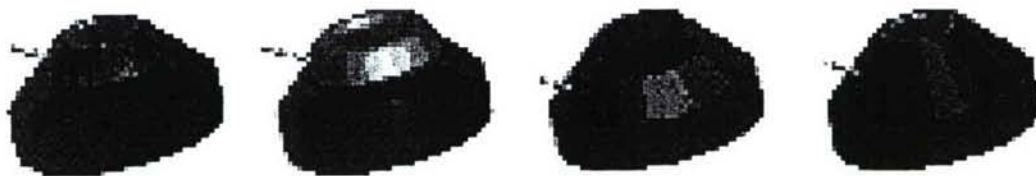


**Figure 4.22 Four initial electric Kelvin force electrode geometries; full cap geometry on right.**

Heat transfer performance data using the initial electric Kelvin force electrode geometries shown in Figure 4.21A and Figure 4.22 (termed “cap electrodes”) have been obtained in the present study for applied voltage levels up to 6 kV. This limitation on applied voltage is necessary to prevent arcing due to the small clearance of only 2.5 mm between these electrode geometries and the heater, which is the nearest grounded metal surface. These data were initially presented by Kreitzer et al. (2006).

Measured non-dimensional heat flux,  $G\Delta$ , is shown for the full cap electrode versus the non-dimensional temperature difference in Figure 4.23 for a spray flow rate of  $8.0 \times 10^{-6} \text{ m}^3/\text{s}$  (7.6 GPH); see the thesis by Glaspell (2006). The working fluid was FC-72, and a negative polarity was applied to the electrode. Clearly, at these electrode voltages there is no noticeable effect of the Kelvin force on spray cooling performance, even for  $G\Delta$  values above 60, where the nonlinearity of the curve indicates two-phase heat transfer. Corresponding Nusselt number data are shown versus  $G\Delta$  in Figure 4.24. Nusselt number increases versus  $G\Delta$  from around 1200 to around 1800, and enhancement due to phase change is apparent, but again there is no noticeable effect of the applied electrode voltage. Since no effects due to the electrode voltage are observed, these results can be interpreted as demonstrating the very good repeatability that is achievable in the current apparatus when no modifications or realignment of the apparatus have occurred between data runs. For the other three cap electrode geometries, again no significant effect was found for the electric field, so similar levels of data repeatability were documented (5% or better; see Glaspell, 2006). Consistent but small improvements in performance (no more than 5%) were seen for this electrode geometry at high  $G\Delta$  using HFE-7000 (Glaspell, 2006).

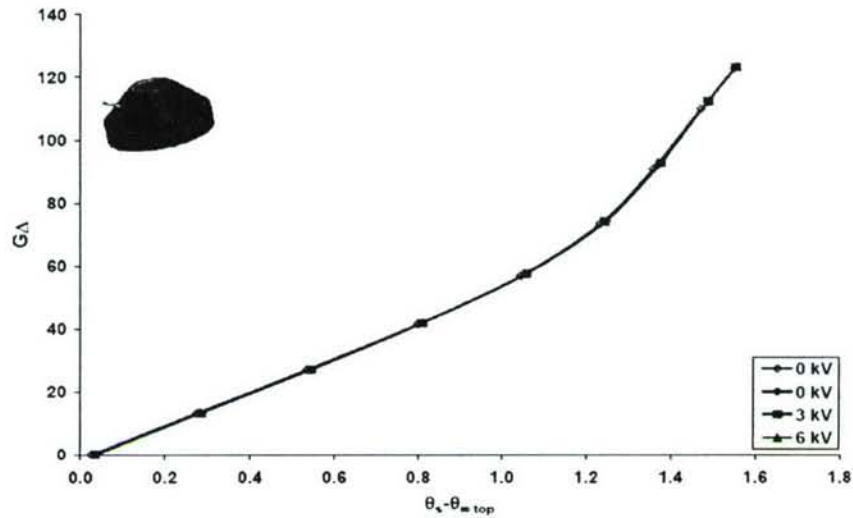


Figure 4.23  $G\Delta$  vs.  $\Delta\theta$  for full cap Kelvin force electrode: FC-72 for 0 kV-6 kV voltage.

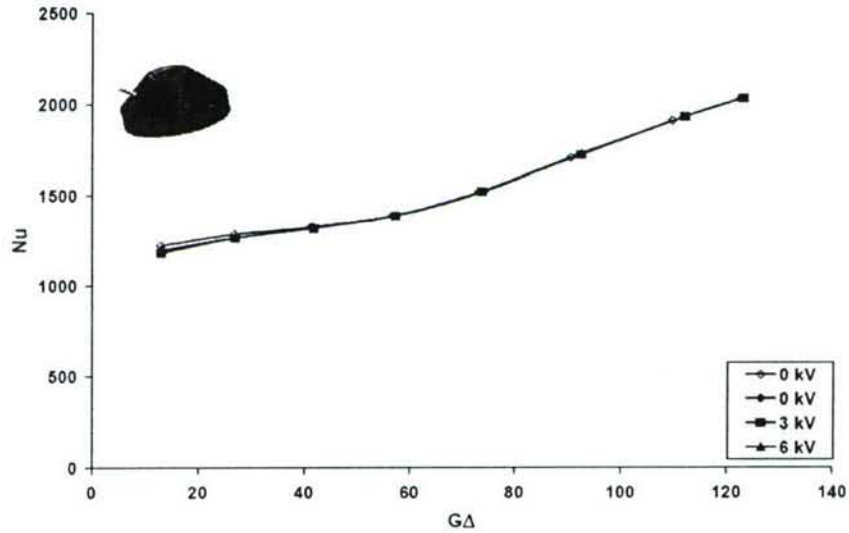


Figure 4.24  $Nu$  vs.  $G\Delta$  for PVC nozzle for full cap Kelvin force electrode: 0 kV-6 kV voltage.

Some understanding of the cause of these negative results was obtained from simulations of the electric field strength using the multiphysics code, CFD-ACE+. The computed electric potential at an electrode voltage of 6 kV for the full cap electrode is shown in Figure 4.25, while the resulting x-component of the Kelvin force per unit mass normal to the heater surface is shown in Figure 4.26 for FC-72, at several x-distances above the heater. Glaspell (2006) has presented similar results for the other three cap electrodes. This computed normal force is downwards toward the heater, and is largest near the outer radius of the heater. The computed radial component of force is similar in magnitude and is directed away from the centerline. It is apparent that the predicted Kelvin force is extremely small over the inner 50-70% of the heater radius.

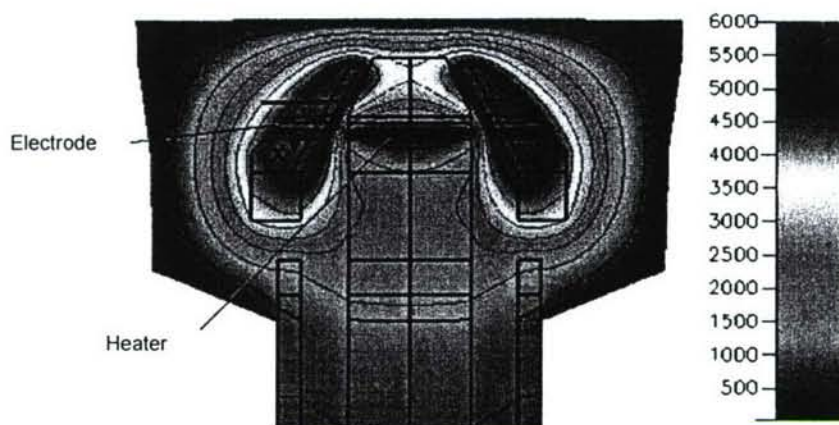


Figure 4.25 Calculated electric potential from CFD-ACE+ for full cap Kelvin force electrode at 6 kV electrode voltage.

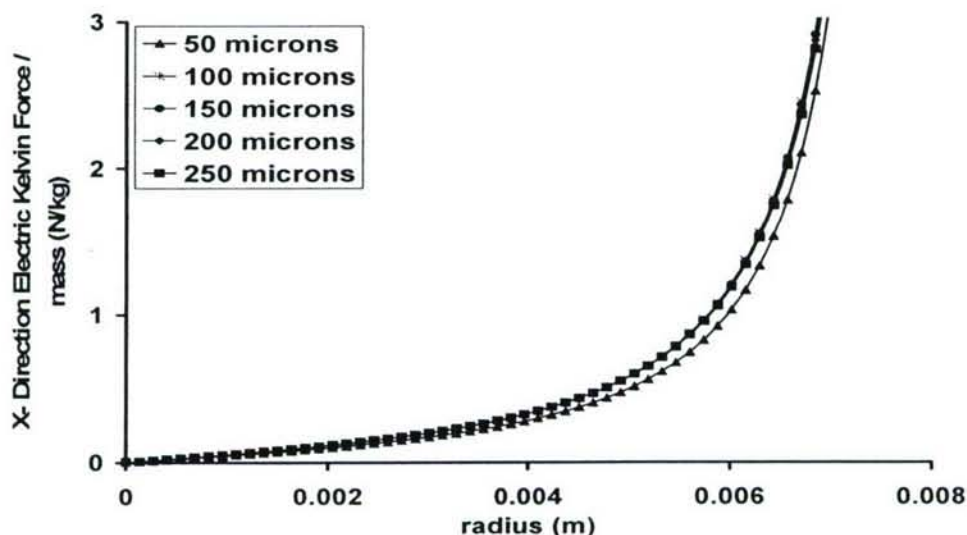
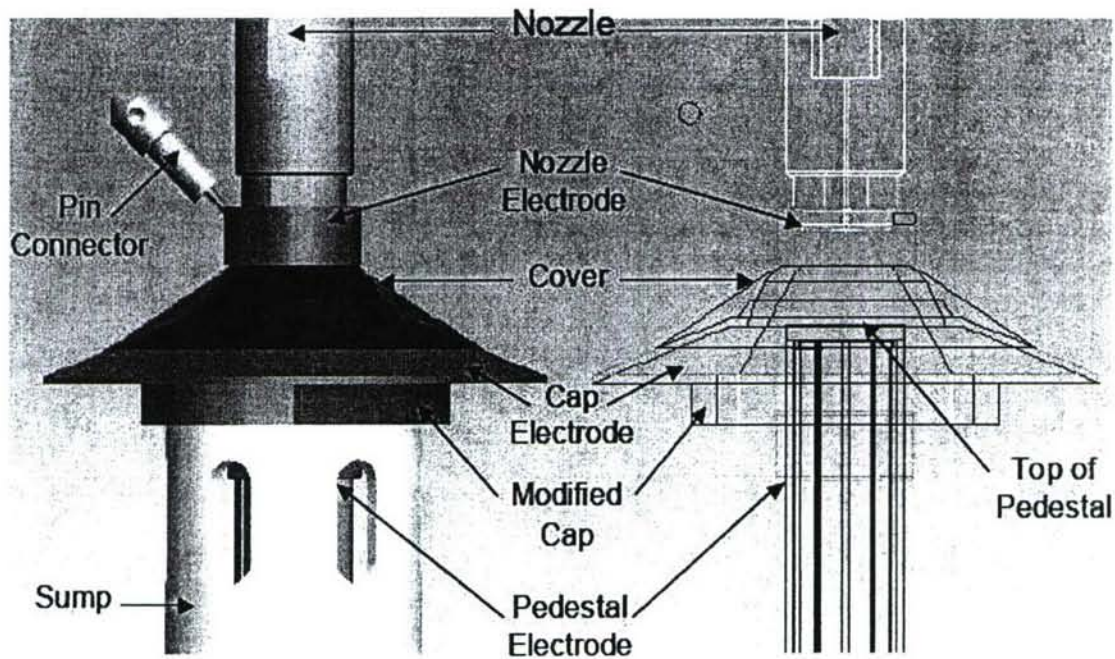


Figure 4.26 Calculated Kelvin force per mass normal to heater surface, from CFD-ACE+, for FC-72 and full cap Kelvin force electrode at 6 kV electrode voltage: various distances normal to heater.

Following the failure of the previous Kelvin force electrodes to produce a significant effect, a second-generation Kelvin force electrode geometry was designed using the CFD-ACE+ multiphysics code. It was desired to have as uniform as possible an electric Kelvin force acting away from the heated surface on which the impingement took place rather than towards the heater surface as for the four cap electrodes shown in Figure 4.22. Details of the design procedure and the resulting design are given in Chapter 3, Section 3.3.2.

The second generation system of electrodes consisted of three different electrodes. Figure 4.27 gives a view of the three electrodes. The charged electrode is attached to the PVC spray nozzle, one ground electrode is shaped like a cymbal and attached to the cap, and the second ground electrode is ring-shaped and fits around the pedestal post inside the sump. Since the heater is a metal, it is an equipotential surface (12 volts), and the field lines are normal to it. If the heater was at the top of the pedestal, the electric field lines would be normal to the impingement surface, preventing an axial Kelvin force from occurring at the impingement surface. Therefore, the heater was moved from its initial location to be 2 mm below the top surface of the pedestal. The distribution of Kelvin force produced by this electrode system is described in Chapter 3.



**Figure 4.27 Second-generation Kelvin force electrode designed using CFD-ACE+.**

Preliminary non-dimensional performance results for this Kelvin force electrode design using HFE-7000 at a spray flow rate of  $4.0 \times 10^{-6} \text{ m}^3/\text{s}$  (3.8 GPH) are summarized in Figure 4.28 and Figure 4.29 (Glaspell, 2006). Modest, but consistent improvements in performance are noted at the higher surface temperatures and heat fluxes (on the order of 6% at a nominal  $G\Delta$  value of 34), even though only relatively modest heat flux levels have been achieved in the current study. A reduction in heater surface temperature of approximately  $2^\circ\text{C}$  at constant heat flux as a nozzle electrode voltage of 23 kV is applied is observed in the dimensional plot of the data shown in Figure 4.28. This results in increases in the heat transfer coefficient on the order of 5%; see Figure 4.29. It is noted that these enhancements are only observed at the higher heat fluxes, where two-phase conditions prevail in the liquid film on the heater surface. The limitations on heat flux resulted from design choices and from the adhesives used in the construction of this electrode and pedestal; see Glaspell (2006) for a detailed description of the design. As explained

previously, the TFR heater was mounted under a 2 mm thick alumina layer which caused pedestal temperatures that could melt the adhesive used to bond the layers.

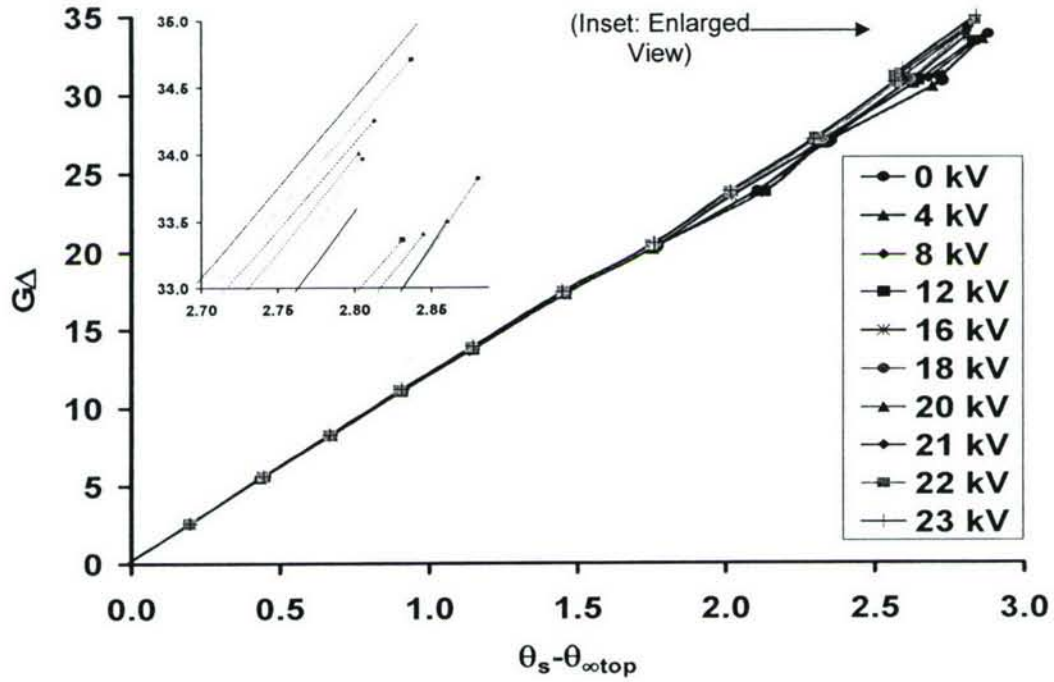


Figure 4.28 Heat transfer performance for second-generation Kelvin force electrode:  $G\Delta$  vs.  $\Delta\theta$ ; inset: enlarged view at high  $G\Delta$ .

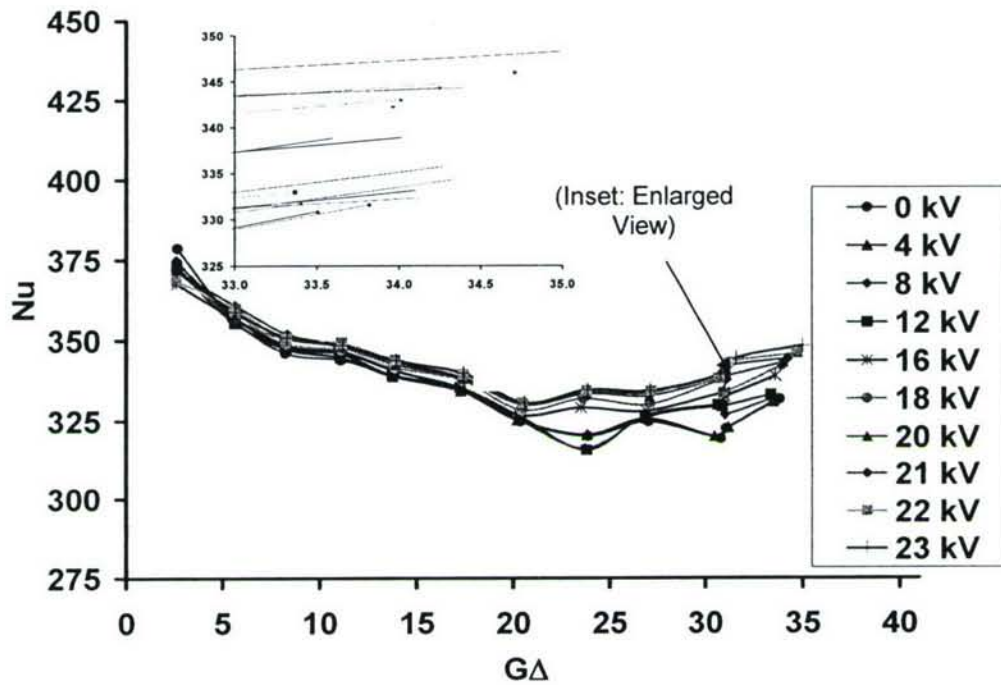


Figure 4.29 Heat transfer performance for second-generation Kelvin force electrode:  $Nu$  vs.  $G\Delta$ ; inset: enlarged view at high  $G\Delta$ .

#### 4.4.2 Coulomb Force Experiments

The Coulomb force electrodes were designed by attempting to follow the recommendations of Law (1978) for inductive charging of the spray droplets. Schematics of the two different Coulomb force electrode designs are shown in Figure 4.30. Electrode thickness for both Coulomb force electrodes is 2.5 mm (0.1").

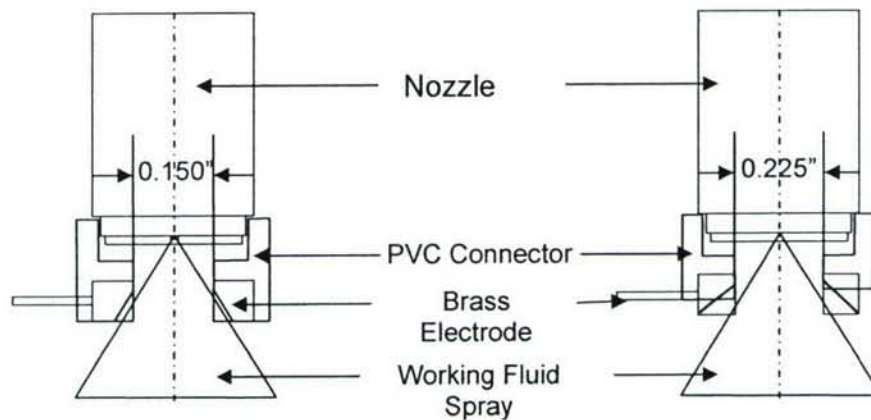
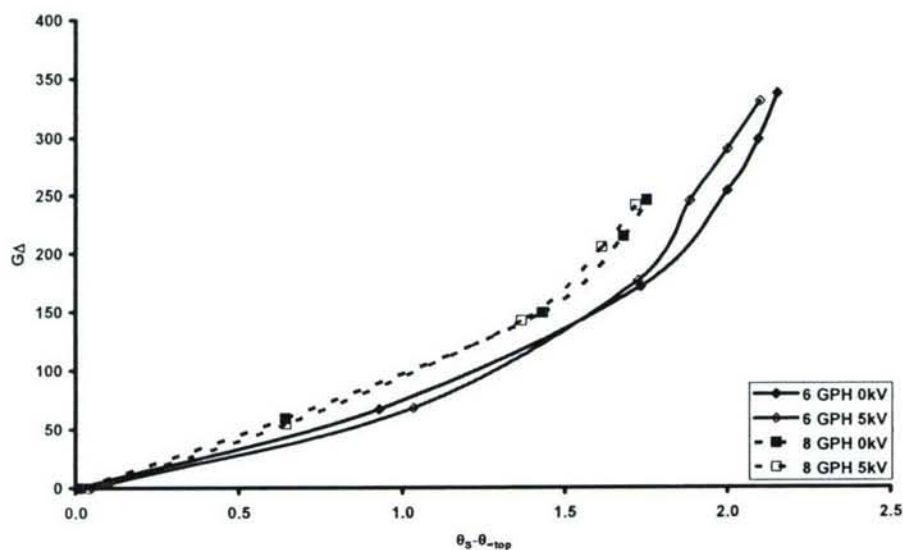


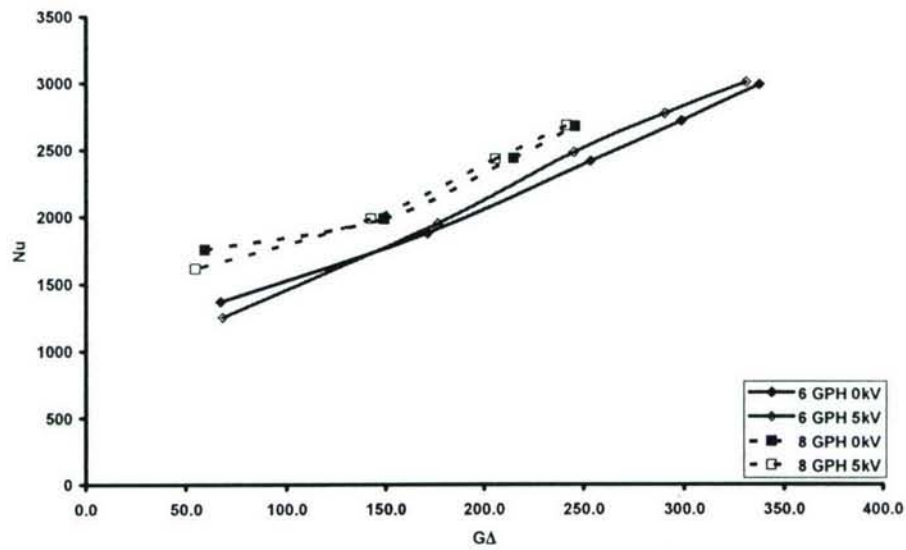
Figure 4.30 Schematic of electrode configurations; left – electrode 1; right – electrode 2.

The complete results using the Coulomb force electrode geometries shown in Figures 4.21B and 4.30 for a vertical downward spray have been presented in detail by Kreitzer (2006), and summarized by Kuhlman et al. (2007). The present data for the Coulomb force electrodes have been obtained for applied voltage levels of up to 5 kV. This limitation on applied voltage is due to the small clearance of only 2.5 mm between these electrodes and the nearest grounded metal surface, the spray nozzle.



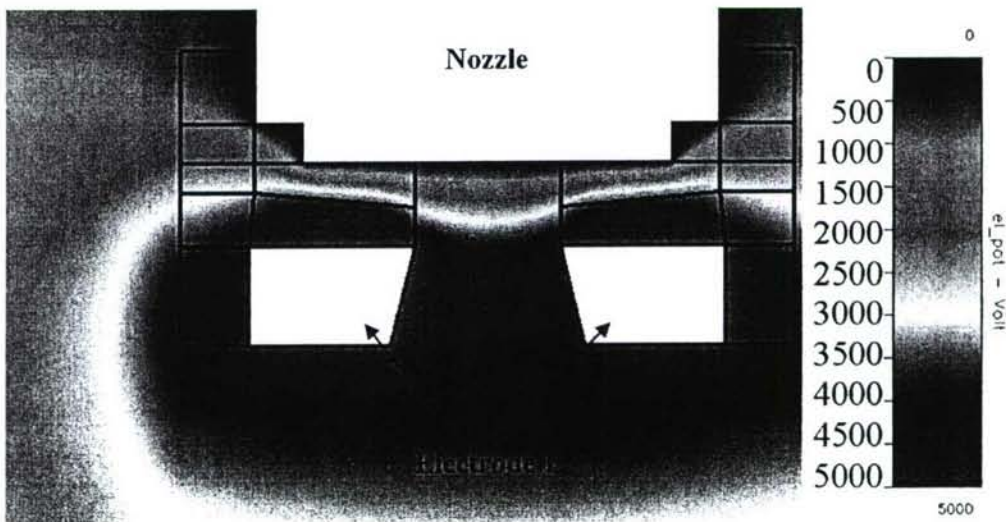
**Figure 4.31 Non-dimensional heat flux versus temperature difference for HFE-7000 using TFR heater and Coulomb force electrode 1 at flow rates of 6 and 8 GPH.**

Figure 4.31 presents the measured nondimensional heat flux,  $G\Delta$ , as defined in Equation (4.1) versus the nondimensional temperature difference between the heater surface and the impinging liquid spray coolant for Coulomb force electrode 1 for two different spray flow rates. Spray flow rates were  $8.4 \times 10^{-6}$  and  $6.3 \times 10^{-6} \text{ m}^3/\text{s}$  (8 and 6 GPH). Here the coolant was HFE-7000, and a 5 kV negative polarity voltage was applied to the electrode. Clearly, at these electrode voltages, there is a modest but consistent enhancement in the heat transfer (up to a 13-17% increase in heat flux or  $G\Delta$  at the same surface temperature or  $\Theta$ ) for  $G\Delta$  values above around 150 for both spray flow rates, where the nonlinearity of the curve clearly indicates two-phase heat transfer. Corresponding Nusselt number data are shown versus  $G\Delta$  in Figure 4.32. Nusselt number increases at the same  $G\Delta$  of up to 14% are seen, again at the onset of phase change beyond  $G\Delta \geq 150$ . Note that the heat transfer enhancement appears to diminish as the CHF is approached. Also, a slightly larger percentage increase in heat transfer is observed at the lower spray flow rate; this may be due to the lower droplet velocities and resulting longer droplet charging times.



**Figure 4.32** Nusselt number versus non-dimensional heat flux for HFE-7000 using TFR heater and Coulomb force electrode 1 at flow rates of 6 and 8 GPH.

The electric potential exerted by both electrodes has been calculated using the CFD-ACE+ multiphysics code. Axisymmetric results for electrode 1 are shown in Figure 4.33. Similar results are presented in Kreitzer (2006) for electrode 2. For these simulations the electrode was held at 5 kV and the nozzle and pedestal were fixed at 0 kV. The computed electric field strength for this electrode is shown in Figure 4.34. Results versus distance along the spray centerline are shown in Figure 4.35, in units of N/C. These results have been used to estimate the magnitude of the Coulomb force on a spray droplet on the centerline, using calculated values of the induced charge (Kreitzer, 2006).



**Figure 4.33** Electric potential for Coulomb force electrode 1, computed using CFD-ACE+.

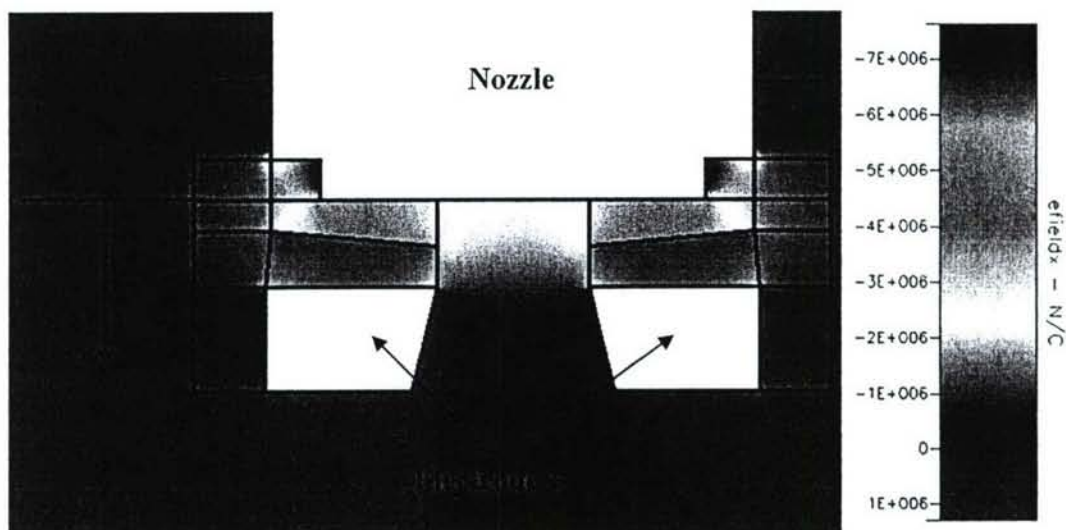


Figure 4.34 E field magnitude (N/C) for Coulomb electrode 1, computed using CFD-ACE+.

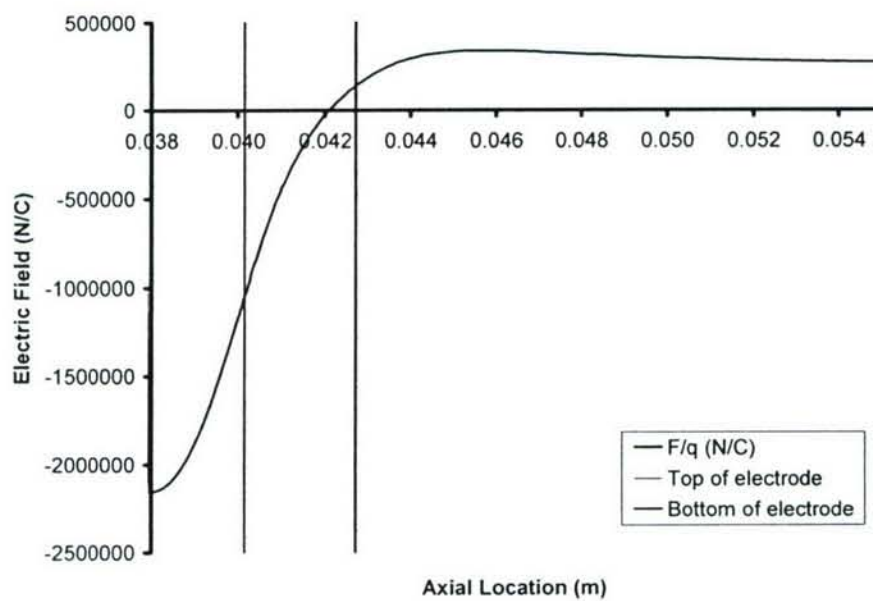


Figure 4.35 E field magnitude along the centerline for Coulomb force electrode 1, computed using CFD-ACE+, presented in N/C.

The charge applied to each droplet,  $q_p$ , has been computed using Equation 4.4 (Law, 1978).

$$q_p = \frac{m_p 2\epsilon_0 V}{r_p r_j^2 \ln\left(\frac{r_c}{r_j}\right)} \quad (4.4)$$

where,  $\epsilon_0$  is the permittivity of air ( $8.85 \times 10^{-12} \text{ C}^2/\text{N}\cdot\text{m}^2$ )

$r_p$  is the radius of the droplet

$r_c$  is the outer radius of the electrode

$r_j$  is the radius of the liquid jet

$m_p$  is the droplet mass

$V$  is the applied charging voltage.

The computed value is only approximately 1.5% of the Rayleigh limit, which is the maximum charge that can be placed on the droplet without shattering it (Law, 1978). The resulting computed charge and the Coulomb force per mass at locations at the top and the bottom of electrode 1 are shown in Table 4.1 (Kreitzer, 2006). Even with the modest computed levels of charge relative to the Rayleigh limit, the computed forces are appreciable. It is believed that the actual levels of charge achieved on the electrodes may have been less than listed in Table 1, due to non-optimal axial spacing of the electrodes, and/or inadequate charging time.

**Table 4.1 Computed droplet charge and resulting Coulomb force exerted on the droplet at the top and bottom of electrode 1.**

|         | Electrode 1 with FC-72 |                     |                     | Electrode 1 with HFE-7000 |                     |                     |
|---------|------------------------|---------------------|---------------------|---------------------------|---------------------|---------------------|
| Voltage | $q_p$                  | $F_{p \text{ top}}$ | $F_{p \text{ bot}}$ | $q_p$                     | $F_{p \text{ top}}$ | $F_{p \text{ bot}}$ |
| (V)     | (C)                    | (N/kg)              | (N/kg)              | (C)                       | (N/kg)              | (N/kg)              |
| 0       | 0.00                   | 0.00                | 0.00                | 0.00                      | 0.00                | 0.00                |
| -1000   | -2.17E-15              | 24.13               | -3.21               | -2.17E-15                 | 28.95               | -3.86               |
| -2500   | -5.43E-15              | 60.32               | -8.03               | -5.43E-15                 | 72.38               | -9.64               |
| -5000   | -1.09E-14              | 120.64              | -16.06              | -1.09E-14                 | 144.76              | -19.28              |
| -6000   | -1.30E-14              | 144.76              | -19.28              | -1.30E-14                 | 173.71              | -23.13              |

## CHAPTER 5 TIME SCALE ESTIMATES

Order-of-magnitude estimates have been made by Kuhlman et al. (2007) of the time scales for FC-72 for physical phenomena that are expected to be relevant in spray impingement cooling, in an effort to develop some understanding of how a body force might be able to influence spray cooling performance. First, a kinematic time scale has been computed as the time between droplet impacts onto a region of the heater surface equal to the estimated area of the thin liquid film “crater” that forms due to the previous droplet impact. Droplet size has been assumed to be  $48\text{ }\mu\text{m}$  (Yerkes et al., 2006), and crater diameter has been assumed to be  $250\text{ }\mu\text{m}$ , based on initial high speed video imaging of the liquid film viewed from below using the transparent ITO heater. Two example frames from one of these visualizations appear in Figure 5.1. For these images, the liquid film was illuminated using the beam of a 2 W Argon-ion CW laser formed into a light sheet that was oriented parallel to the heater surface. A Phantom v4.2 digital high speed video camera was used, operated at 15 000 frames per second (fps), using a macro lens at f8 and a  $10\text{ }\mu\text{s}$  shutter. The curved edge of the heater is visible in the left and right side of both images. Also visible are the  $250\text{ }\mu\text{m}$  (0.01”) diameter thermocouples that have been embedded in the pedestal. These help provide a scale in the images. If it is assumed that the dark regions visible in both images are associated with recent droplet impacts, then these crater regions are estimated to be between 200-500  $\mu\text{m}$  in diameter. Based on this observation, along with measurements by Bernardin et al. (1996), a value of  $250\text{ }\mu\text{m}$  has been assumed for the crater diameter.

The estimated thickness of the liquid film on the heater surface away from any droplet impact regions ( $150\text{ }\mu\text{m}$ ) is from measurements by Tilton (1989). Pautsch et al. (2004) have reported spray impingement cooling liquid film thicknesses ranging between  $80\text{ }\mu\text{m}$  and  $300\text{ }\mu\text{m}$ . The assumed liquid film thickness in the region of droplet impact ( $1.5\text{ }\mu\text{m}$ ) has then been computed based on the assumed value of the crater diameter ( $250\text{ }\mu\text{m}$ ), and assuming no splashing. Cossali et al. (1997) have developed a criterion (3.21) for the onset of splashing due to droplet impingement onto a surface covered with a preexisting liquid film. This criterion predicts no splashing for  $48\text{ }\mu\text{m}$  Sauter mean diameter droplets, but somewhat larger droplets are predicted to splash. Cole et al. (2005) used computational fluid dynamics to simulate these phenomena; their simulations agree qualitatively with the experimental observations by Cossali et al.. These values, along with other key dimensional parameters used in the time scale estimates, have been listed in Table 5.1.

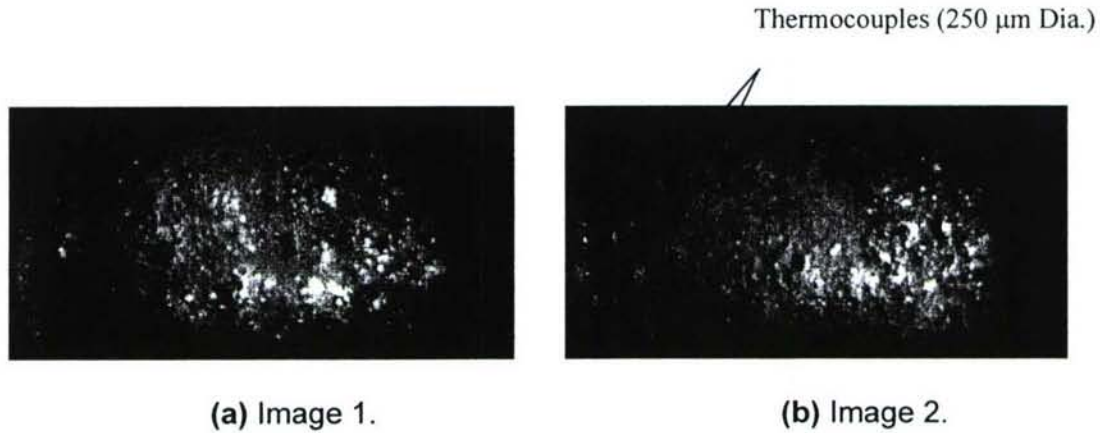


**Figure 5.1** Sample video images of liquid film on heater surface, at heater power = 57 W, FC-72 flow rate = 9.5 GPH.

**Table 5.1** Assumed parameter values for time scale analysis using FC-72 properties.

| Parameter  | Value                 |
|--|-----------------------|
| Droplet Diameter <sup>1</sup> ( $\mu\text{m}$ )                            | 48                    |
| Liquid Film Thickness <sup>2</sup> ( $\mu\text{m}$ )                       | 150                   |
| Droplet Impact Crater Dia. <sup>3</sup> ( $\mu\text{m}$ )                  | 250                   |
| Crater Film Thickness ( $\mu\text{m}$ )                                    | 1.5                   |
| Heater Dia. (mm)   | 16                    |
| Active Heater Area ( $\text{m}^2$ )  | $1.46 \times 10^{-4}$ |
| Assumed Heater Power (W)   | 100                   |
| Assumed Liquid Subcooling ( $^{\circ}\text{C}$ )                           | 30                    |
| Spray Flow Rate ( $\text{m}^3/\text{s}$ )                                  | $1.05 \times 10^{-5}$ |
| Spray Droplet Flux to Heater ( $\text{s} \cdot \text{m}^2$ ) <sup>-1</sup> | $9.0 \times 10^{11}$  |

Source: <sup>1</sup>Yerkes et al., 2006, <sup>2</sup>Tilton, 1989, <sup>3</sup>Bernardin et al., 1996.

The calculated time scales have been based on typical assumed values of the spray flow rate and heater power of  $1.05 \times 10^{-5} \text{ m}^3/\text{s}$  and 100 W, respectively. Two different kinematic time scales for droplet impacts have been computed: the average time between droplet impacts on the heater surface for an area equal to the cross sectional area of an incoming drop (610  $\mu\text{s}$ ) and the average time between droplet impacts into the estimated area of a previous droplet impact crater (22  $\mu\text{s}$ ); see Table 5.1. These known flow time scales are compared to the estimated time to heat the drop to saturated conditions and to vaporize the drop, the time scale for surface tension phenomena, and the gravity time scale in Table 5.2. Surface tension and gravity time scales have been computed by setting the Weber and Froude numbers equal to one to compute velocity scale estimates, and then using these velocities to compute time scales for the propagation of a surface wave from the outer edge of a droplet impact crater to the center. Thus, these times scales are

representative of the times for a droplet impact crater to fill in under the influence of surface tension or gravity. Note that the time to vaporize the drop liquid in the crater would be nearer to the time between droplet impacts in a crater if the heater power was larger (say, 200 W), or if there was significant splashing of the drop away from the crater. Flow visualization for the present sprays indicates the existence of significant splashing. For some spray impingement conditions it is possible for this splashed mass to exceed that of the impinging droplet (Cole et al., 2005). It is speculated that this splashing could result in less of the impinging droplet liquid remaining in the thin film left in the crater formed by droplet impact, thereby allowing localized dryout of these portions of the heater surface prior to the next droplet impact into the crater. This localized dryout in the droplet impact craters is proposed as a key mechanism for the onset of CHF in spray impingement cooling.

**Table 5.2 Estimated time scales using parameters from Table 5.1.**

| Time Scale                                | Value ( $\mu\text{s}$ ) |
|---|-------------------------|
| Time Between Droplet Impacts at Same Spot | 610                     |
| Time Between Droplet Impacts In Crater    | 22                      |
| Time to Vaporize Drop                     | 224                     |
| Time to Heat Drop to $T_{sat}$            | 87                      |
| Surface Tension Time                      | 720                     |
| Gravity Time Scale                        | 3900                    |
| Droplet Charging (Charge Relaxation) Time | 66                      |
| Residence Time for Droplet at Electrode   | 130                     |

For the assumed length scales in Table 5.1, it appears that the time scale for gravitational effects is considerably longer than any of the time scale estimates for the other phenomena. This leads to the conclusion that gravitational effects would not be expected to be capable of causing a significant effect on spray cooling performance, at least for the range of parameters assumed in Table 5.1. A possible exception to this conclusion may be the governing time scale for the formation and/or detachment of the small vapor bubbles that form in the liquid film during boiling. Since increased heat transfer in the present work is only observed during boiling, it is reasonable to assume that these phenomenon may be influenced by the Coulomb and/or gravitational body force. However, in the present work, no vapor bubble time scales have been estimated.

It is noted that the droplet residence time at the electrode is comparable to the charge relaxation time (Law, 1978; see Table 5.1); this indicates that the actual inductive charge achieved on a droplet in the current work could be comparable to the value computed from Equation (4.4), assuming that the electrode has been placed at the axial location where the liquid jet breaks up into droplets. It is not known whether or not this has been the case for the present work. Because of the limited charging voltages achievable for inductive charging, it is recommended that contact charging be explored in future experiments, as well as inductive charging using different electrode spacings.



## CHAPTER 6 CONCLUSIONS AND RECOMMENDATIONS

Several flows that embody phenomena that occur in spray impingement boiling were simulated using the state of the art commercial multiphysics code CFD-ACE+. All of the simulations were performed using single processor personal computers, and all assumed two dimensional axisymmetric flow.

The experiments of Labus (1977) in which an isothermal jet impinged on a sharp edge disk in microgravity ( $\mu g$ ) were simulated using the Flow and Free Surfaces modules of CFD-ACE+. The code was able to reproduce the qualitative behavior of the surface tension and inertial flow regimes as seen in moving and still photos of the experiments. A quantitative comparison of the shape of the free surface in the inertial regime was also in good agreement, given the uncertain parameter values for the experiment.

The Flow, Free Surfaces, and Heat Transfer modules were used to simulate the experiment of Liu and Lienhard (1989) in which a round jet impinged on a constant heat flux surface. There was no significant phase change in this experiment. The computed values of local Nusselt number as a function of distance from the impingement point showed good agreement with the experimental data, generally within the experimental uncertainty bounds.

An experiment of Pasandideh-Fard et al. (1996) in which a droplet impacted a dry wall was simulated with the Flow and Free Surfaces modules. The simulations reproduced the spread and rebound of the droplet, although the simulations were stopped before the rebounding droplet would have left the surface. The ratio of the maximum radius of spread to the drop diameter showed a sensitive dependence on contact angle which agreed with the experimental data.

The Flow and Free Surfaces modules were also used to simulate the impact of a droplet on a liquid film. A relatively coarse grid was sufficient to show the formation of the crown and the Worthington jet, including the pinch-off of a droplet. The ejection of the droplet was in agreement with the experimental splashing criterion of Cossali et al. (1977). With a much finer grid, additional details of the flow became visible, notably the ring jet observed experimentally by Thoroddsen (2002). To resolve this phenomenon required a grid having  $0.3 \mu m \times 0.3 \mu m$  cells.

CFD-ACE+ was modified to allow the inclusion of the Coulomb and electric Kelvin forces. As supplied, the program did not provide for the electric field to be altered by the motion of charged droplets or particles, nor did it compute the Coulomb forces among droplets. Coding changes were made to allow for these phenomena. The interaction of spray drops and liquid layers is not fully understood, so it could not be properly modeled by the code. In particular, the fate of free charge carried by droplets when they impinge on a wall or liquid film requires further study. Two new boundary conditions were added to the code to account for the limiting cases of an insulated wall and a grounded perfectly conducting wall. No progress was made toward the physically correct treatment of the general case.

The source term for the electric Kelvin force was added to the CFD-ACE+ Flow module and fully coupled to the electric field calculated by the Electric module. The flow of a round free jet in the WVU experimental geometry was simulated with no body force, with terrestrial gravity in the initial direction of the jet, and with terrestrial gravity opposed by the electric Kelvin force generated by the second generation electrode. Gravity was found to accelerate the jet as expected. Because the Kelvin force is highly nonuniform in space, it distorted the jet and appeared to create free surface waves near the impact zone. This result confirms that significant electric Kelvin forces can be created in the vicinity of a heated surface.

Although much was accomplished in the computational phase of the WVU project, the goal of simulating a spray with boiling on the impingement surface was not reached, primarily because the computational requirements exceeded the capabilities of the Pentium 4 class single processor personal computers that were used. Recognizing that fully three dimensional simulations involving phase change and large numbers of droplets are needed to accurately simulate spray impingement boiling, it appears certain that much more powerful computers, probably using parallel computation, will be required for the foreseeable future in order to simulate problems of this complexity. In addition, significant gaps in physical understanding concerning the interaction of both uncharged and charged sprays with liquid films and solid surfaces were encountered. The microphysics of bubble growth in flow boiling is another key area requiring more research. Progress in simulating spray impingement boiling will require better understanding of these phenomena.

An apparatus was constructed with assistance from AFRL researchers that was closely patterned after their spray impingement boiling experiment. In the WVU apparatus, a single full-cone spray nozzle sprays a dielectric coolant onto a circular resistive heater. Both ceramic Thick Film Resistor (TFR) and optically-transparent Indium-Tin-Oxide (ITO) heaters have been used. Flow management is sometimes provided by a conical cap surrounding the heater area that directs the excess liquid spray into an annular sump to be recirculated. This WVU apparatus is identical to the AFRL apparatus with the exception of the necessary high-voltage feedthroughs and electrodes to electrically control the spray.

Without electrical body force effects, heat transfer performance in Earth gravity for both vertical downward and horizontal spray impingement has been documented for spray flow rates between  $4.8 \times 10^{-6} \text{ m}^3/\text{s}$  and  $9.8 \times 10^{-6} \text{ m}^3/\text{s}$  (4.6 GPH to 9.3 GPH), and heater power levels from 10 W to 70 W using the TFR heater. As flow rate is increased at fixed heater power the heat transfer effectiveness increases, as indicated by reduced heater surface temperatures and increased heat transfer coefficients. Generally, heat transfer effectiveness for the vertical downward spray and horizontal spray configurations are nearly identical, but the horizontal spray has somewhat better heat transfer performance for the unconfined flow at the highest flow rate of 9.3 GPH. The ITO heater consistently has somewhat better performance than the TFR heater. Heat transfer coefficient increases with increased spray flow rate, but is only weakly dependent on the heater power level. Without the electrical body forces, different brass and PVC spray nozzles show significant variations in spray cooling performance (order of  $\pm 5\text{-}15\%$ ) whenever the nozzle is realigned. Changing the nozzle-to-heater spacing results in similar performance variations, again largely due to nozzle realignment. Flow visualization of the spray and liquid film motion using a high speed digital video camera and laser light sheet illumination indicates a highly contorted

free surface for the liquid film that forms on the heater surface. Outward radial motion of the wave-like craters and ridges that form on the interface is observed.

Results have also been obtained for a study of the effects of electrical body forces on heat transfer performance of the identical instrumented spray nozzle and heater. Heat transfer performance was documented for ranges of electrode voltage, and for similar ranges of spray volume flow rate and heater power level using a TFR heater. An initial series of Kelvin force electrode designs showed no improvement in heat transfer performance using FC-72, while a second-generation Kelvin force electrode that was designed using the Electric module of the CFD-ACE+ code showed modest but consistent improvements (order of 10% in heat flux; order of 5% for Nusselt number) using HFE-7000. These heat transfer enhancements are seen only during two phase cooling. Two Coulomb force electrode geometries also showed modest but consistent improvements in heat transfer (order of 5-15%), but only at heat fluxes where boiling of the liquid film occurs.

The flow visualization results have been used to aid in the estimation of characteristic time scales governing the effects of surface tension, gravity, heating of the liquid film, and vaporization of the film. For the present dense liquid sprays, it is concluded that none of these time scales are as short as the average time between droplet impacts into a heater surface area equal to the estimated size of the thin, crater-like liquid films formed by a previous droplet impact.

The most significant result of this research is that the fundamental hypothesis that spray impingement boiling heat transfer can be enhanced by electrical fields has been demonstrated for the first time. Neither the Coulomb nor the Kelvin force electrodes used in these tests can be considered to be anywhere near optimal. Therefore, it is expected that significantly greater enhancement of heat transfer by means of electrical forces can still be achieved.

## REFERENCES

- Baysinger, K., Yerkes, K., Michalak, T. E., Harris, R., and McQuillen, J., 2004. "Design of a Microgravity Spray Cooling Experiment," 42nd AIAA Aerospace Sciences Conference and Exhibit, Paper 2004-0966, Reno, NV, January.
- Baysinger, K., 2004. "Experimental Testing and Numerical Modeling of Spray Cooling under Terrestrial Gravity Conditions," M. S. Thesis, Wright State University, Dayton, OH.
- Beam, J., 2000. "Military Spacecraft Thermal Management Needs," Session TP-13, Panel Session Presentation at AIAA 33rd Thermophysics Conference, Denver, CO, June 19-22.
- Bernardin, J. D., Stebbins, C. J., and Mudawar, I., 1996. "Mapping of Impact and Heat Transfer Regimes of Water Drops Impinging on a Polished Surface," *Int. J. Heat and Mass Transfer*, Vol. 39, pp. 247-267.
- Chow, L., Sehmbey, M., and Pais, M., 1997. "High Heat Flux Spray Cooling," *Annual Review of Heat Transfer*, Vol. 8, pp. 291-318.
- Cole, V., Mehra, D., Lowry, S., Gray, D., 2005. "A Numerical Spray Impingement Model Coupled with a Free Surface Film Model," *Proceedings of the 16<sup>th</sup> Annual Thermal and Fluids Analysis Workshop (TFAWS-2005)*, 14 pages.  
[http://www.ustdc.com/tfaws/files/InterdisciplinaryPaperSession/TFAWS05\\_VCole\\_ID.pdf](http://www.ustdc.com/tfaws/files/InterdisciplinaryPaperSession/TFAWS05_VCole_ID.pdf)
- Cossali, G. E., Coghe, A., Marengo, M., 1997. "The Impact of a Spray Drop onto a Liquid Film," *Experiments in Fluids*, Vol. 22, 463-472.
- Darabi, J., Ohadi, M. M., and Dessiatoun, S. V., 2000. "Augmentation of Thin Falling-Film Evaporation on Horizontal Tubes Using an Applied Electric Field," *Journal of Heat Transfer*, Vol. 122, pp. 391-398.
- DiMarco, P. and Grassi, W., 2002. "Motivation and Results of a Long-Term Research on Pool Boiling Heat Transfer in Low Gravity," *International Journal of Thermal Sciences*, Vol. 41, pp. 567-585.
- ESI, 2004. CFD/ESI Ace Manual for CFD Ace Solver, Huntsville, AL.
- Feng, X. and Bryan, J. E., 2005. "Control of Liquid Impingement with Electrical Field," *Proceedings ASME IMECE2005*, Orlando, FL, Nov. 5-11.
- Gebhart, B., Jaluria, Y., Mahajan, R. L., and Sammakia, B., 1988. *Buoyancy-Induced Flows and Transport*, Hemisphere Publishing Corporation, New York.
- Glaspell, S. L., 2006. "Effects of the Electric Kelvin Force on Spray Cooling Performance," M. S. Thesis, West Virginia University, Dept. of Mechanical and Aerospace Engineering, Morgantown, WV.
- Hirt, C.W., and Nichols, B.D., 1981. "A Computational Method for Free Surface Hydrodynamics," *Transactions of the ASME, Journal of Pressure Vessel Technology*, Vol. 103, no. 2, pp. 136-41.

Hughes, W.F. and Young, F.J., 1966. *The Electromagnetodynamics of Fluids*, John Wiley and Sons Inc., New York.

Hunnell, C. A., 2005. "Design, Construction, and Initial Testing of Experimental Test Package for Convective Spray Cooling in Terrestrial Gravity Conditions," M. S. Thesis, West Virginia University, Dept. of Mechanical and Aerospace Engineering, Morgantown, WV.

Hunnell, C. A, Kuhlman, J. M., and Gray, D. D., 2006. "Spray Cooling in Terrestrial and Simulated Reduced Gravity," *Space Technology & Applications International Forum (STAIF-2006)*, AIP Conference Proceedings Volume 813, M. S. El-Genk, editor, 126-133.

Kato, M., Abe, Y., Mori, Y., and Nagashima, A., 1994. "Spray Cooling Characteristics under Reduced Gravity," *Journal of Thermophysics*, Vol. 9, No 2, Technical Notes, pp. 378-381.

Kreitzer, P. J., 2006. "Experimental Testing of Convective Spray Cooling with the Aid of an Electric Field Using the Coulomb Force," M. S. Thesis, West Virginia University, Dept. of Mechanical and Aerospace Engineering, Morgantown, WV.

Kreitzer, P. J., Glaspell, S. L., Kuhlman, J. M., Mehra, D, and Gray, D. D., 2006. "Electrical Force Effects on Spray Cooling," Paper 06PSC-61, SAE 2006 Power Systems Conference, New Orleans, LA, Sept. 7-9.

Kuhlman, J. M., Kreitzer, P. J., Mehra, D., Gray, D. D., and Yerkes, K. L., 2007. "Influence of the Coulomb Force on Spray Cooling," STAIF 11<sup>th</sup> Conference on Thermophysics Applications in Microgravity, Albuquerque, NM, Feb. 11-15.

Labus, T. L., 1977. "Liquid Jet Impingement Normal To A Disk In Zero Gravity", NASA Technical Paper 1017, Lewis Research Center, Cleveland, Ohio.

Labus, T. L. and DeWitt, K. J., 1978. "Liquid Jet Impingement Normal to a Disk in Zero Gravity," *Journal of Fluids Engineering*, Vol. 100, pp. 204-209.

Law, S. E., 1978. "Embedded-Electrode Electrostatic-Induction Spray-Charging Nozzle: Theoretical and Engineering Design," *Transactions of the ASAE*, Vol. 21, pp. 1096-1104.

Lin, L. and R. Ponnappan, R., 2003. "Heat Transfer Characteristics of Spray Cooling in a Closed Loop," *Int. J. Heat and Mass Transfer*, Vol. 46, pp. 3737-3746.

Liu, X. and Lienhard, J.H., 1989. "Liquid Jet Impingement Heat Transfer on a Uniform Flux Surface", National Heat Transfer Conference, HTD-Vol 106, Heat Transfer Phenomena in Radiation, Combustion and Fires.

Mahefkey, T., Yerkes, K. L., Donovan, B., and Ramalingam, M. L., 2004. "Thermal Management Challenges for Future Military Aircraft Power Systems," *Proceedings of SAE 2004 Power Systems Conference*, 2004-01-3204, Reno NV, November, pp. 309-317.

Mudawar, I., 2000. "Assessment of High-heat Flux Thermal Management Schemes," *Intersociety Conference on Thermal Phenomena*, Las Vegas, Nevada, 2000.

Mundo, C., Sommerfeld, M., and Tropea, C., 1995. "Droplet Wall Collisions: Experimental Studies of the Deformation and Breakup Process", *Int. J. Multiphase Flow*, Vol. 21, pp. 151-173.

Mundo, C., Sommerfeld, M., and Tropea, C., 1998. "On the Modeling of Liquid Sprays Impinging on Surfaces," *Atomization and Sprays*, Vol. 8, pp. 625-652.

Pasandideh-Fard, M., Qiao, Y.M., Chandra, S., and Mostaghimi, J., 1996. "Capillary Effects During Droplet Impact on Solid Surface", *Physics of Fluids*, Vol. 8, pp. 650-659.

Patankar, S. V., 1980. *Numerical Heat Transfer and Fluid Flow*, McGraw Hill, NY.

Pautsch, A. G., Shedd, T. A., Nellis, G. F., 2004. "Thickness Measurements of the Thin Film in Spray Evaporative Cooling," in the Proceedings of the 2004 Inter Society Conference on Thermal Phenomena. – ITHERM, IEEE, Piscataway, NJ, pp. 70-74.

Seyed-Yagoobi J. and Bryan, J. E., 1999. "Enhancement of Heat Transfer and Mass Transport in Single-Phase and Two-Phase Flows with Electrohydrodynamics," *Advances in Heat Transfer*, Vol. 33, pp. 95-186.

Snyder, T. J., Chung, J. N., and Schneider, J. B., 2001. "Dielectrophoresis with Application to Boiling Heat Transfer in Microgravity. II. Experimental Investigation," *Journal of Applied Physics*, Vol. 89, pp. 4084-4090.

Thoroddsen, S. T., 2002. "The Ejecta Sheet Generated by the Impact of a Drop," *Journal of Fluid Mechanics*, Vol. 451, pp. 373-381.

Tilton, D., 1989. "Spray Cooling," Ph. D. Dissertation, University of Kentucky, Lexington, KY.

Van doormaal, J. P., and Raithby., G. D., 1984. "Enhancements of the SIMPLE Method for Predicting Incompressible Fluid Flows." *Numerical Heat Transfer*, Vol. 7, pp. 147-163

White, F. M., 1991. *Viscous Fluid Flow*, McGraw-Hill, NY, 2<sup>nd</sup> Ed.

Yerkes, K. L., Michalak, T., Baysinger, K., Puterbaugh, R., Thomas, S. K., and McQuillen, J., 2005. "Variable-Gravity Effects on the Cooling Performance of a Single-Phase Partially-Confin ed Spray," Air Force Research Lab Report AFRL-PR-WP-TR-2005-2116.

Yerkes, K. L., Michalak, T., Baysinger, K., Puterbaugh, R., Thomas, S. K., and McQuillen, J., 2006. "Variable-Gravity Effects on a Single-Phase Partially-Confin ed Spray Cooling System," *ALAA Journal of Thermophysics and Heat Transfer*, Vol. 20, pp. 361-370.

Yoshida, K., Abe, Y., Oka, T., Mori, Y., and Nagashima, A., 2001. "Spray Cooling under Reduced Gravity Conditions," *Journal of Heat Transfer*, Vol. 123, pp. 309-318.